Characterization of structural properties of U and Pu in model systems by advanced synchrotron based X-ray spectroscopy

Zur Erlangung des akademischen Grades eines

DOKTORS DER NATURWISSENSCHAFTEN

(Dr. rer. nat.)

der KIT-Fakultät für Chemie und Biowissenschaften

des Karlsruher Instituts für Technologie (KIT)

genehmigte

Dissertation

von

Dipl. Chem. Ivan Pidchenko

aus

Ukraine, Simferopol

KIT-Dekan:	Prof. Dr. Willem Klopper
Referent:	Dr. Tonya Vitova (KIT Associated Fellow)
Korreferent:	Prof. Dr. Horst Geckeis
	Prof. Dr. Thorsten Schäfer

Tag der mündlichen Prüfung: 20.04.2016

This document is licensed under the Creative Commons Attribution – Share Alike 3.0 DE License
(CC BY-SA 3.0 DE): http://creativecommons.org/licenses/by-sa/3.0/de/

Erklärung

Hiermit versichere ich, dass ich die vorliegende Arbeit selbständig verfasst und keine anderen als die angegebenen Quellen und Hilfsmittel verwendet habe. Darüber hinaus versichere ich, dass alle Stellen der Arbeit, die wörtlich oder sinngemäß aus anderen Quellen übernommen wurden, als solche kenntlich gemacht sind und die elektronische Version der Arbeit mit der schriftlichen übereinstimmt und dass die Arbeit in gleicher oder ähnlicher Form noch keiner Prüfungsbehörde vorgelegt wurde. Die Satzung des Karlsruher Instituts für Technologie (KIT) zur Sicherung guter wissenschaftlicher Praxis wurde in der jeweils gültigen Fassung beachtet.

Datum, Ort Unterschrift

Acknowledgements

First, I would like to thank my scientific supervisors Prof. Dr. Horst Geckeis and Dr. Tonya Vitova for a very interesting subject of the Doctoral Project, exciting experiments and discussions during the whole time of the project.

I am grateful for the support of Dr. Jörg Rothe, who was the first to introduce me to a synchrotron facility and assisted, together with Dr. Kathy Dardenne, during the several beamtimes at the INE-Beamline, ANKA.

I am very thankful to Dr. David Fellhauer - “The Plutonium Master” and Dr. Dieter Schild - “The XPS Master” of INE for their great help and several measurements and preparations done for this work. These colleagues helped greatly with the several technical developments together with Elke Bohnert, Andreas Neumann, Valentin Traunfelder, Alexander Gensch, Radiation Protection Team as well as INE Workshop.

I express my gratitude to Dr. Kristina Kvashnina and Dr. Peter Glatzel (ESRF) for their assistance during several synchrotron experiments as well as Dr. André Rossberg and Dr. Cristoph Hennig for their interest and useful advices for some parts of a dissertation and to Dr. Bob Baker for his help in correcting this work.

I am thankful to my former scientific advisers Dr. Juhani Suksi, Prof. Dr. Jukka Lehto and Dr. Roman Bogdanov as well as my school chemistry teacher Dr. Valeriy Ustimenko, who first introduced me to the World of Chemistry.

Many thanks to my KIT friends for their support during a time of my PhD studies.

Finally, I am grateful to my mother Nadiia and my father Mikola for their infinite support for all my undertakings!

Abstract

This dissertation presents the investigations of different systems relevant for safety assessment studies of nuclear waste repositories using the X-ray based synchrotron techniques: *An* $L_3/M_{4,5}$ edge HR-XANES, L_3 edge EXAFS and 3*d*4*f* RIXS as well as other complementary techniques, including XPS, XRD and SEM/TEM.

In the first section, the U interaction with magnetite is investigated. In the first of the two investigated systems the U(VI) co-precipitated with magnetite nanoparticles with varying U concentrations, pH~8.0 and I[NaCl]=0.192 M is discussed. The U redox states and speciation after a short-term (10 days) up to long-term interaction time (373 days) were studied by U L_3/M_4 edges HR-XANES and EXAFS techniques. Samples kept under ambient conditions are also investigated. The U M_4 edge HR-XANES technique clearly detected three different redox states: U(IV), U(V) and U(VI) simultaneously present in the magnetite after 10 days and mainly a mixture of U(IV) and U(V) after 147 days interaction time. It is found that U(V) is stabilized in octahedral sites in the structure of magnetite at environmentally relevant concentration and was stable after 226 days exposure on air. In the second system the U(VI) redox behavior by interaction with magnetite nanoparticles in batch static conditions is investigated. A long-term batch sorption experiment (175 days) under nearly neutral pH conditions and I[NaCl]=0.01 M is performed. The effect of aqueous Fe(II) on the U redox states and the Fe speciation are studied. It is shown that the amount of U(V) stabilized on the surface of magnetite is 50% for 175 days aged samples. After addition of Fe(II) and two days contact time no U(IV) is formed, whereas the amount of U(V) has increased by 10%.

An interesting outcome of the studies is the apparent stabilization of U(V) in co-precipitation studies even under reducing conditions. Two species could be identified by EXAFS: incorporation in octahedral magnetite sites and as non-stoichiometric UO_{2+x}.

In the second section, the results from exploring structural investigations of three different U and Pu systems are presented. The very first study of U(VI) and U(V) carbonate complexes using *in-situ* spectroelectrochemical cell by U M_4 edge HR-XANES and 3*d*4*f* RIXS techniques coupled with *in-situ* UV-Vis spectroscopy is presented. One of the main tasks of this work includes the development, building and tests of the *in-situ* cell coupling spectroscopy with electrochemistry. Reference U M_4 edge HR-XANES spectra and 3*d*4*f* RIXS maps for U(VI) and U(V) carbonate complexes are measured for the first time. The spectra will be used for speciation analyses for identification of U(V)-*yl* species. Significant differences in the electronic structures of these complexes is found. A series of UO_3 polymorphs are investigated for the first time by the U M_4 edge HR-XANES technique. A fingerprint approach was proposed and applied to compare the level of covalency of the U-*yl* bonds within the UO_3 polymorphs. The order of the increase in covalency in the materials is found to be the same from the spectroscopy and the thermodynamic results based on free Gibbs energies of formations in series α-UO_3 < β-UO_3 < γ-UO_3 < $UO_3 \cdot 1\text{-}2H_2O$.

In the third part, Pu oxidation states, Pu(III), Pu(IV), Pu(V) and Pu(VI) in perchlorate solution and colloidal Pu(IV) prepared electrochemically are investigated for the first time by using Pu L_3/M_5 edges HR-XANES and 3*d*4*f* RIXS techniques. One of the key parts of this work is the development and testing of a set of cells for liquid, redox sensitive Pu samples, allowing the spectroscopic measurements. All measured HR-XANES spectra have significantly reduced spectral broadening resulting in better energy resolved features for all regions of the spectra. These spectra will be applied as references in future Pu speciation studies. It is demonstrated that the Pu M_5 edge HR-XANES technique detects 6% Pu(VI) present in a Pu(IV) sample.

Table of Contents

Abstract V

Table of Contents VII

1. Introduction and Motivation 1

2. X-Ray based Spectroscopy Techniques 6

2.1. X-ray absorption spectroscopy (XAS). Basic principles 6

2.2. High energy resolution X-ray absorption near edge structure (HR-XANES) and resonant inelastic X-ray scattering (RIXS) techniques. Basic principles 10

3. Experimental Techniques 16

3.1. X-ray absorption spectroscopy 16

3.2. High-energy resolution X-ray absorption near edge structure spectroscopy and resonant inelastic X-ray scattering 18

3.3. X-ray photoelectron spectroscopy 21

3.4. X-ray diffraction 23

3.5. Scanning and transmission electron microscopies 24

4. U Interaction with Magnetite 25

4.1. U(VI) co-precipitation with magnetite nanoparticles 26
4.1.1. Materials and Methods 27
4.1.1.1. Preparation of the samples 27
4.1.1.2. Speciation methods 28
4.1.1.3. EXAFS analysis 29
4.1.2. Results and Discussion 32
4.1.2.1. Characterization of magnetite nanoparticles 32
4.1.2.2. Redox state of Fe 34
4.1.2.3. Redox state of U 36
4.1.2.4. Analysis of non-stoichiometric UO_2 39
4.1.2.5. U(V) incorporated in Fe octahedral sites of magnetite 44
4.1.3. Conclusion 47

4.2. Influence of Fe(II) on the redox state of U sorbed on magnetite 48
4.2.1. Materials and Methods 49
4.2.1.1. Preparation and analyses of the magnetite nanoparticles 49
4.2.1.2. U(VI) batch sorption on magnetite/maghemite 50
4.2.1.3. Spectroscopic measurements 51
4.2.2. Results and Discussion 52
4.2.2.1. U 4*f* and Fe 2*p* XPS 54
4.2.2.2. U L_3 edge HR-XANES 56
4.2.2.3. U M_4 edge HR-XANES 57
4.2.3. Conclusion 59

5. HR-XANES and RIXS Investigations of U and Pu Systems 60

5.1. *In-situ* spectroscopy of the electrochemical reduction of U(VI) to U(V) in carbonate complexes 62

5.1.1. Introduction 62

5.1.2. Materials and Methods 64

5.1.2.1. Preparation of U stock solution 64

5.1.2.2. Electrochemical procedures 65

5.1.2.2.1. Cyclic voltammetry 65

5.1.2.2.2. Bulk electrolysis 66

5.1.2.3. *In-situ* UV-Vis spectroscopy 68

5.1.2.4. U M_4 edge HR-XANES/RIXS spectroscopy 69

5.1.2.5. Spectral area fitting 69

5.1.3. Results and Discussion 70

5.1.3.1. *In-situ* spectroelectrochemical cell 70

5.1.3.2. Cyclic voltammetry and chronoamperometry 73

5.1.3.3. *In-situ* UV-Vis spectroscopy 75

5.1.3.4. U M_4 edge HR-XANES/RIXS 77

5.1.4. Conclusion 81

5.2. Probing covalency in the UO_3 polymorphs by a fingerprint approach 82

5.2.1. Introduction 82

5.2.2. Materials and Methods 83

5.2.2.1. Sample preparations 83

5.2.2.2. Analysis methods 83

5.2.2.3. Quantum chemical calculations 84

5.2.3. Results and Discussions 85

5.2.3.1. U M_4 edge HR-XANES 86

5.2.3.2. Thermodynamic approach 89

5.2.4. Conclusion 90

5.3. Study of the Pu oxidation states in perchloric acid 91
5.3.1. Introduction 91
5.3.2. Material and Methods 92
5.3.2.1. Pu oxidation states preparation 92
5.3.2.2. Pu L_3 edge XAFS and L_3/M_5 edges HR-XANES/RIXS measurements 93
5.3.2.3. Quantum chemical calculations 94
5.3.3. Results and Discussion 95
5.3.3.1. Pu L_3 edge HR-XANES 96
5.3.3.2. Pu L_3 edge EXAFS 100
5.3.3.3. Pu M_5 edge HR-XANES 102
5.3.4. Conclusion 107

6. Summary and Outlook 108

List of References 111

Appendix 121

List of Tables and Figures 129

List of Symbols and Abbreviations 134

List of Publications and Contributions **136**

1. Introduction and Motivation

A fundamental understanding of the physical and chemical properties of the early actinide (*An*) elements (Ac-Am) and their interactions with the environment are obligatory for the long-term safety assessment of nuclear waste repositories (Figure 1.1). [1-3] Development of strategies for safe storage and disposal of radioactive wastes requires mechanistic understanding of the interaction of the waste products with the container materials in case of water accessing the waste. This necessitates speciation studies of radionuclides using advanced, sensitive techniques. [4-6]

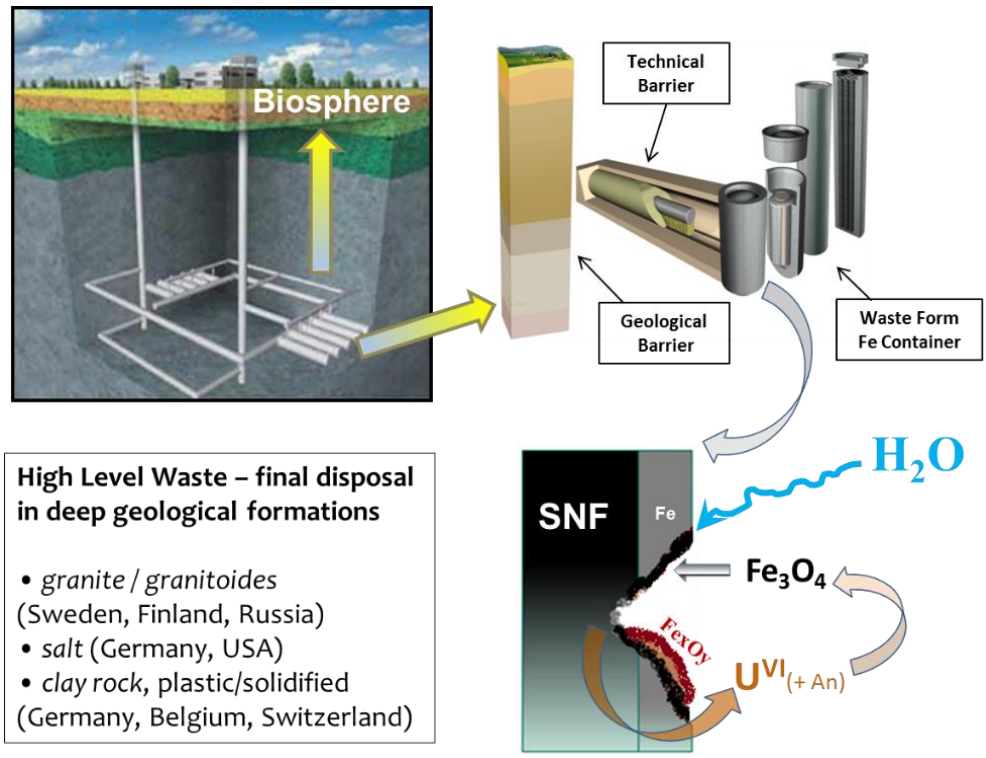

Figure 1.1. Schematic view of a potential nuclear waste repository including different barriers and an example of a corrosion process, which takes place by interaction of ground water with the storage container and the waste; a simplified list of final repositories in different type of geological formations considered by different countries is also included. (Source Nagra Info, 2010-2014)

For example, groundwater in a nuclear waste repository (NWR) and radiation induced redox processes can lead to oxidation of the inner iron (Fe) walls of the canisters resulting in formation of Fe oxides including, magnetite, maghemite and other Fe oxy(hydr)oxide phases. [7-9] It has been demonstrated that Fe containers can fail due to corrosion in abiotic conditions; these processes may potentially last thousands of years, depending on the disposal concept and the host rock considered, years resulting in Fe oxidation and destruction of the canister walls, followed by corrosion of the spent nuclear fuel (SNF). [10] In case of interaction with oxygenated water or due to radiolysis effects, the oxidation of the *An* to soluble and highly mobile redox states interacting with Fe corrosion products arising from continuous Fe dissolution and remineralization processes can lead to re-immobilization of such species.

Uranium is a main constituent of radioactive wastes (e.g. SNF) but it is also present in high quantities in contaminated sites after U ore reprocessing and technogenic accidents. Several redox active species control the U behaviour in the environment including redox active inorganic, i.e. iron, sulphur, nitrogen and dissolved oxygen [11, 12] as well as organic and biological species. [13-15] From those processes, significant interest lies in the investigation of the heterogeneous reduction of U(VI) by ferrous iron (Fe(II)). Such interactions are believed to be key processes influencing the mobilization/immobilization of U in the near and far field of the NWR. [16, 17] Uranium is often found as a mixture of its redox states in respective experiments. U has two environmentally relevant oxidation states, U(IV) and U(VI), and an intermediate U(V) with poorly understood chemical behaviour and interaction with the environment. U(V) is often not considered at all due to the lack of reliable detection methods. Recent works aimed to reconsider the significance of U(V) for U (geo)chemical systems. [16-18]

Besides U, one of the most challenging and important elements in SNF is plutonium (Pu). The long lifetime of the notably ^{239}Pu contribute significantly to the long-term radiotoxicity inventory of spent nuclear fuel (SNF). It has been shown that up to four Pu oxidation states may coexist under environmentally relevant conditions, each having different potential migration pathways in the environment. [3, 19] For reliable predictions of the mobility and the concentration of Pu under the geochemical conditions of nuclear waste repositories, a set of thermodynamic parameters and ion interaction coefficients are necessary. These parameters can be derived by combining dedicated wet chemistry (solubility and sorption) experiments with sensitive spectroscopic investigations. It is well known that Pu(IV) has a high tendency towards hydrolysis, polymerization and subsequent colloid formation under environmental conditions, depending on the aqueous solution redox potential. These colloids are believed to be in equilibrium with ionic solution species and in this case are part of the thermodynamic system of Pu aqueous chemistry. However, their formation is still not well understood and their role for Pu redox chemistry remains controversial. [20] The standard X-ray absorption spectroscopy (XAS) technique applied under *ex-situ* conditions cannot characterize the Pu polymers due to their heterogeneity and simultaneous presence of different species. Application of selective spectroscopic techniques would open up the possibility to gain deeper insight into the formation processes and stability of Pu species, which are highly relevant for the redox chemistry of Pu in aqueous solution at geochemically relevant concentrations. [5, 21, 22]

One widely used technique to determine *An* oxidation states is 4*f* X-ray photoelectron spectroscopy (XPS). [23, 24] The method provides mainly surface sensitive information about the *An* oxidation states by detecting variations in the binding energies of 4*f* electrons appearing as a chemical shift of peaks in spectra and by the observation of characteristic satellites. [25, 26] For example, the energy shifts between the U 4*f* peaks characteristic for U(VI), U(V) and U(IV) oxidation states usually amount to a few tens of eV and strongly overlapping.

As a result, it is often not possible to distinguish and unambiguously quantify the different U oxidation states. In a review of XPS studies related to U(IV), U(V) and U(V) compounds it has been shown that energy positions of U 4*f* peaks for some U(V) compounds can be similar with to those being characteristic for U(IV). [27] In case of mixtures of U oxidation states, the XPS analysis depends on the applied fitting procedure and can lead to ambiguous results. The analysis of U(V) is based on the evaluation of satellite peaks, which are only detectable with a sufficiently high signal to noise ratio for samples with high U content. Such samples are obviously not relevant for environmental studies. XPS also requires investigation of samples in ultra-high vacuum, which can potentially influence the chemical state of U and, that of the *An* in general.

The X-ray absorption spectroscopy (XAS) based methods, i.e. *An* L_3 X-ray absorption near edge structure (XANES) and extended X-ray absorption fine structure (EXAFS) have been intensively applied to investigate *An* oxidation states and their local coordination environments in environmentally relevant systems. [16, 28-34] The *An* L_3 edge XANES spectra are sensitive to the *An* oxidation states but the spectra are dominated by broad features due to large core-hole lifetime broadening effects. This prevents reliable characterization and quantification of the different *An* oxidation states in the same material. The high-energy resolution XANES (HR-XANES) technique at the U $M_{4,5}$ absorption edges was demonstrated to be very valuable for studies related to U oxidation state analysis in systems containing mixed oxidation states. [35] *An* $M_{4,5}$ edges HR-XANES has a great advantage over the conventional *An* L_3 edge XANES: reduced core-hole lifetime broadening for U $M_{4,5}$ and L_3 edges results in better resolved spectral features. [36] In turn, this allows for more precise oxidation state analysis. The method is also a direct probe for the *An* 5*f* valence states, which are of significant importance for the chemical bonding in *An* complexes. [35, 37] The *An* L_3 edge HR-XANES provides also additional information about the unoccupied 6*d* valence states of *An* compared to the conventional XANES method.

The main aims of this Doctoral Project are:

1) To unambiguously verify the U(V) species after interaction of U(VI) with magnetite nanoparticles under different reaction conditions using spectroscopic methods (Sections 4.1 and 4.2);
2) To design, build and apply the first compact *in-situ* electrochemical cell for reduction of U(VI) to U(V) by combining electrochemistry with UV-Vis and U $M_{4,5}$ edges HR-XANES/RIXS techniques (Section 5.1);
3) To design, build and apply a set of inert-gas liquid cells for *An* $M_{4,5}$ edge HR-XANES/RIXS studies of Pu(III)-Pu(VI) in perchloric acid solutions (Section 5.3);
4) To perform pioneering investigations of the unoccupied 5*f* and 6*d* valence states of U and Pu in three different reference systems and thereby fully demonstrate the characterization potential of the HR-XANES and RIXS techniques for electronic structure studies of *An* (Sections 5.1 and 5.3);
5) To generate U/Pu $M_{4,5}$ and L_3 edge HR-XANES reference spectra for speciation analysis of U and Pu in both laboratory and environmental systems (Sections 5.1, 5.2 and 5.3).

In each section the U M_4 and Pu M_5 edges HR-XANES and 3*d*4*f* RIXS results are complemented by one or several of the following complimentary characterization methods: XAFS, XPS, resonant inelastic X-ray scattering (RIXS), Transmission and secondary electron microscopies (TEM and SEM), X-ray diffraction (XRD) and ultraviolet-visible-near infrared (UV-Vis-NIR) technique. Quantum-chemical calculations with the FEFF code and resulsts from thermodynamic modelling have also been used to support some of the experimental results (Sections 5.2 and 5.3).

2. X-ray based spectroscopy techniques

2.1. X-ray absorption spectroscopy (XAS). Basic principles

XAS is a widely used technique for investigating the chemical speciation of *An*, i.e. oxidation states and local atomic structure in a variety of samples in environmentally relevant studies. [38] The advantage of this technique over for example, XRD, is that it can be used to study non-crystalline (amorphous and liquid) samples. In addition, it probes the local atomic environment of each absorbing atom, whereas XRD measures only ordered regions containing several unite cells. For environmentally relevant samples where the *An* concentrations are usually low, excluding U minerals and contaminated sites with high *An* contents, XAFS spectra are recorded in fluorescence and transmission modes. The absorption coefficient is measured as a function of the incident X-ray energy.

For fluorescence mode (Equation 1):

$$\mu(\mathrm{E}) \cdot d \in \frac{I_f}{I_0} \tag{1}$$

Where d is the thickness of the sample, I_0 – intensity of incident X-rays and I_f – intensity of fluorescence X-rays.

For transmission mode (Equation 2):

$$\mu(\mathrm{E}) \cdot d = \ln\left(\frac{I_0}{I_t}\right) \tag{2}$$

Where I_0 is the intensity incident photons and I_t - the intensity of transmitted photons.

The XAFS spectrum is divided into two parts. The first part beginnings from about -50 eV and ends at about +250 eV relative to the absorption edge and is called XANES. This region partially overlap with the EXAFS part of the spectrum. EXAFS typically starts after the most

intense absorption resonance (white line, WL) and continues to 1000 eV or more above the absorption edge. Figure 2.1.1 depicts the XAFS spectrum of uranium dioxide (UO_2).

The sharp rise in the absorption coefficient (absorption edge) occurs when the incident energy exceeds the binding energy of a core level electron, which is first excited to unoccupied bound states and when the energy is sufficiently high to the continuum states. The WL of the XANES is mainly used for determination of the redox state and to selectively probe the angular momentum projected unoccupied states of an atom as consequence of the dipole selection rule, i.e. electronic transitions are allowed only between energy states that differ in azimuthal quantum number (l) by ±1: $\Delta l = \pm 1$. This refers to $2p \rightarrow nd$ transitions for *An* $L_{2,3}$ edges. It also fingerprints to some extend the coordination geometry of the absorbing atom. EXAFS probes the local atomic environment of the absorbing atom. The EXAFS spectrum contains information on the types and number of atoms in coordination with the absorbing atoms, their interatomic distances and the degree of local structural disorder. [39, 40]

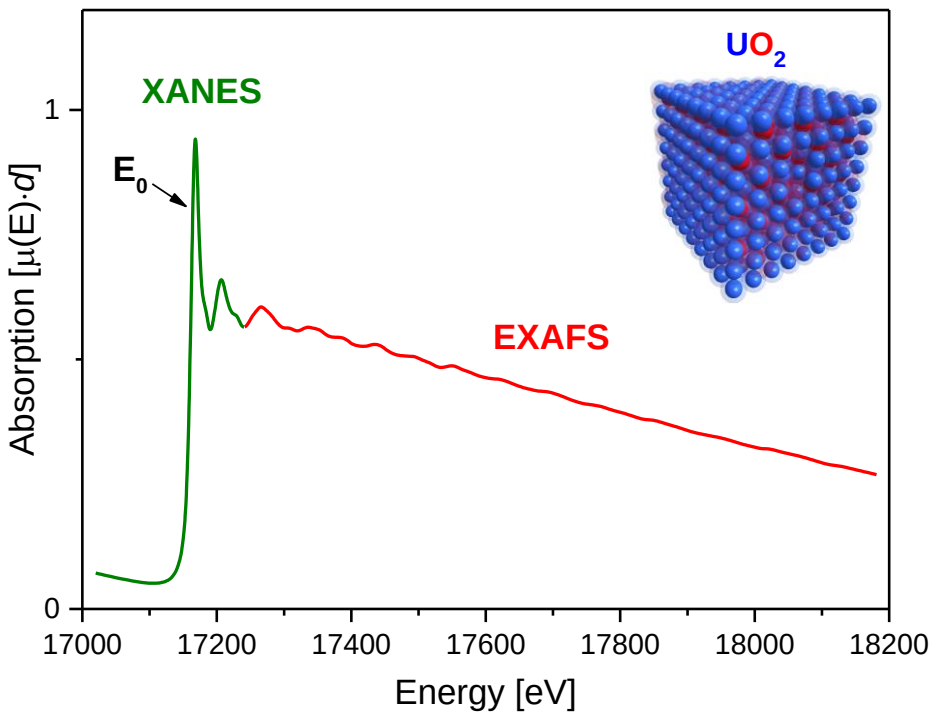

Figure 2.1.1. The XAFS spectrum of UO_2; the U absorption edge energy (E_0), the XANES and the EXAFS regions are marked.

To describe the EXAFS spectrum $\chi(k)$ the EXAFS equation is used, which can be represented as a sum of all scattering paths of the photoelectron in Equation 3. [41, 42]

$$\chi(k) = \sum_i \chi_i(k) \tag{3}$$

Where χ is a scattering path of the photoelectron. Each χ can be written as Equation 4:

$$\chi_i(k) = \sum_i \left(\frac{N_i S_0^{\,2}}{kR_i^{\,2}}\right) F_i(k) \sin[2kR_i + \varphi_i(k)] \cdot e^{-2\sigma_i^2 k^2} e^{-2R_i/\lambda(k)} \tag{4}$$

where R_i is described by Equation 5:

$$R_i = R_{0i} + \Delta R_i \tag{5}$$

and k is described by Equation 6:

$$k = \sqrt{2m_e\left(\frac{E - E_0 + \Delta E_0}{\hbar}\right)} \tag{6}$$

Here, the terms $F_i(k)$, $\varphi_i(k)$, and $\lambda(k)$ are the scattering amplitude of the photoelectron, the phase shift of the photoelectron, and the mean free path of the photoelectron. These parameters can be calculated by the *ab initio* quantum-chemical FEFF code based on the multiple-scattering theory. [40] R_i is the half path length of the photoelectron: the distance between the absorber and a coordinating atom for a single-scattering event. The value of R_{0i} is the half path length used in the theoretical calculation, and is modified by ΔR_i and shows a change in the interatomic distance relative to the initial path length R_i.

The variables described below can be determined by modelling the EXAFS spectrum. Equation 5 is used to express the excess kinetic energy of the photoelectron in wavenumbers (k) by using the mass of the electron m_e and the Plank's constant ($\hbar$). Here, ΔE_0 relates to a change in the photoelectron energy and it can be calculated by FEFF code. It is used to align the energy scale

of the theoretical spectrum to match the measured spectrum. It can be further simplified and represented as Equation 7:

$$k \approx 0.51\sqrt{E - E_0} \tag{7}$$

Here $E - E_0$ is in units of eV, and k is in units of Å^{-1}, where E is the incident energy of the photon and E_0 is electron binding energy of the emitted photoelectron. The EXAFS equation includes the following components: $N_i S_0^2$ changes the amplitude of the EXAFS signal and does not depend on k. The subscript i indicates that this value can be different for each path of the photoelectron. S_0^2 has a value between 0.7 and 1.0. [38]. $1/R_i$ is a contribution from a shell of atoms at a distance R_i which decreases with increasing distance from the absorber atom. $sin[2kR_i + \varphi_i(k)]$ considers the oscillations in the EXAFS signal with a phase represented by $2kR_i + \varphi_i(k)$. The path of the photoelectron is described by the distance which photoelectron travels to the neighbour atom (R_i) and then back ($2R_i$). In order to determine a phase shift it is multiplied by k. $\varphi_i(k)$ is a phase shift of the photoelectron caused by the interaction of the photoelectron with the nuclei of the absorber atom. Fourier transform (FT) of the *sine* function results in peaks at the interatomic distances between the absorber and coordinating atoms. In $e^{-2\sigma_i^2 k^2}$ part, the σ^2 is the mean-square displacement of the bond length between the absorber atom and the coordinating atoms in a shell. This term also includes contributions from thermal disorder and from structural heterogeneity. EXAFS measures the distribution of the distances between the absorber atom and each of the coordinating neighbour atoms within a shell in terms of a σ^2 value. $\lambda(k)$ is a mean free path of the photoelectron, which can be treated as the average distance that a photoelectron travels after its excitation. [38]

2.2. High-energy resolution X-ray absorption near edge structure (HR-XANES) and resonant inelastic X-ray scattering (RIXS) techniques. Basic principles

In this section, the HR-XANES technique is discussed. *An* L_3 edge conventional XANES spectroscopy has been commonly used for most environmentally relevant U studies. [29, 43-46]

In conventional fluorescence mode the *An* L_3 edge XANES spectrum is usually measured with a solid state detector (SSD) with detector's resolution exceeding 100 eV which is much higher than the energy width of a core-hole (< 10 eV). For example in the U L_3 edge XANES measurement the spectral energy resolution is limited by a large core-hole lifetime broadening of ~7.4 eV due to the short core-hole lifetime of the U $2p_{3/2}$ level. [36] The resolution is additionally influenced by instrumental broadening originating from the beamline optical components. Thus the total energy resolution of the XANES spectrum is described as a combination of the core-hole width and the instrumental effects, which are described mathematically as Lorentzian and Gaussian type broadenings, respectively. [47] The spectral broadening can be significantly reduced by applying high-energy resolution multi analyzer crystal (MAC)-Spectrometer. The central component of the MAC-Spectrometer used in this doctoral project is a spherically bent free of defects usually Si/Ge crystal with specific orientation that diffracts the characteristic fluorescence emitted from the sample and focuses it onto a SSD. In such experimental setup, the analyser crystal is positioned in a one-to-one focusing Rowland geometry with a SSD and a sample. [48, 49] In order to increase the solid angle of collection the MAC-Spectrometer contains five analyser crystals. This setup is adopted from original design realized for the Beamline ID26, ESRF.

The advantage of this experiment is that the width of the spectrum is no longer limited by the $2p_{3/2}$ core-hole lifetime but by the sharper $3d_{5/2}$ width in the final state. [50-52]

The technique of reducing the core-hole lifetime broadening obtained in the XANES spectra by using MAC-Spectrometer was first shown by Hämäläinen *et al*. on lanthanide systems. [53] The technique has been named as partial fluorescence yield XANES (PFY-XANES), high-energy resolution fluorescence detected XANES (HERFD-XANES or HR-XANES in the text). [51, 52, 54, 55] The spectral broadening achieved for the U L_3 edge HR-XANES spectrum becomes lower than the width of the $2p_{3/2}$ core-hole and has been estimated as ~4.5 eV. It can be further reduced by recording HR-XANES spectra using other emission lines, i.e. $L_{\beta 5}$ ($5d_{3/2} \rightarrow 2p_{3/2}$) with spectral broadening estimated as ~1 eV. This resolution is sufficient to resolve separate peaks resulting from a crystal field splitting of the U 6*d* states in UO_2. [50, 56] *An* L_3 edge XANES probes unoccupied *An* 6*d* states and is sensitive to its octahedron coordination and to crystal field splitting effects, however the most interesting properties of U and the other *An* originate from the participation of the 5*f* valence states in the chemical bonding. These are located closest to nuclei and do not overlap much with the 6*d*, 7*s* and 7*p* orbitals (Figure 2.2.1).

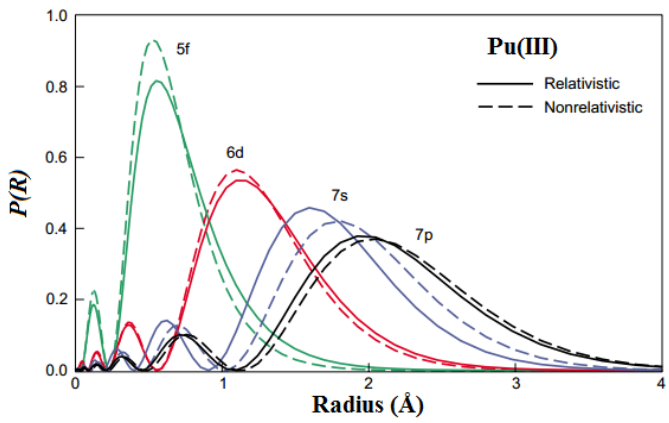

Figure 2.2.1. Radial extent of Pu 5*f* valence electrons. The radial probability *P(R)* of finding electron at a distance *R* from nucleus is shown for the valence 5*f*, 6*d*, 7*s* and 7*p* orbitals for Pu(III). The solid lines show the probabilities after the inclusion of relativistic effects. (Used from Los Alamos Science Journal, 2000, by D. Clark)

The 5*f* unoccupied states can be directly probed by measuring U XANES spectra at the $M_{4,5}$ edges using the M_β ($4f_{5/2} \rightarrow 3d_{3/2}$) ($M_4$ edge) or M_α ($4f_{7/2} \rightarrow 3d_{5/2}$) ($M_5$ edge) emission lines. U M_4 edge has an advantage over the M_5 edge due to ~200 eV higher energy facilitating less losses of X-ray signal and slightly better energy resolution of the

MAC- Spectrometer for the M_β emission line. [56]

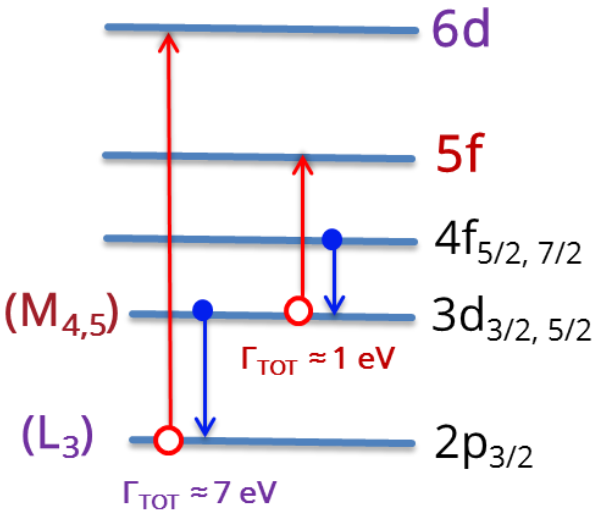

Figure 2.2.2. Schematic electron excitations and emission transitions for *An* L_3 and $M_{4,5}$ edges.

In this case the width of the spectral features is no longer limited by the $3d_{3/2}$ core-hole lifetime, but by the sharper $4f_{5/2}$ lifetime broadening of ~0.37 eV. [57] The examples of U L_3 and M_4 edges conventional and HR-XANES spectra for U(VI) uranyl type compounds are shown in Figures 2.2.3 a, b. The spectral peaks are more intense and are better resolved for both edges with a remarkable difference for the U M_4 edge for which two additional higher energy separate peaks are clearly resolved.

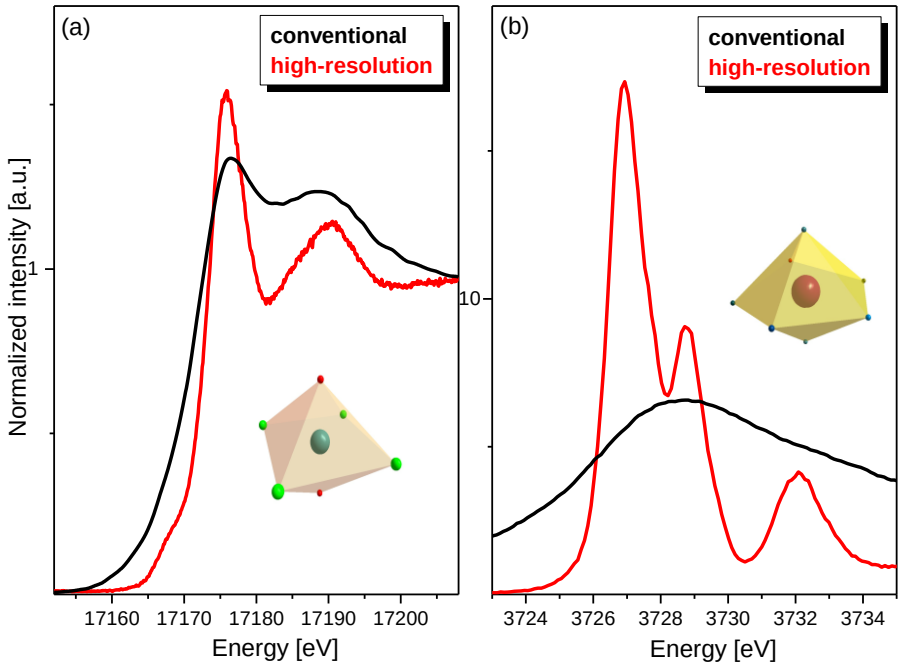

Figure 2.2.3. U L_3 (a) and M_4 (b) edges conventional and HR-XANES spectra of $Cs_2(UO_2)Cl_4$ and $UO_3 \cdot 1\text{-}2H_2O$ (meta-schoepite), respectively.

An example of a resonant inelastic X-ray scattering (3*d*4*f* RIXS) contour map of U(VI) is depicted in Figure 2.2.4. This 3*d*4*f* RIXS map comprises the U_β emission of U measured as a function of the excitation energy across the U M_4 absorption edge. The HR-XANES spectrum corresponds to the cut parallel to the excitation energy performed at the maximum of the normal emission line. The normal emission is recorded for excitation energies well above the absorption edge when the photoelectron is excited to the continuum, i.e. the atom is ionized.

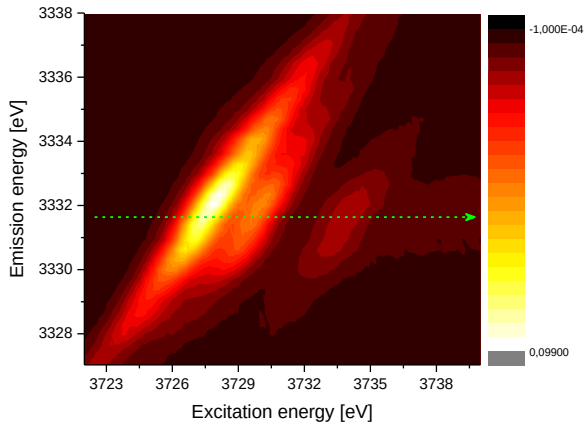

Figure 2.2.4. U 3*d*4*f* RIXS map of U(VI) in 1 M $HClO_4$ aqueous solution.

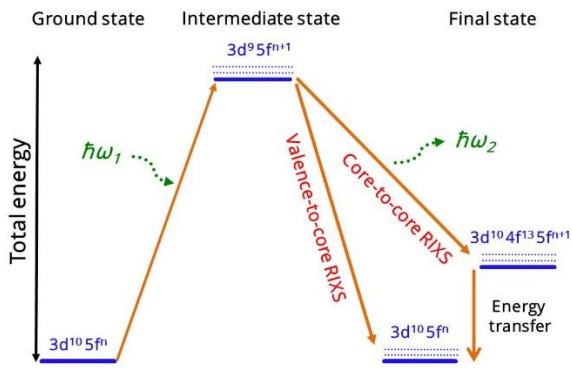

Figure 2.2.5. Schematic representation of RIXS processes for *An*.

RIXS is a process where electron is first excited from the ground state ($3d^{10}5f^{n}$ for U) to unoccupied bound states ($3d^{9}5f^{n-1}$, intermediate state) followed by relaxation processes with emission of characteristic X-rays after the core-hole is filled with an electron from higher energy states ($3d^{10}5f^{n}$, final state). [35, 50, 58, 59] Figure 2.2.5 represents a scheme for two RIXS processes for the *An* $M_{4,5}$ edge. In this work, the core-to-core RIXS (3*d*4*f* RIXS) technique is used. For this RIXS process, the 3*d* core-hole is filled from another core like state 4*f*. The overall spectral broadening is dominated by the core-hole lifetime broadening, which has contributions from the intermediate and final states and can be estimated by the approach shown by de Groot *et al*. [47]

The experimental spectrum also includes instrumental broadening effects with two main contributors: beamline (energy resolution of the DCM, size of the beam on the sample etc.) and spectrometer (quality and bending radius of the analyzer crystals, Bragg angle etc.).

The total experimental energy bandwidth is estimated as 0.7 eV for the ID26 Beamline [35]; the value is ~0.5 eV higher, 1.2 eV, for both U (M_4 edge, 3728 eV) and Pu (M_5 edge, 3775 eV) at the INE-Beamline mainly due to a bigger spot size of the incident beam. These values are determined by measuring the full width at half maximum (FWHM) of the elastic peak.

All relevant *An* L_3 and $M_{4,5}$ edges (Pa-Cm) are accessible over the $L_{\alpha 1}$, M_α and M_β emission lines with the available at the INE-Beamline (5 Si(111), 5 Ge(111), 5 Si(220)) analyzer crystals (Figure 2.2.6).

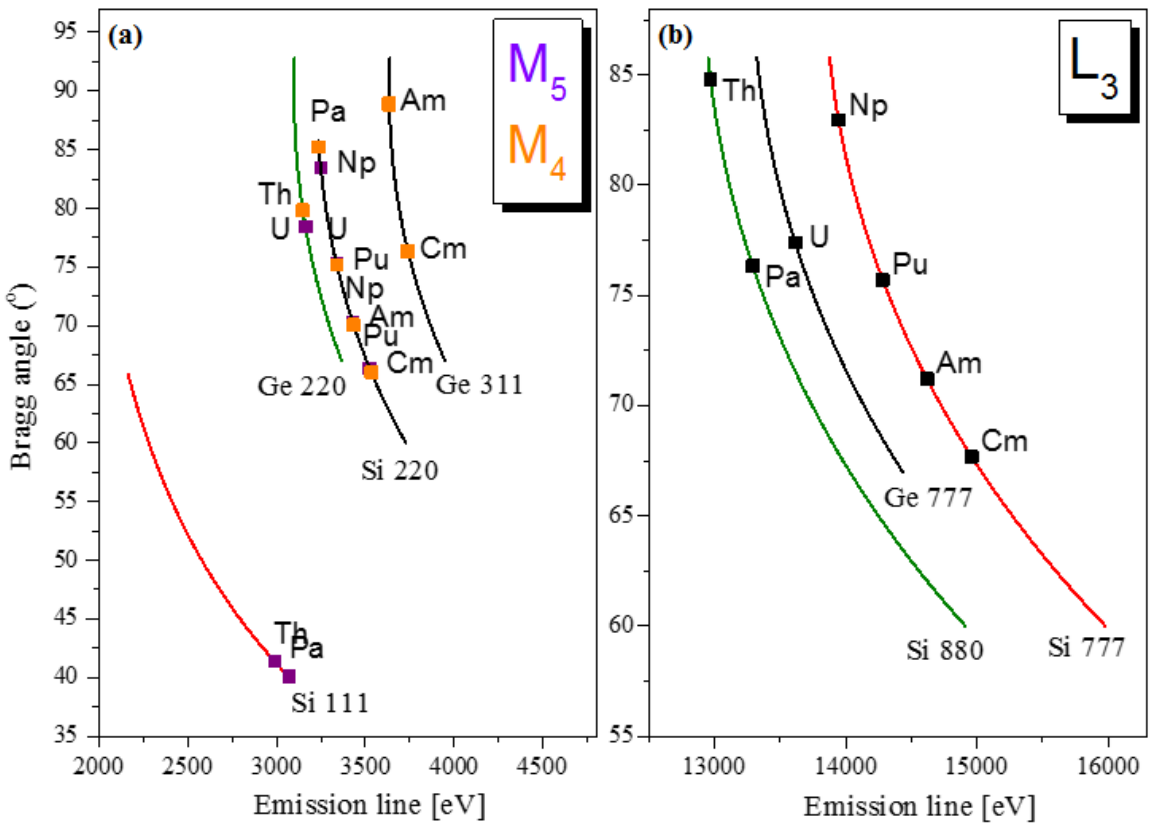

Figure 2.2.6. Emission energies and the corresponding analyzer crystals and Bragg angles for *An* M_β/M_α (a) and *An* $L_{\alpha 1}$ (b) emission lines for *An* Z=90-96.

The measured absorption edges of U and Pu, emission lines, the used analyser crystals and corresponding Bragg angles are listed in Table 2.2.1.

Table 2.2.1. Emission energies, analyzer crystals and corresponding Bragg angles used in the U and Pu L_3 as well as U and Pu $M_{4,5}$ edges HR-XANES measurements.

Absorption edge, [eV]/ emission line, [eV]	Electronic transition	Analyser crystals	Bragg angle, θ°
U L_3 (17168) / $L_{\alpha 1}$ (13618)	$3d_{5/2} \rightarrow 2p_{3/2}$	Ge(777)	77.39
Pu L_3 (18057) /$L_{\alpha 1}$ (14282)	$3d_{5/2} \rightarrow 2p_{3/2}$	Si(777)	75.70
U M_4 (3726) / M_β (3337)	$4f_{5/2} \rightarrow 3d_{3/2}$	Si(220)	75.18
Pu M_5 (3775) / M_α (3351),	$4f_{7/2} \rightarrow 3d_{5/2}$	Si(220)	75.22

3. Experimental techniques

3.1. X-ray absorption spectroscopy

The XAS experiments were performed at the INE-Beamline for *An* research (ANKA synchrotron radiation facility, Karlsruhe). [54] The layout of the INE-Beamline is shown in Figure 3.1.1.

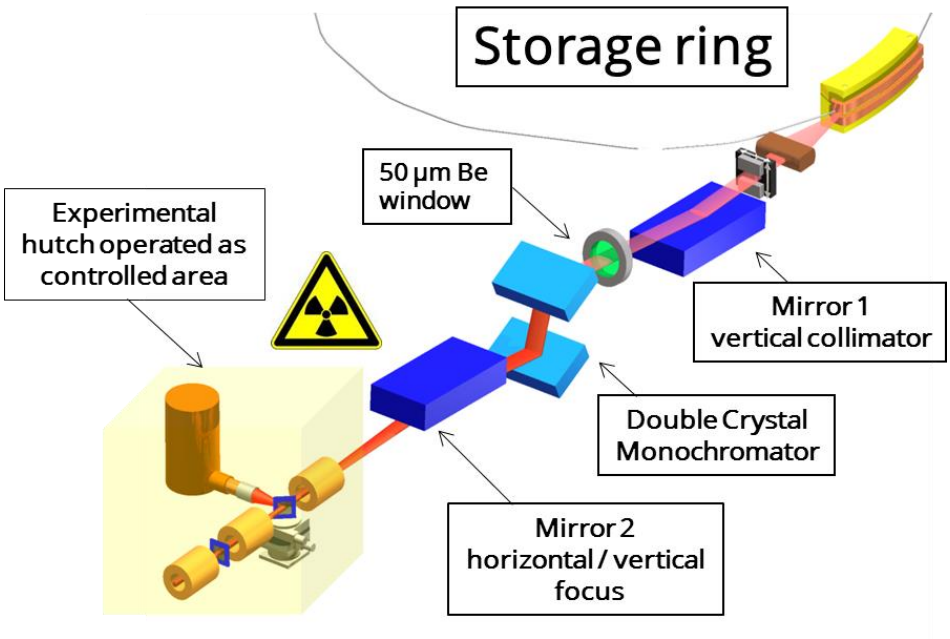

Figure 3.1.1. 3*D* graphical layout of the INE-Beamline. Source [54]

A double crystal monochromator (DCM) equipped with two Ge(422) crystals was used for the energy monochromatization. The U and Pu L_3 edge XAFS spectra were recorded in fluorescence detection mode by registering the U $L_{\alpha 1}$ (13618 eV) and the Pu $L_{\alpha 1}$ (14282 eV) fluorescence lines, respectively, as a function of the incident photon energy by means of a five-element high purity Ge solid state detector (Canberra) (U: Section 4.1; Pu: Section 5.2).

Y (K edge = 17038 eV) and Zr (K edge = 17998 eV) foils were simultaneously measured with the U and Pu samples in transmission mode, respectively; these foils were also used for energy calibration of the DCM.

The samples in form of suspensions (U: Section 4.1) or aqueous solutions (Pu: Section 5.3) were placed into 300 µl vials and positioned into the inert gas cell. Ar gas was flushed continuously during the experiment. From three to six scans were usually collected at room temperature and averaged for each sample. The averaged XAFS scans were normalized by subtraction of a linear background function from the featureless pre-edge region and normalization of the edge jump to unity. The EXAFS spectra were extracted and analyzed with the ATHENA and ARTEMIS programs, respectively, included in the IFEFFIT package. [60] The single scattering paths used in the modelling procedure were generated with the FEFF9.5 code. [61, 62] More details on the preparation of the samples and the analyses of the spectra are given in Sections 4.1 and 5.3 for U and Pu, respectively.

3.2. High-energy resolution X-ray absorption near edge structure spectroscopy and resonant inelastic X-ray scattering

The HR-XANES experiments were performed at the INE-Beamline (ANKA) for U (Sections 4.1, 5.1 and 5.2) and Pu (Section 5.3) [54] and at the Beamline ID26 (ESRF) for U (Sections 4.1 and 4.2). [48] The U and Pu 3*d*4*f* RIXS experiments were carried out at the INE-Beamline. Two Si(111) and Ge(422) crystals were set in the DCM and used for the U/Pu $M_{4,5}$ and Pu L_3 edge experiments at the INE-Beamline, respectively. The beam was focused to ~0.500 mm vertically and ~0.500 mm horizontally at the position of the sample, XANES spectra were measured in high-resolution mode using the MAC-Spectrometer depicted in Figure 3.2.1. (Pruessmann, PhD Thesis, 2016) The sample, five analyzer crystals and a single diode silicon drift detector (SDD Vortex) were arranged in a vertical Rowland geometry (Figure 3.2.1 top left). The Si(220) (edges, emission lines)/Ge(777) (edge emission line) five spherically bent crystal analyzers with 1 m bending radius were applied. A glovebox equipped with a chamber for transfer of samples was built around the MAC-Spectrometer to minimize losses of X-ray intensity for the U/Pu $M_{4,5}$ edge experiments. Constant He flow was maintained. The O_2 level was monitored and kept constant (~0.1%) inside the He box. The experimental energy resolution measured for the U/Pu $M_{4,5}$ edge HR-XANES experiments was ~1.2 eV; it was determined by measuring the FWHM of the elastic peak. The experimental energy resolution was not measured for the Pu L_3 edge experiments due to the low intensity of the elastically scattered X-rays. U/Pu $M_{4,5}$ edge HR-XANES and normal emission spectra of a uranyl peroxide mineral ($UO_4 \cdot 2H_2O$)/UO_2 and PuO_2 for U and Pu, respectively, were measured after each sample to verify the energy calibration of the DCM and the alignment of the MAC-Spectrometer. Zr foils was measured in transmission mode simultaneously with the samples for the Pu L_3 edge HR-XANES experiments. Resonant inelastic X-ray scattering (3*d*4*f* RIXS) maps

for U/Pu compounds were measured by recording HR-XANES across the normal M_β/M_α emission line.

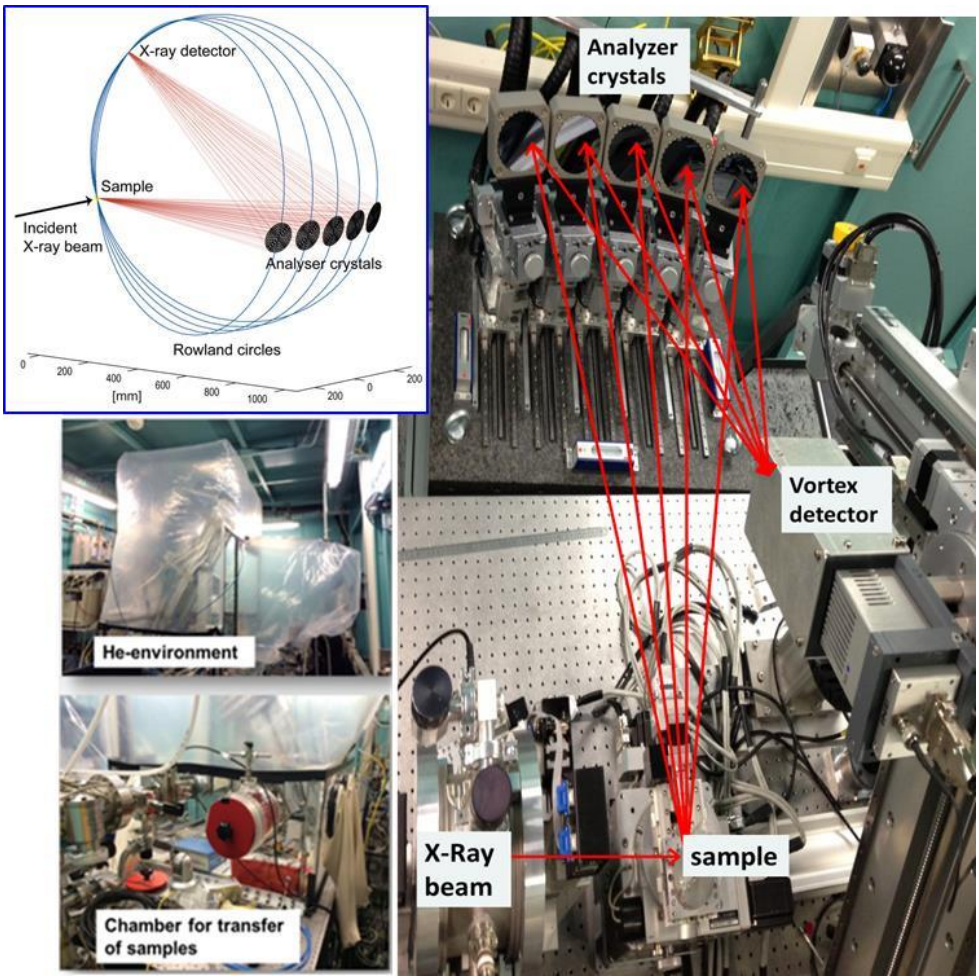

Figure 3.2.1. A photograph of the MAC-Spectrometer installed at the INE-Beamline (right). A scheme of the Rowland circle geometry (top left). The He glovebox and the transfer chamber for the samples (left bottom).

For the measurements of the U L_3 and M_4 edges HR-XANES spectra at the ID26 beamline, ESRF. The incident energy was monochromatized by a Si(111) DCM. Rejection of higher harmonics was achieved by three Si mirrors at an angle of 3.5 mrad (for the U M_4 edge experiment) and three Pd mirrors at an angle of 2.5 mrad (for the U L_3 edge experiment) relative to the incident beam.

The beam size was focused to ~0.150 mm vertically and ~0.450 mm horizontally for the measurements at both absorption edges. XANES spectra were measured in high-resolution mode using a MAC-Spectrometer. The sample, analyzer crystal and silicon drift diode (SDD) were arranged in a vertical Rowland geometry. The U HR-XANES spectra at the L_3/M_4 edges were obtained by recording the maximum intensity of the U L_α/M_β emission lines. Ge(777) (emission line) or the Si(220) (emission line) diffraction order of five spherically bent Ge/Si crystal analyzers with 1 m bending radius were used. The experimental energy resolution was ~2.6 eV for the U L_3 and ~0.7 eV for the U M_4 edge and was determined by measuring the FWHM of the elastic peak. The paths of the incident and emitted X-rays through air were minimized in order to avoid losses in intensity due to absorption. Depending on the edge, from ten to forty-four scans were measured for each sample. Samples were checked for the radiation damage by measuring very fast scans (12 sec/spectrum) with and without 200 µm Al foil attenuating the beam intensity. For the U M_4 edge changes in the spectral shape were detected after 60 seconds of measuring time, therefore each XANES spectrum has been collected at a fresh sample spot and measured for 12 s/spectrum; all spectra were normalized to the maximum absorption intensity.

3.3. X-ray photoelectron spectroscopy

The U containing magnetite samples were prepared for X-ray photoelectron spectroscopy (XPS) measurements in the glove box under Ar atmosphere. The dried solid samples were pressed on indium foil and mounted on the gas tight sample holder. Transfer of the samples under Ar atmosphere into the XP spectrometer was achieved by means of an O-ring sealed vacuum transfer vessel.

XPS measurements were carried out by using a ULVAC-PHI VersaProbe II instrument equipped with a monochromatized Al K_α X-ray source (1486.6 eV) operated at 33 W source power. The spectrometer has a hemispherical capacitor analyzer and a detector consisting of a micro channel plate with 16 anodes. Calibration of the binding energy scale of the spectrometer was performed using well-established binding energies of elemental lines of pure metals (surface cleaned by Ar ion beam sputtering, monochromatic Al K_α: Cu $2p_{3/2}$ at 932.62 eV, Au $4f_{7/2}$ at 83.96 eV. [63] The difference of binding energies between both lines is adjusted by the electronics to coincide with the reference value of 848.66 eV within ± 0.1 eV. Standard deviation of binding energies is within ± 0.1 eV for conductors and within ± 0.2 eV for non-conducting samples. Spectra were collected at a take-off angle of 45° (angle between sample surface and analyzer). During analysis, the pressure inside the spectrometer was about 2×10^{-7} P_a. Elemental composition of the sample surface was analyzed by survey spectra recorded with pass energy of 187.85 eV at the hemispherical capacitor analyzer. The areas of elemental lines (after Shirley background subtraction), sensitivity factors, asymmetry parameters, and transmission function of the analyzer were used to calculate the atomic concentrations. To retrieve information about the chemical state of the elements, narrow scan spectra of elemental lines were recorded with pass energy of 46.5 eV allowing the acquisition of high-resolution spectra. The XP spectrometer results a FWHM of 0.7 eV for the Ag $3d_{5/2}$ line at this pass energy.

The magnetite powder samples were almost conductive, thus only a small shift for charge referencing (< 0.3 eV) to the O 1*s* elemental line of magnetite at 530.2 eV was applied. [64] Charge referencing to the C 1*s* elemental line of adventitious hydrocarbon commonly used was not practical since the C 1*s* spectra exhibited noisy spectra at low intensity. Curve fitting of the narrow scans of elemental lines was performed by the program PHI MultiPak, version 9.6.0 (data analysis program) using a nonlinear least-squares optimization procedure with Gaussian-Lorentzian sum functions after subtraction of an iterated Shirley background.

3.4. X-ray diffraction

X-ray diffraction (XRD) experiments were performed using a X-ray tube and a synchrotron as sources of X-ray radiation. Bruker AXS D8 laboratory powder diffractometer equipped with a BSI (Baltic Scientific Instrument) Si(Li) solid detector and a Cu K_α X-ray source was applied. Synchrotron based XRD experiments were performed at the SUL-X-Beamline at ANKA (KIT, Karlsruhe). [65] A Si(111) crystal pair with a fixed beam exit was used as a monochromator. The X-ray beam was aligned to an intermediate focus, and then collimated by slits located at a distance of the intermediate focus to 500 μm × 500 μm and subsequently focused with a Kirkpatrick-Baez mirror pair to about 250 μm (hor.) × 150 μm (vert.) size at the sample position. XRD patterns were measured in transmission mode with a CCD detector using 2×2 binning during 90 seconds of exposure time. The beamline was operated at energy of 17000 eV (λ=0.731708 Å). All measurements have been performed under air and room temperature. Data analysis was performed using FIT2D program [66] for radial integration of the Debye rings and DIFFRAC.EVA V3.1 program for background subtraction and diffraction peaks evaluation. Measured spectra were compared with reference XRD patterns from the American Mineralogist Crystal Structure (AMCSD) and the Inorganic Crystal Structure (ICSD) databases.

3.5. Scanning and transmission electron microscopies

For imaging purposes two different devices have been used, the scanning and transmission electron microscopies (SEM and TEM).

For SEM a commercial CamScan CS44FE Field Emission SEM (Cambridge, UK) has been used. For TEM imaging FEI Tecnai G2 F20 X-TWIN machine has been used operated at 200 kV in high-resolution transmission electron microscopy (HR-TEM) mode. A sample preparation procedure was as following: the U containing magnetite suspension was rinsed by MilliQ water and a TEM specimen was prepared by dispersing the rinsed solution on a carbon thin film on a Cu grid followed by that the solution was dried up at room temperature with an Ar atmosphere.

4. U interaction with magnetite

A number of laboratory studies have been performed to clarify the fate of U(VI) by interaction with magnetite. [28, 29, 45, 46] Due to kinetic effects during interaction with Fe(II)/Fe(III) species, U is often found as a mixture of its redox states. U has two environmentally relevant redox states, U(IV) and U(VI), and an intermediate as well U(V) with poorly understood chemical behavior and interaction with the environment. U(V) is often not considered due to the lack of reliable detection methods. Recent works aimed to reconsider the significance of U(V) for U containing (geo)chemical systems. [16-18]

Two different U-Fe systems are investigated in the present Section:

The first part is dedicated to co-precipitation of U(VI) at varying concentrations with magnetite nanoparticles. The U redox states and U speciation after a short (10 days) and a long-term interaction period (ca. 373 days) are studied. Investigations related to U(VI) removal by magnetite nanoparticles in batch static and dynamic systems are also performed. The long-term batch sorption study takes place for 175 days is under nearly neutral pH conditions.

4.1. U(VI) co-precipitation with magnetite nanoparticles

There are several studies investigating the potential investigations of uranium into the iron oxy-(hydr)oxides: ferrihydrite, goethite and hematite partly in presence of Fe(II). [17, 67] No studies were specifically dedicated to the co-precipitation of uranium for environmentally relevant concentration with one of the most relevant iron oxide phases under reducing condition namely, magnetite. The investigations presented here are concentrated on the redox and speciation characterization of uranium in the final product formed by co-precipitation of U with magnetite. Specifically the U redox states and speciation in magnetite nanoparticles with varying (1000-10000 ppm) U loadings were investigated by U M_4/L_3 edges HR-XANES and U L_3 edge XAFS as well as TEM. SEM, XRD, XPS and thermodynamic modeling were additionally used to characterize the magnetite nanoparticles. The main aim is to verify the presence of U(V) in this system and to describe its local coordination environment. A long-term study (373 days) was performed to elucidate the stability of U(V) incorporated in the structure of magnetite. It is demonstrated that the applied U M_4 edge HR-XANES method is capable of detection of U(IV), U(V) and U(VI) simultaneously present in the same sample at environmentally relevant concentrations.

4.1.1. Materials and Methods

4.1.1.1. Preparation of the samples

To a 50 mL Teflon container inside an argon (Ar) glovebox equipped with pH, E_h electrodes (Metrohm) and a dropping funnel, the calculated amounts of aqueous $FeCl_3$, $FeCl_2$ (starting pH=2.3) and an aliquot of U(VI) (UO_2Cl_2, pH=2.5) were added followed by dropwise addition of 0.5 M NaOH. The pH of the resulting suspension was adjusted within a range 7.5-8.0. The suspension was stirred overnight, pH and E_h values were recorded and pH was adjusted if necessary by adding 0.1 M NaOH. After complete precipitation the aliquot of supernatant was filtered with a 0.22 µm Millipore filter and investigated by ICP-MS to determine the U and Fe concentrations. The U and Fe concentrations were found below the respective detection limit (< 0.1 ppb for U) and (< 300 ppb for Fe). Experimental details for U, Fe and salt concentrations as well as pH, E_h measurements are given in Table 4.1.1.

Table 4.1.1. U and Fe concentrations, pH, E_h and Ionic strength (I[NaCl]). Detailed information is given in Table 4.1.2.

Sample	[U], $\cdot 10^{-5}$ M	[Fe], M	I[NaCl], M	pH initial	E_h initial, mV	pH final	E_h final, mV
Um10	20	0.062	0.192	2.2	740	8.0	-330
Um6	12	0.062	0.192	2.3	750	7.5	-310
Um3	6	0.062	0.192	2.4	740	7.7	-210
Um1	2	0.062	0.192	2.3	760	7.7	-370
Um1a	2	0.062	0.192	-	-	-	-
Umh	6	0.062	0.020	7.1	110	7.7	160

4.1.1.2. Speciation methods

Several spectroscopic and microscopic techniques have been used for sample characterization. The U M_4/L_3 edges HR-XANES, U L_3 edge XAFS, U 4*f* and Fe 2*p* XPS, SEM and TEM as well as powder XRD are described in Section 3. The U M_4/L_3 edges HR-XANES spectra were measured in the energy range of 3723 eV to 3735 eV for M_4 edge and from 17142 eV to 17242 eV for L_3 edge with step sizes of 0.1 eV for both edges for Sections 4.1 and 4.2.

Ten days after preparation of the Um1 Um3, Um6 and Um10 samples U M_4/L_3 edges HR-XANES spectra were measured at the ID26 Beamline, ESRF, Grenoble. An inert gas (Ar) sample holder comprising a double compartment has been designed and used for the experiments (Figure 4.1.1). To avoid contact of the samples with air they were transported in a gas tight aluminum cylinder filled with Ar and opened very shortly prior to the measurements. All samples were prepared in an Ar glove box with O_2 level < 1 ppm. After the U M_4 edge HR-XANES measurements the samples were disposed of. Samples aged for 147 days sampled from the same synthesis batch (Um1, Um3, Um6 and Um10) were studied with U L_3 edge XAFS at the INE-Beamline, ANKA, Karlsruhe, using an inert gas cell. [54] The Um1 sample has been kept outside of the Ar glovebox in non-hermetically sealed plastic vials for 142 days (Um1a) prior to the U M_4 edge HR-XANES measurements at the INE-Beamline using a X-ray emission spectrometer. [68] In order to minimize the absorption of the low energy photons by the salts formed at the surface of the Um1a sample, the magnetite suspension has been very quickly washed with MQ-H_2O prior to the U M_4 edge HR-XANES measurements. The same Um1a sample has been kept in the sample holder at ambient conditions for 84 days and was studied again with U L_3 edge XAFS at the INE-Beamline.

All XPS and XRD measurements were done for samples sampled from the same batch 310 and 480 days after their preparation, respectively. Table 4.1.2 summarizes the descriptions of the samples and the applied characterization methods.

4.1.1.3. EXAFS analysis

Three U-O, two U-Fe and one U-U single scattering paths (total six) were used to fit the EXAFS spectra of the Um10, Um6 and Um3 samples. No U-Fe2 and U-U1 were resolved in the EXAFS spectrum of the Um1a sample. A shell-by-shell modeling approach was followed in the EXAFS analyses. The shells were modeled using structural parameters from the following databases: U-O1, 2.37 Å and U-U, 3.87 Å: UO_2 ICSD 168164; U-O2, 2.65 Å: UO_2, ICSD 82477; U-O3, 1.77 Å: $UO_3 \cdot 1\text{-}2H_2O$; ICSD 82477; U-Fe1, 2.97 Å and U-Fe2, 3.48 Å; Fe_3O_4, AMCSD 0002400. The amplitude reduction factor (S_0^2) was set to 0.77 as determined from EXAFS analyses of a bulk UO_2 reference sample measured at the same experimental conditions. The shells were fitted in the following order: U-O1, U-U, U-Fe1, U-O3, U-O1, U-Fe2. For each shell, initially R values were allowed to vary, while N values were fixed; N and R were consecutively varied until the best fit was obtained; this procedure was repeated for each shell. The Debye-Waller factors (DW) and the energy shifts of the ionization potential (ΔE_0) were always varied. The amount of variables were kept approximately half or less the number of independent data points during the fitting. No U-U1 and U-Fe1 shells were used to model the EXAFS spectrum of the Um1a sample. For all EXAFS fits, the general requirement was to obtain a goodness of fit parameter (r) of about 0.01, i.e. 1% difference between data and model (Table 4.1.3). The ΔE_0 parameters found for all spectra were between 5.0 and 7.3 and correspond to the values found for similar studies. [29, 30, 67] The DW for U-Fe1 are 2-4 times higher than those obtained for U-O and U-U shells, due to the structural interference introduced by widely varying U-Fe distances. [17, 32, 69]

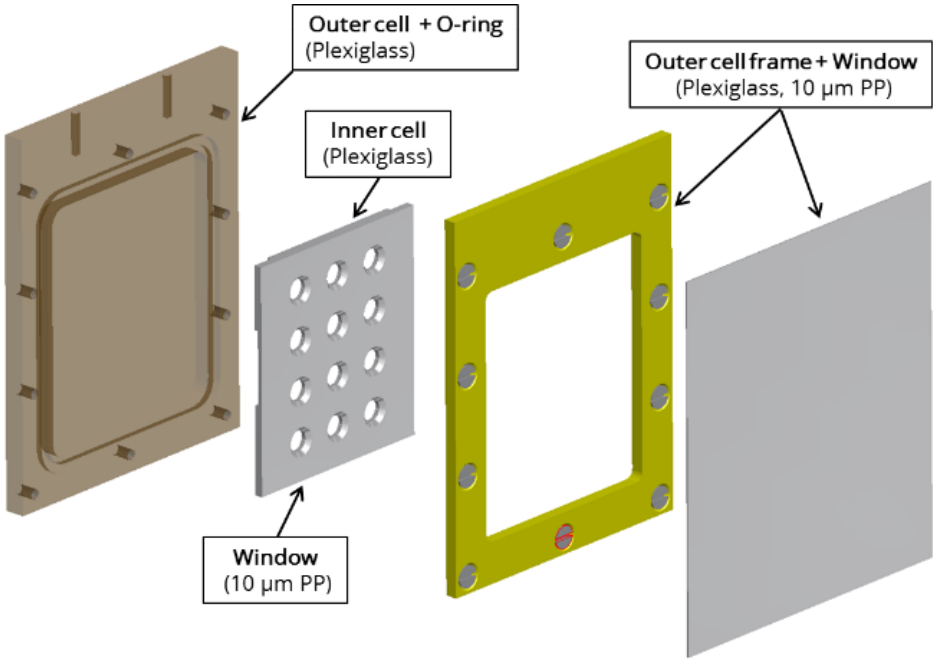

Figure 4.1.1. Design of the sample holder used for the U M_4 edge HR-XANES experiments at ESRF.

Table 4.1.2. Descriptions of the samples and lists of the applied characterization techniques.

Sample ID	Sample description	Technique / days after preparation
Um10	Suspension: 10000 ppm U, Magnetite - 4.8 g/L, pH=8.0	U M_4 edge HR-XANES / 10 U L_3 edge HR-XANES / 10 SEM / 70 U L_3 edge EXAFS / 147 Fe 2*p* XPS / 310 XRD / 10 XRD / 480
Um6	Suspension: 6000 ppm U, Magnetite - 4.8 g/L, pH=7.5	U M_4 edge HR-XANES / 10 U L_3 edge HR-XANES / 10 U L_3 edge EXAFS / 147 Fe 2*p* XPS / 10 Fe 2*p* XPS / 310 XRD / 480
Um3	Suspension: 3000 ppm U, Magnetite - 4.8 g/L, pH=7.7	U M_4 edge HR-XANES / 10 U L_3 edge HR-XANES / 10 U L_3 edge EXAFS / 147 Fe 2*p* XPS / 310 XRD / 480
Um1	Suspension: 1000 ppm U, Magnetite - 4.8 g/L, pH=7.7	U M_4 edge HR-XANES / 10 U L_3 edge HR-XANES / 10 U L_3 edge EXAFS / 147 Fe 2*p* XPS / 310 TEM / 330
Um1a	Um1 sample stored for additional 226 days outside Ar glovebox. Washed with MQ-H_2O prior HR-XANES	U M_4 edge HR-XANES / 289 U L_3 edge EXAFS / 373 XRD / 480
Umh	Suspension: 3000 ppm U, Sorbed on maghemite for 55 days. 4.8 g/L, pH=7.5	U M_4 edge HR-XANES / 10 U L_3 edge HR-XANES / 10

4.1.2. Results and Discussion

4.1.2.1. Characterization of magnetite nanoparticles

The formation of the magnetite nanoparticles can be described with the following reaction [70-72]:

$$Fe^{2+} + 2Fe^{3+} + 8OH^{-} \rightarrow Fe_3O_4\downarrow + 4H_2O \quad [\sim 1 \text{ wt \% NaCl}] \qquad (1)$$

The formation of magnetite undergoes several recrystallization steps and is schematically depicted in Figure 4.1.2. Several possible interaction mechanisms of U with iron oxide phases are also schematically shown.

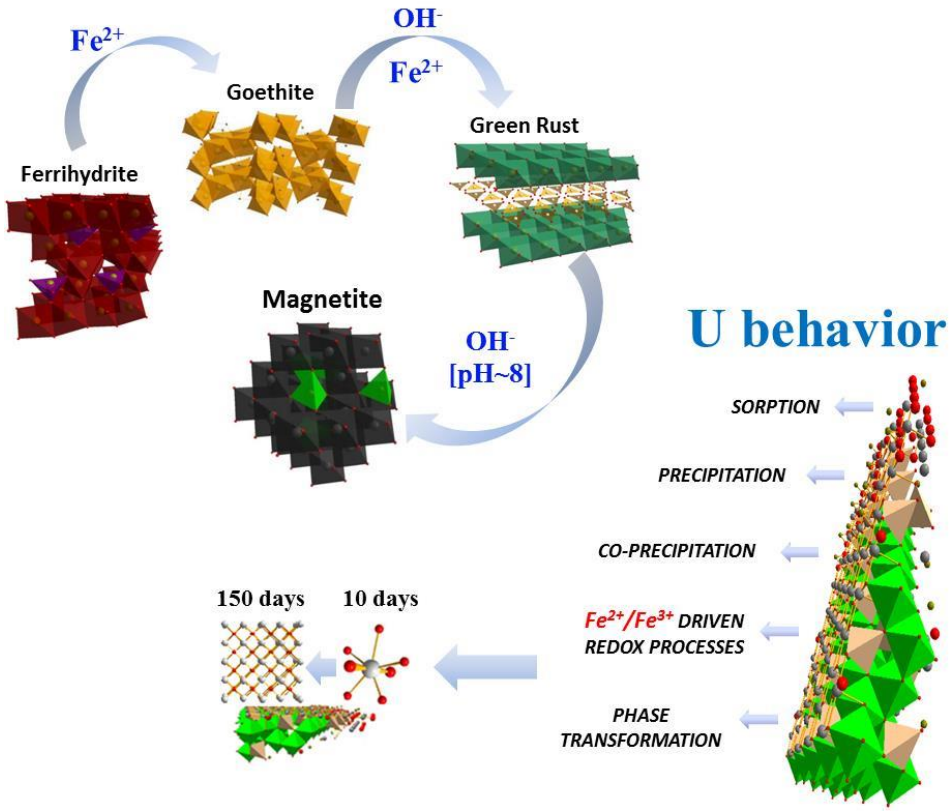

Figure 4.1.2. Schematic representation of the formation of magnetite through continuous recrystallization of Fe oxy-(hydr)oxide species and possible U interaction mechanisms with these species. [2, 73]

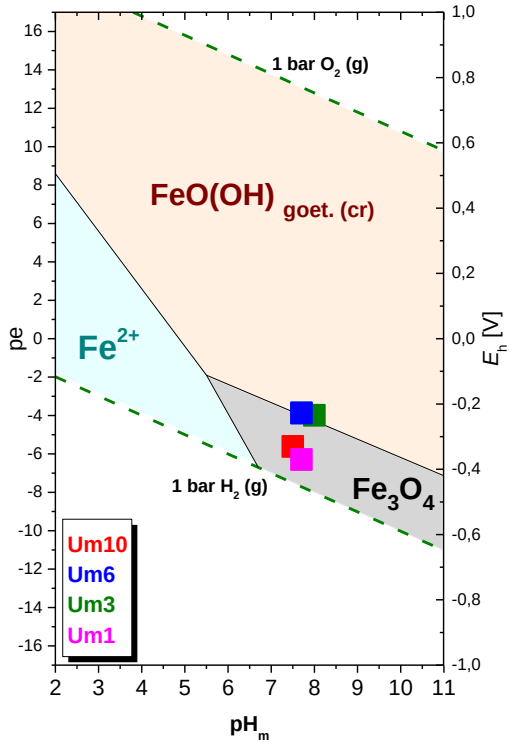

Figure 4.1.3. Fe *Pourbaix* diagram for Um1, Um3, Um6 and Um10. Symbols correspond to experimental pH and E_h measurements for Um1 - Um10 samples with $1000 \leq [U]_{tot}$ [ppm] ≤ 10000. Calculations performed with $[Fe]_{tot}$ = 0.062 M and I[NaCl] = 0.192 M (Table 4.1.1).

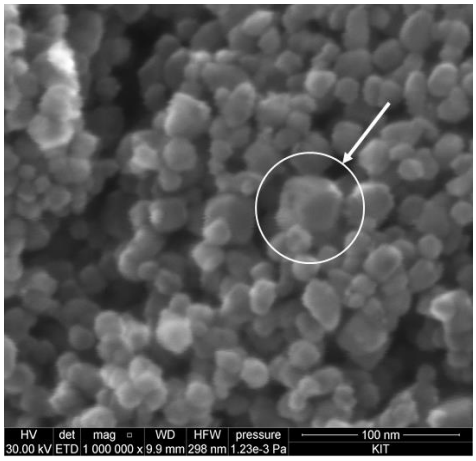

Figure 4.1.4. SEM image of Um10 (100 nm scale). An octahedrally shaped magnetite particle is circled.

The Fe *Pourbaix* diagram depicted in Figure 4.1.3 confirms that the samples containing 1000 (Um1) and 3000 (Um3) are inside the stability field of magnetite; the samples containing 6000 (Um6) and 10000 (Um10) ppm U are located at the magnetite/goethite border. Several Fe(III) oxy-(hydr)oxides phases like for example $Fe(OH)_3$(am), FeO(OH)(cr) and Fe_2O_3(cr) [73] with different degrees of crystallinity and/or crystal structures are reported in the literature as relevant products for reaction (1).

The use of (FeO(OH)(cr) in the thermodynamic modelling is favoured as it is one of the main intermediate phases forming during the magnetite nanoparticles' formation. [17] SEM image (Figure 4.1.4) and XRD patterns (Figure 4.1.5) reveal that highly crystalline magnetite nanoparticles with octahedral shape and 10-30 nm size are formed. No detectable FeO(OH)(cr) or any other Fe containing crystalline phases are found.

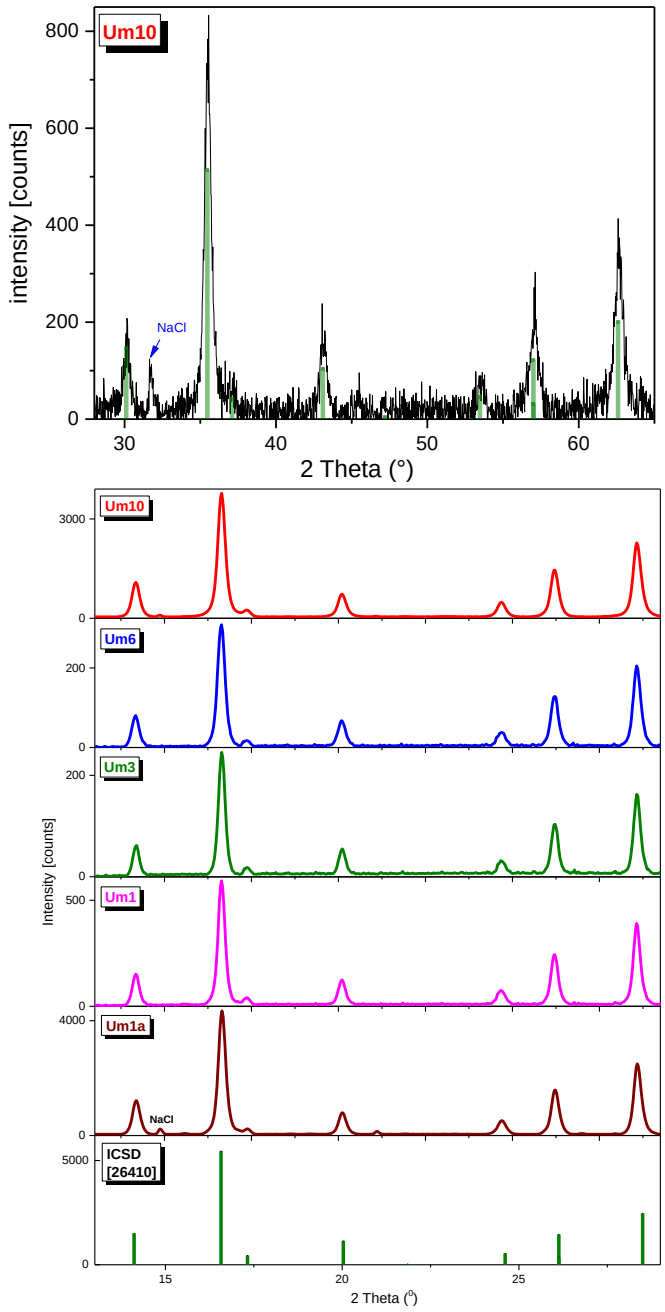

Figure 4.1.5. XRD patterns for the 10 days aged Um10 sample (top; laboratory based measurements at INE) and for the 480 days aged Um10, Um6, Um3, Um1 as well as Um1a samples (bottom; synchrotron based measurements at the SUL-Beamline, Section 3.4). Incident X-ray beams with 8.05 keV and 17.00 keV energies are used for the laboratory and synchrotron experiments, respectively. This leads to a shift of the 2 Theta angle. Reference spectra are taken from ICSD.

4.1.2.2. Redox state of Fe

Fe 2*p* XPS spectra reveal a slight decrease of Fe(II) indicated by the reduced intensity of the Fe(II) $2p_{3/2}$ peak for 310 days compared to the spectrum of a 10 days aged Um6 sample (Figure 4.1.6 b). The Fe(II) content is slightly reduced in all Um1-Um10 samples aged for 310 days to $Fe(II)/Fe_{TOT}$=28±3% compared to stoichiometric Fe_2O_3 ($Fe(II)/Fe_{TOT}$= 33±3%). The differences between the samples are within the experimental error. The analysis of the XPS spectra were performed as described in Huber *et al*. [30]

An additional approach for quantification of Fe(II) is the analyses of the pre-edge region of Fe K edge HR-XANES spectra. This method was used to quantify variations of Fe(II)/Fe(III) within several wt % in different Fe compounds and minerals. [74].

The energy distance between the main peak and the satellite peak in the emission Fe K_β spectra is smaller for Fe(II) compared to Fe(III) and has been also extensively exploited for Fe oxidation state analyses. [48, 74] In Figure 4.1.7 the Fe K edge HR-XANES (a) and Fe K_β emission spectra (b) of Fe in U co-precipitated with magnetite (Um6) are compared with spectra of magnetite ($Fe(II)/Fe_{TOT}$ = 30±3%) prepared without U, and reference spectra of materials containing Fe(II) (FeO) and Fe(III) (FeO(OH)). The FeO sample was partially oxidized prior to the experiments as indicated by the lower intensity of peak A compared to peak B in the pre-edge region of the XANES spectrum (Figure 4.1.7 a). The spectra for the Um1-Um10 samples are very similar therefore the Um6 is used here as a respective example. There is only a minor intensity difference for the pre-edge XANES spectrum and no differences for the emission lines of the Um6 sample compared to the spectrum of the Fe_3O_4 reference. Clearly, the sensitivity of the two methods is not sufficiently high to detect small variations in Fe redox states. The detection limit can be dramatically increased by using Fe $K_{\beta 1,3}$ emission satellite lines as was previously demonstrated. [48]

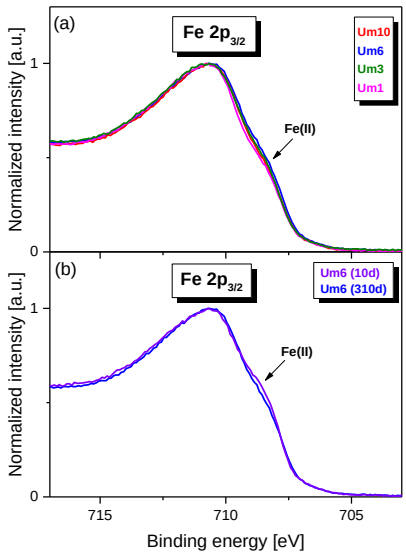

Figure 4.1.6. Fe $2p_{3/2}$ XPS spectra for Um10-Um1 samples aged for 210 days (a) and for Um6 aged for 10 and 310 days (b).

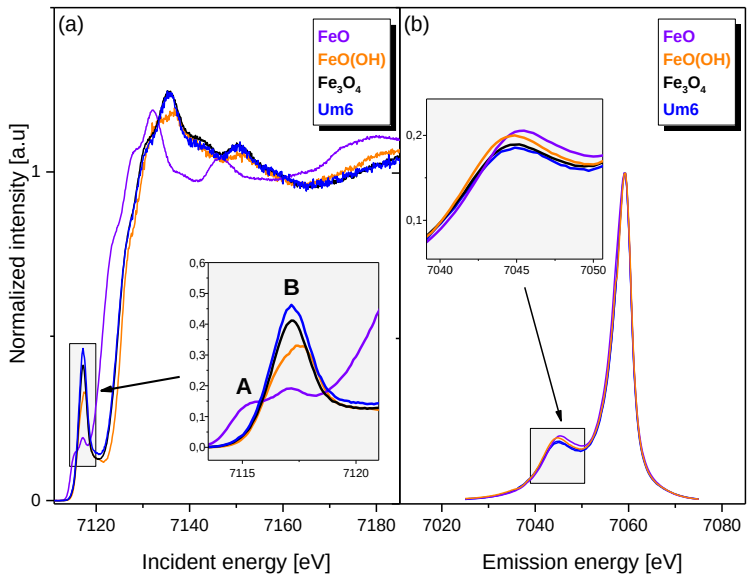

Figure 4.1.7. Fe K edge HR-XANES (a) and Fe $K_{\beta 1,3}$ X-ray emission (b) spectra of FeO, FeO(OH), Fe_3O_4 and Um6. The pre-edge regions are enlarged in the insets.

4.1.2.3. Redox state of U

The redox states of U in the Um1, Um3, Um6 and Um10 samples were characterized 10 days after the preparation of the samples by the U M_4 edge HR-XANES technique. Figure 4.1.8 depicts the U $M_{4,5}$ edge HR-XANES spectra of the Um1-Um10 samples and U_4O_9 as well as Umh with 3000 ppm U adsorbed. The latter samples are used as reference compounds.

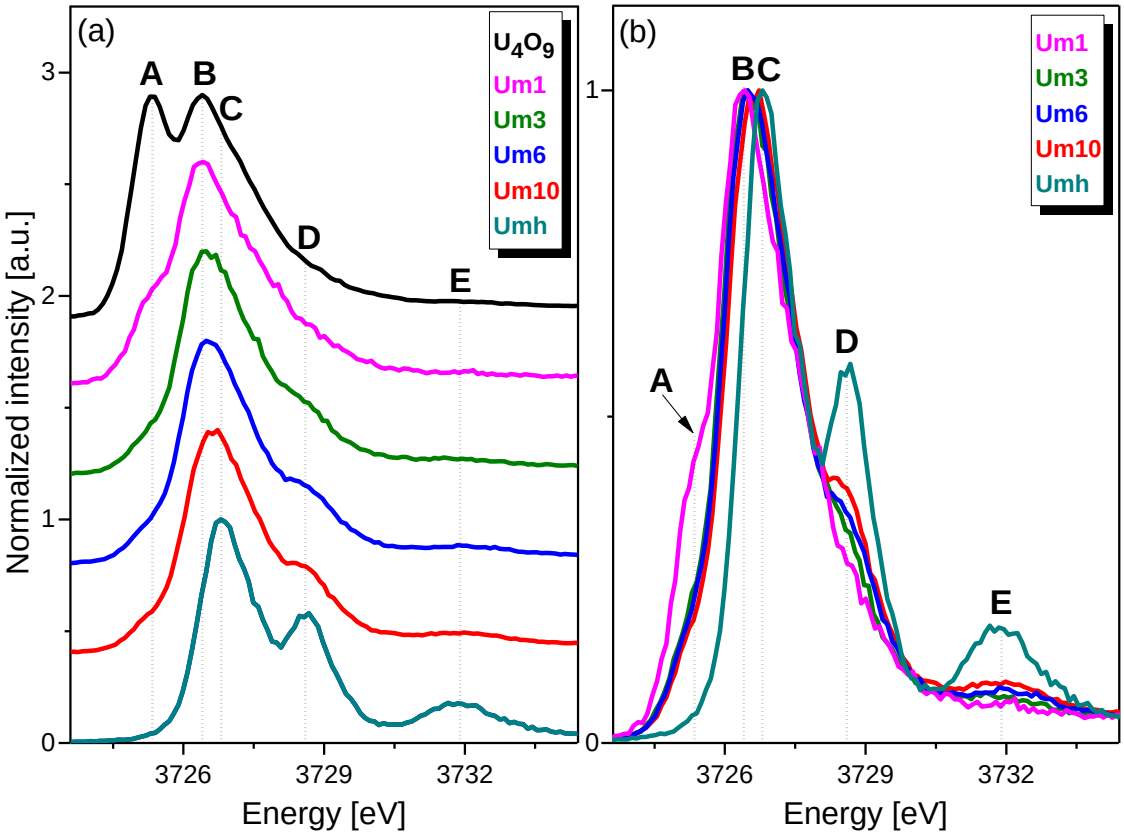

Figure 4.1.8. U M_4 edge HR-XANES spectra of the U_4O_9, Um1, Um3, Um6, Um10 and Umh samples shifted along the *y*-axis (a) and of the Um1, Um3, Um6, Um10 and Umh samples plotted without a shift along the *y*-axis (b).

The absorption spectra typically shift to higher energies by increasing the U redox state due to the reduced screening of the $3d_{3/2}$ core-hole by the decreased electronic charge density on the U atoms. Smaller energy shifts of about 0.5 eV can be caused by variations of the electronegativity of the bonding partner, changes in symmetry, short and long range atomic order etc. for the same U redox state as found in U L_3 edge XANES studies. [75, 76]

For the U M_4 edge HR-XANES method discussed here, the energy shift varies within ~0.2 eV as found from different U(V) containing organic and inorganic compounds. It was demonstrated that U_4O_9 contains equal amounts of U(IV) and U(V) described by the two peaks separated apart by ~1 eV. These spectral features are named A and B in the U M_4 edge HR-XANES spectrum of U_4O_9 (Figure 4.1.8 a). Maghemite has the same inverse spinel crystal structure as magnetite with the specificity that Fe(II) is oxidized to Fe(III). The main absorption peak C of the Umh spectrum is shifted by ~0.4 eV to higher energies as compared to peak B, which is characteristic for U(V). Hence U(VI) is the main redox state of U in the Umh sample.

Spectral features D and E are characteristic for U(VI) and U(V) forming short trans-dioxo bonds with typical lengths of < 1.77 Å and < 1.91 Å (uranyl (U-*yl*), respectively. [37, 77, 78] Peak E describes transitions of $3d_{3/2}$ electrons to σ* orbital containing a mixture of U with O valence orbitals. The π* orbitals probed by peak D contain typically also valence orbitals of equatorial ligands. [37]

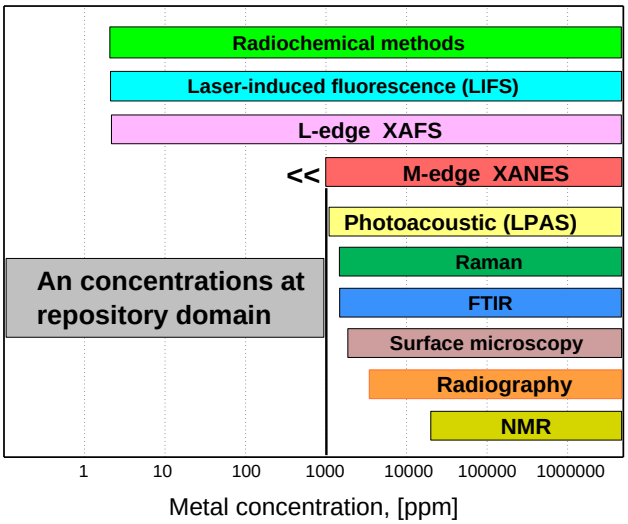

Figure 4.1.9. General schematic overview of the methods' sensitivity for speciation of An. $M_{4,5}$ edge XANES has a great potential for An speciation at much lower concentrations (Readopted from W. Runde, Los Alamos Science, 2000)

The spectrum obtained for Um1 containing 1000 ppm U demonstrates the promising capabilities of the U $M_{4,5}$ edge HR-XANES technique. Even at low *An* contents of samples in the trace concentration range, being relevant for environmental samples and studies in the context of nuclear waste disposal, speciation information can be obtained. [79, 80].

A schematic overview of the sensitivity of different methods for *An* speciation is shown in Figure 4.1.9. The energies of the two main absorption resonances of the Um1 spectrum correspond to the energy positions of the main peaks of the U_4O_9 reference spectrum (Figure 4.1.8 a). [35] Based on this strong experimental evidence we conclude that after 10 days interaction time U(V) is formed in Um1 coexisting with minor amount of U(IV) visible as a shoulder on the low energy side of the main absorption peak. Features D and E are absent in the Um1 spectrum. This confirms that U(VI) is not present in the Um1 sample and that U(V) does not form U-*yl* type of bonding.

It is evident that by going from the Um1 to the Um10 spectrum the intensity of feature A decreases, the energy position of feature B shifts to higher energies and features D and E gain intensities. These spectral changes strongly suggest that the relative contributions of U(IV) decreases, whereas the U(VI) content rises continuously going from 1000 ppm U (Um1) to 10000 ppm U (Um10) in the samples (Figures 4.1.8 b). The increase of U(VI) is attributed to the fact that the exceed of its solubility limit for U(VI) solid phases are exceeded of schoepite (~$4\cdot10^{-6}$ M) resulting in precipitation [81, 82] along with the formation of U(V) and U(IV) species.

The U M_4 edge HR-XANES technique is clearly capable of detecting the three different redox states, i.e. U(IV), U(V) and U(VI), being present simultaneously in the same sample. The measured spectra are free of artifacts induced by sample preparation since no any complex preparation is required for these and most sample systems in general. The quantitative analyses are currently under development. One of the difficulties is the challenging estimation of the absorption cross sections for the different U oxidation states.

4.1.2.4. Analysis of non-stoichiometric UO_2

The atomic environments and redox states of U in 147 days aged Um1-Um10 samples are probed by U L_3 edge XANES and EXAFS techniques.

(Figures 4.1.10 a and 4.1.11 a; Table 4.1.3).

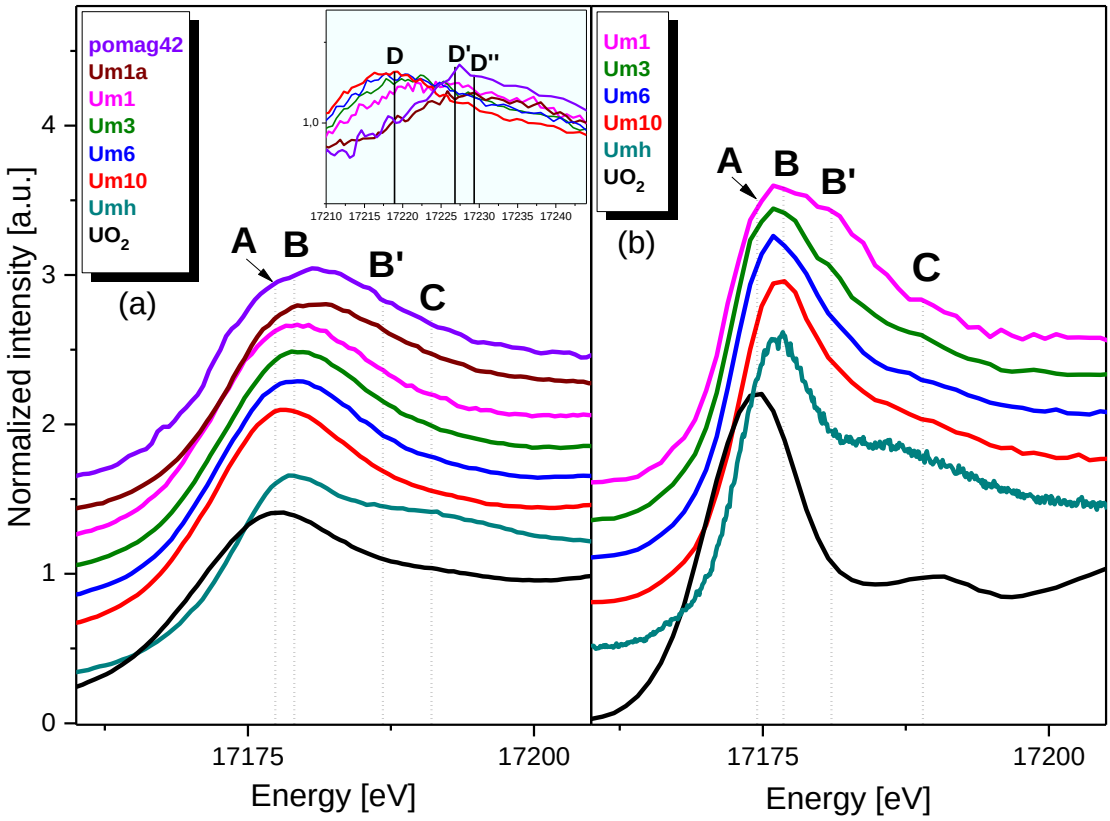

Figure 4.1.10. U L_3 edge XANES spectra of po-mag42 [30], Um1a, Um1, Um3, Um6, Um10 (aged for 147 days), Um1a (aged for 373 days including 226 days under ambient conditions), Umh (aged for 330 days), and UO_2 (a): U L_3 edge HR-XANES spectra of Um1, Um3, Um6, Um10 (aged 10 days), Umh (aged 55 days) and UO_2 (b).

The U L_3 edge XANES spectra of the Um1-Um10 samples clearly shift to lower energies on going from the Um1 to the Um10 compared to the U(VI) reference spectrum of the Umh sample revealing rising U(IV) content in the samples (Figure 4.1.10 a; discussion in the next section). U(IV) is the dominant specie in the Um10 sample. The FT-EXAFS spectra and their best fits for the Um1, Um3, Um6 and Um10 samples are depicted in Figure 4.1.11 (Figures AI.1-4).

The first coordination sphere of U is best modeled with three U-O distances (R). The obtained U-O1 R=1.69-1.73 Å is a typically short bond length for U(VI). It has been demonstrated that such peaks do not have any structural significance since they are caused by multi-electronic excitations appearing at ~10.5 $Å^{-1}$ in the EXAFS spectrum. [34, 83] In contrast, Conradson *et al.* proposed that these short U-O distances are characteristic for U(VI) in a series of UO_{2+x} compounds. [84] Herein the short U-O1 distance is considered in the EXAFS model without attempting to its interpretation; the structural parameters obtained from the fit do not change substantially with and without modeling this peak but the goodness of fit improves.

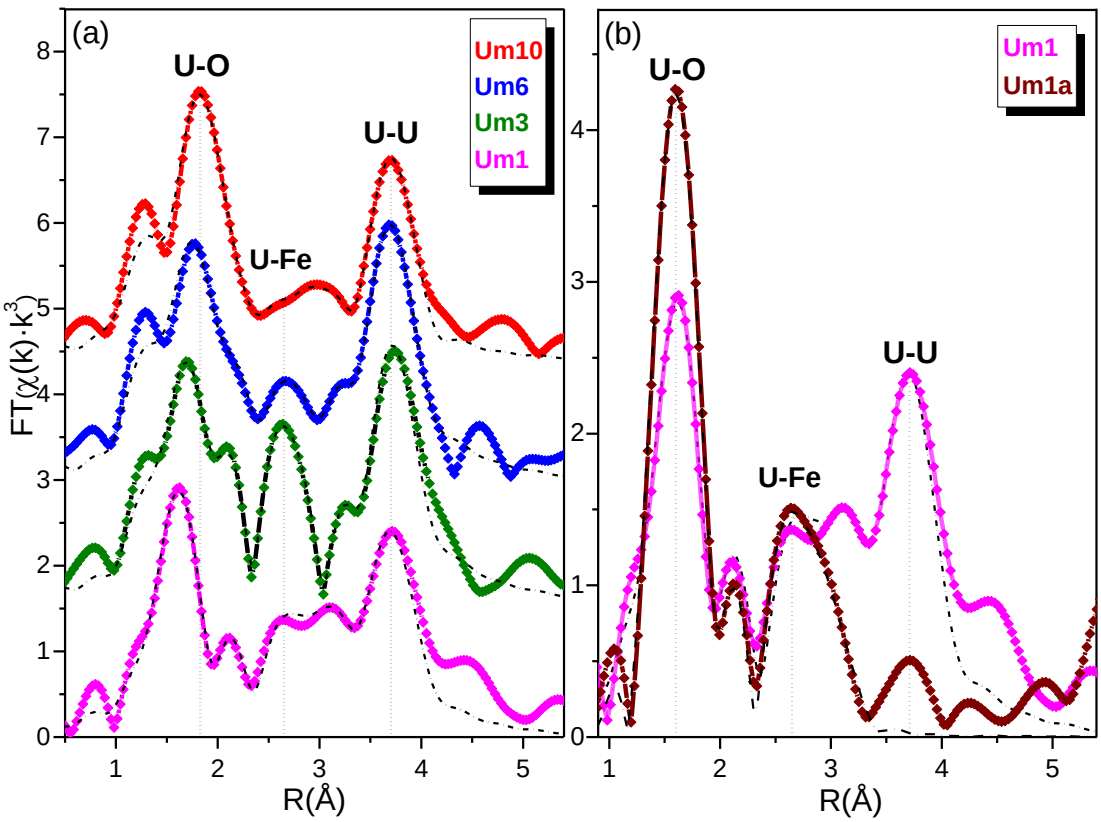

Figure 4.1.11. Magnitude of FT-EXAFS data (colored rhombs) and best fits for the Um10, Um6, Um3, Um1 (a) and Um1a, Um1 (b) samples.

The main U-O2 distance decreases continuously from 2.29(1) Å to 2.17(1) Å within the Um10-Um1 series, whereas U-O3 remains within the region R=2.38(2)-2.44(2) Å (Table 5.1.3 and Figure AI.4).

The coordination numbers (N) vary N=0.2(1)-0.4(1), N=2.7(3)-3.0(3) and N=1.7(1)-2.4(1) for O1, O2 and O3, respectively (Table 4.1.3 and Figure AI.4). It was reported that for increasing x in UO_{2+x}, the first O coordination sphere of U splits to two dominant peaks similar to the results presented here. [84]

Table 4.1.3. EXAFS fit results for Um10, Um6, Um3, Um1 and Um1a samples (SP denotes scattering path, N – coordination number, R – bond distance, σ^2 - Debye-Waller factor, ΔE_0 – energy shift, S_0^2 – amplitude reduction factor and r - goodness of fit parameter. Errors are given in the parentheses as the last decimal in the fit value. ^{t} - parameters were fixed after obtaining the best fit).

Sample/ Parameter	SP	N	R, [Å]	$\sigma^2[\cdot 10^{-3}Å^2]$	ΔE_0, [eV]	S_0^2	r, [chi^2]
Um10	U-O1	0.4 (2)^t	1.73 (3)	6 (1)	7.3 (3)	0.77	0.004
	U-O2	2.9 (2)	2.29 (1)	6 (1)			
	U-O3	2.1 (2)	2.44 (2)	6 (1)			
	U-Fe1	1.2 (4)	3.14 (2)	13 (4)			
	U-Fe2	0.5 (2)^t	3.45 (2)	4 (3)			
	U-U1	5.2 (8)	3.84 (1)	6 (1)			
Um6	U-O1	0.4 (1)^t	1.69 (2)	6 (1)	7.0 (4)	0.77	0.004
	U-O2	2.7 (3)	2.25 (1)	6 (1)			
	U-O3	1.7 (1)	2.38 (2)	6 (1)			
	U-Fe1	2.7 (5)	3.13 (2)	6 (2)			
	U-Fe2	0.6 (3)^t	3.50 (2)	5 (3)			
	U-U1	3.6 (6)	3.83 (1)	2 (1)			
Um3	U-O1	0.3 (1)	1.70 (1)	6 (1)	7.2 (3)	0.77	0.004
	U-O2	2.8 (3)	2.22 (1)	6 (1)			
	U-O3	2.4 (1)	2.43 (2)	6 (1)			
	U-Fe1	3.4 (6)	3.13 (1)	13 (1)			
	U-Fe2	0.6 (3)^t	3.34 (2)	6 (4)			
	U-U1	3.2 (7)	3.84 (1)	2 (1)			
Um1	U-O1	0.2 (1)^t	1.73 (3)	6 (1)	6.8 (9)	0.77	0.008
	U-O2	3.0 (3)	2.17 (1)	6 (1)			
	U-O3	1.7 (1)	2.38 (2)	6 (1)			
	U-Fe1	4.9 (8)	3.18 (2)	18 (2)			
	U-Fe2	0.6 (3)^t	3.55 (3)	1 (1)^t			
	U-U1	2.9 (7)	3.85 (1)	2 (1)			
Um1a	U-O1	0.7 (2)	1.79 (1)	4 (1)	5.0 (9)	0.77	0.008
	U-O2	3.3 (3)	2.13 (1)	4 (1)			
	U-O3	0.8 (1)^t	2.40 (1)	4 (1)			
	U-Fe1	5.0 (6)	3.19 (1)	17 (2)			

The observed trend for these two main U-O distances is reverse compared to our EXAFS results since R(U-O) grows as a function of the increasing non-stoichiometric oxygen in UO_2 (R(U-O2)=2.17-2.29 Å, R(U-O3)=2.38-2.44 Å). [84] This can be explained by the presence of a second U(V) site becomes significant as a function of the decreasing U concentration in the discussed samples in addition to the potential U(V)/U(VI) constituent of the UO_{2+x} particles. This U(V) site has major participation in the Um1 sample. The U-O2 distance R=2.17(1) Å for the Um1 sample is within the bond length region (2.10-2.20 Å) most typical for U(V) compounds reported in the literature. [16] In contrary, the UO_{2+x} species dominates in the Um10 sample and its fraction decreases when going from the Um10 to the Um1 sample. The interatomic distances in the Um10 sample are closest to the structural parameters obtained for the $UO_{2.20}$ sample studied by Conradson *et al*. [84]; this is the sample with the highest fraction of excess oxygen (x=0.2). Based on XANES analyses, the authors claim U(IV) and U(VI) as main contributions in this sample. However, they do not consider that the U L_3 edge XANES spectrum of U(V) uranate (U-*ate*) can be shifted to higher energies compared to the UO_2 WL position. [75, 84]. It has been also shown with the help of U M_4 edge HR-XANES that U_4O_9 (x=0.25) and U_3O_8 (x= 0.67) contain U(IV), U(V) and U(V) and U(VI), respectively. The U L_3 edge XANES data differs from the spectra presented by Conradson *et al.* since there is about 4 eV energy shift of the WLs to higher energies of the spectra compared to the UO_2 reference (Figure 4.1.10 a). This shift might be caused by the presence of U(V)/U(VI) in UO_{2+x} and/or due to the U(V) specie incorporated in octahedral sites in magnetite (see the Results and Discussions below). The presence of UO_{2+x} in the Um1-Um10 samples is also supported by the intense peak at about 3.84 Å characteristic for the scattering of the photoelectron from U atoms in the second coordination sphere of U. The U coordination numbers vary between about N=2.9(7)-3.6(6) (Um1, Um3 and Um 6) and N=5.2(8) (Um10).

All N are strongly reduced compared to bulk UO_2 (R(U-O2)=2.36 Å and N=8; R(U-U1)=3.88 and N=12) likely due to structural disorder caused by the large contribution of U surface atoms in the small nanoparticles and increase of non-stoichiometry of UO_2. [84, 85]

TEM analyses clearly detect crystalline nanoparticles with size of about 4-5 nm possibly grown on the surface of the magnetite particles (Figure 4.1.12) with lattice parameters very close to stoichiometric UO_2. Due to the relatively large error bars for the obtained lattice parameters (*a* = 0.271±0.004 nm) it is not possible to distinguish between UO_2 and UO_{2+x} hence we conclude that they are both likely.

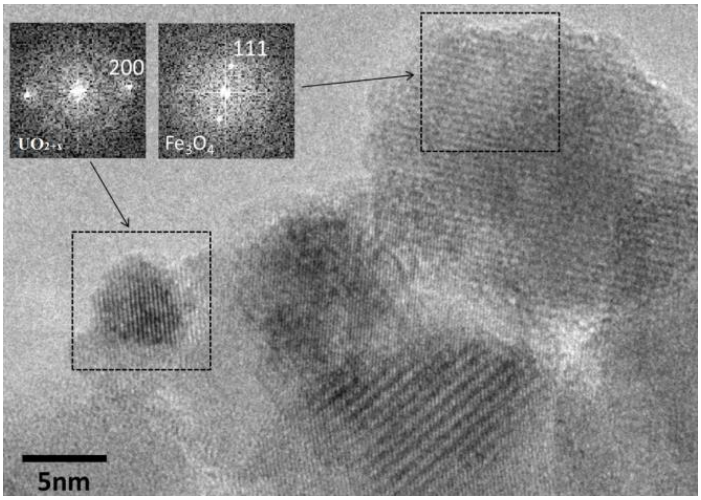

Figure 4.1.12. High-resolution TEM image of Um1 (aged 330 days).

U(VI) species detected by the U M_4 edge HR-XANES technique after 10 days interaction time of U with the magnetite nanoparticles are clearly reduced predominantly to U(IV) after 147 days. No significant redox changes are found for Um1 (see also the discussion below). It can be concluded that the EXAFS and the HR-XANES results confirm major U(V) and U(IV) contributions in the Um1 sample 10 and 147 days after the preparation of this sample. The U L_3 edge XANES, EXAFS and TEM results suggest presence of UO_{2+x} nanoparticles with 4-5 nm size and U(V) incorporated into the structure of magnetite in the Um1-Um10 samples. No indications for U(VI)/U(V)-*yl* are found (Figure 4.1.11 a,b).

4.1.2.5. U(V) incorporated in Fe octahedral sites of magnetite

The U L_3 edge HR-XANES spectra measured for the 10 days aged samples Um1-Um10 and spectra of the UO_2 and Umh reference compounds are depicted in Figure 4.1.10 b. Feature C clearly visible in the Umh spectrum is characteristic for U(VI)-*yl*. It has smeared-out intensity in the spectra of the Um3-Um10 samples and it is missing in the spectrum of the Um1 sample. This result clearly demonstrates that U-*yl* type of bonding is not significantly contributing in these materials as confirmed also by the U M_4 edge HR-XANES analyses of the Um1-Um10 samples (Section 4.1.2.3). The WLs of the spectra of the Um1-Um10 samples are shifted to higher energies compared to the UO_2 spectrum and coincide with the U(VI) reference compound (Umh). In addition, feature B' increases in intensity from the Um10 to the Um1 spectrum and the WL becomes broader. The spectrum of the Um1 sample has well pronounced A and B' shoulders previously described as characteristic for U(V). [75] These experimental evidence strongly suggest an increasing contribution of U(V) in an octahedral environment, which dominates in the Um1 sample.

Existence of U(V) in octahedral environment is also supported by the U L_3 edge XANES spectra measured for samples Um1-Um10 aged 147 days and Um1a aged 373 days. The spectra of the Um1-Um10 samples exhibit a trend and clearly shift to higher energies compared to UO_2. The WL becomes broader and the post-edge absorption resonance at about 17191 eV transforms from a single asymmetric to symmetric double peak (Figure 4.1.10 a). For comparison, the spectrum published by Huber *et al.* is also plotted where a presence of U incorporated in octahedral environment was reported. [30] In contrast, the spectrum of the Um1a sample shifts to higher energies compared to the Umh reference, the A and B` shoulders and the shift of the post-edge resonance to higher energies further indicate that U is likely incorporated in octahedral sites in the magnetite.

The shift to higher energies is about 2 eV compared to the spectrum of U(VI)-*yl*, which is more characteristic for U(V) in octahedral/distorted octahedral and generally U-*ate* type of bonding. [75, 86] U(VI) with such local atomic environments would be positioned at least 3 eV compared to the WL maximum of U(VI)-*yl*. [87] This shift can be also partially caused by the minor U(VI)-*yl*, found to have minor contribution in this sample (Figures 4.1.10 a).

The best fits to the FT-EXAFS spectra also reveal coordination of U to Fe atoms, which is most prominent for the Um1 sample.

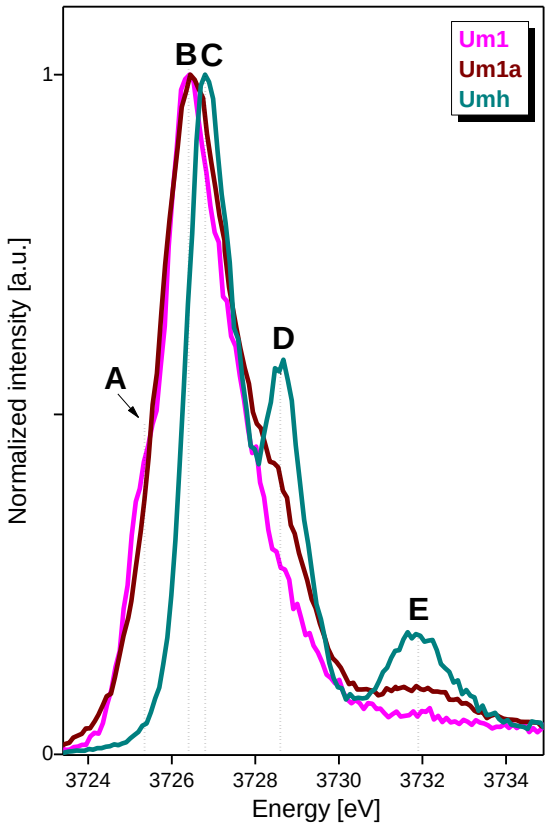

Figure 4.1.13. U M_4 edge HR-XANES spectra of Um1, Um1a after 147 days (measured at the INE-Beamline) and Umh after 373 days.

Two U-Fe interatomic distances are resolved: U-Fe1, R=3.14(2), N=1.2(4) (Um10) – R=3.18(2), N=4.9 (8) (Um1) and insignificant contribution of a U-Fe2 shell with coordination numbers of about 0.5 (Table 4.1.3). Somewhat longer R (+ 0.04 Å) and N (fixed at 6) for U-Fe have been previously reported for U incorporated in Fe octahedral sites. [18] The octahedral and tetrahedral Fe sites of magnetite have R=2.97 Å, N=6 and R=3.48 Å, N=4, respectively. Based on the obtained results from experiments and modeling we propose that the second U(V) species, different from the U(V) constituent of the UO_{2+x} particles, are incorporated in the magnetite structure in octahedral Fe sites. [18] The EXAFS and HR-XANES analyses of the spectra of the Um1a sample strongly support this hypothesis.

The FT-EXAFS spectra of the Um1 and Um1a samples are compared in Figure 4.1.11 b.

It is apparent that the peaks characteristic for the U coordination to O (R(U-O1)=2.13(1) Å, N=3.3(3); R(U-O2)=2.40(1) Å, N=0.8(1) and Fe (R(U-Fe1)=3.19(1) Å, N=5.0(6)) are preserved, whereas the peak describing the coordination to U is absent in the FT-EXAFS Um1a spectrum. The U(IV) is likely to be oxidized to U(VI)-*yl* as suggested by the U-O1 bonding distance R=1.79(1) Å, N=0.8(1).

The disappearance of the peak characteristic for U at about 3.84 Å can be explained by increased disorder during the partial oxidation of U leading to distractive interference of the scattered photoelectron waves. It is remarkable that R for the main U-O2 distance decreases to 2.13 Å for the Um1a sample compared to R=2.17 Å for the Um1 sample. This result implies further stabilization of U(V) within the magnetite structure with U-O distance reported for U(V) in magnetite. [16] The HR-XANES supports this EXAFS result. The shoulder characteristic for U(IV) is not visible, whereas features D and E typical for U(VI)-*yl* appears in the U M_4 edge HR-XANES spectrum of Um1a (Figure 4.1.13). The main peak maximum has energy position very similar to Um1, which strongly suggests that the main redox state of U is U(V) (Figure 4.1.8). The stability of U(V) upon exposure to air (Um1a sample) can be explained by its incorporation into the octahedral sites of magnetite. It is possible that the surface of the magnetite is oxidized while the bulk of the material remains unchanged. This hypothesis is corroborated by the XRD results since the XRD patterns of the Um1 and the Um1a samples are very similar and typical for the structure of magnetite (Figure 4.1.5). The small contribution of the possible surface species is not detected by XRD.

4.1.3. Conclusion

This study demonstrates for the first time that the HR-XANES technique is capable for detection of three different oxidation states of U: U(IV), U(V) and U(VI) simultaneously present in the same sample. It is revealed that U with concentrations above the solubility limit (~$3 \cdot 10^{-6}$ M) precipitates in U(VI) phases found for 10 days aged Um3-Um10 samples. These U(VI) phases transform to UO_{2+x} clusters with ~5 nm size grown on the magnetite nanoparticles as revealed for the 10 and the 147 days aged samples. These are strong evidences that the recrystallization process has slow kinetics and needs more than 10 days to complete. There is no clear U-U coordination visible in low quality FT-EXAFS data (not shown here) for the 10 days aged samples. Therefore it is likely that the initially found U(IV) is either not a component of UO_{2+x} particles or respective solid phases are strongly disordered. In addition, it is revealed that a U(V) specie is stabilized in the Um1-Um10 samples and represents a main constituent of the Um1 sample during the probed time period from 10 to 373 days. It is found that the U(V) is incorporated in the Fe octahedral sites of magnetite for 147 and 373 days aged samples. E_h measurements suggest that the U should be reduced to U(IV) state. Apparently, the solid phase structures seem to stabilize incorporated U(V) species. The U(V) remains stable even upon oxidation of the magnetite for 226 days. One possible hypothesis is that oxidized surface layers of the magnetite particles protect the U(V) species incorporated in the magnetite structure from oxidation. Variations in the solid surface Fe speciation as a function of time and U concentration will be studied in future investigations combining SEM, TEM and spectroscopic techniques.

The presented results are a breakthrough in a long and intensive discussion on the reduction mechanisms of U(VI) in contact with magnetite. The proposed U M_4 edge HR-XANES technique demonstrates its strong capability for redox studies of *An*.

4.2. Influence of Fe(II) on the redox state of U sorbed on magnetite

This section discusses the influence of aqueous Fe(II) on the U redox states of U sorbed for 175 days on magnetite nanoparticles. Results obtained from U L_3/M_4 edges HR-XANES and U 4*f*, Fe 2*p* XPS techniques are presented. The sensitivities of the three methods are compared. The concentration of [U]=$3\cdot10^{-5}$ M in the pH range of 7.0-7.5 is higher than the solubility limit of U(VI) (i.e. schoepite [81]) and is higher than those usually taken for geochemical studies (10^{-6}-10^{-11} M), [88] but well above the detection limits of the XPS and HR-XANES techniques. It can be argued whether the prepared samples are relevant for naturally occurring conditions. Results from spectroscopic investigations of such samples can nevertheless help to verify thermodynamic speciation calculations, which in turn might be transferred to U speciation predictions for concentrations ranges relevant to environmental conditions. The presented experiments can also serve as proof of principle experiments needed to establish reliable experimental protocols for future investigations including environmentally relevant U concentrations. [33]

4.2.1. Materials and Methods

4.2.1.1. Preparation and analyses of the magnetite nanoparticles

The magnetite nanoparticles were prepared by reaction of $FeSO_4$ with KOH and KNO_3 [89] under Ar atmosphere in a glovebox. Freshly prepared magnetite suspension was dialyzed against deionized water until the electric conductivity was comparable to that in deionized water (4 µS/cm). The magnetite concentration in the prepared suspension was 50.5 g/L. The magnetite suspension was stored in Nalgene bottles in a glovebox under Ar atmosphere prior the batch experiments. Maghemite was prepared by heating the freeze-dried magnetite suspension in a dry box at 250 °C for 2 h under ambient conditions.

XRD and SEM have been performed as discussed in Sections 3.4 and 3.5.

The specific surface area of the nanoparticulate magnetite was determined by Brunauer–Emmett-Teller (BET) N_2-adsorption (AUTOSORB-1, Quantachrome Corporation). The freeze-dried magnetite suspension was heated under anoxic conditions to 80 °C and degassed for 60 min. The determination of the surface area was done via the multiple-point method at different pressures and a subsequent fit with BET isotherm.

4.2.1.2. U(VI) batch sorption on magnetite/maghemite

The batch sorption experiments were conducted in a glove box under Ar atmosphere (< 2 ppm O_2) at room temperature (25 °C). Magnetite suspension (2 g/L) was prepared in 125 mL Nalgene vial by diluting magnetite stock suspension (50.5 g/L) with Ar purged MQ water (18 µS/cm). A background electrolyte NaCl concentration was adjusted to 0.02 M. U(VI) as uranyl chloride (pH~2.5) was added by small portions to the magnetite suspension to avoid individual U(VI) phases precipitation. The final U concentration ([U]) was $3 \cdot 10^{-5}$ M. (U(VI) solubility limit is ~$4 \cdot 10^{-6}$ M [81]) The pH value of a resulting suspension was immediately adjusted to approximately neutral pH variations were continuously recorded during the experiment with a digital pH-meter equipped with Thermo-Scientific pH electrode. The maghemite batch experiment was performed in the same way as that of magnetite.

E_h was recorded for each pH measurement by a Pt combined Metrohm electrode. Before pH-E_h measurements, the bottle with the magnetite/maghemite suspension was shaken and measurements were performed after sedimentation of the nanoparticles. E_h measurements were recorded only after 10 minutes while gently stirring the suspension due to the drift of E_h in first minutes of the measurement.

After 175 days of interaction time a calculated amount of aqueous Fe(II) (0.36 mg) was added to a 5 ml portion of batch suspension to recrystallize magnetite closer to its stoichiometric Fe(II)/Fe_{TOT} ratio of 0.33. The amount of Fe(II) was estimated by analyzing XPS spectra measured for as prepared and reacted magnetite. For spectroscopic analysis, the solid phase was separated from the supernatant by using a magnet inside the glovebox and prepared for XPS and HR-XANES measurements.

4.2.1.3. Spectroscopic measurements

The Um175 and Um175f samples were studied by XPS analysis of the U 4*f* and Fe 2*p* electron binding energies as well as by U M_4/L_3 edges HR-XANES spectroscopic techniques as described in Sections 3.2 and 3.3. Table 4.2.1 summarizes the samples investigated in the present study.

4.2.2. Results and Discussion

Well-shaped magnetite crystals with average particle size of 100 nm are formed with a minor contribution of goethite precipitating as needle-like crystals on the surface of the magnetite nanoparticles (Figure 4.2.1). Powder XRD analyses confirm the formation of the magnetite and maghemite particles used for the batch sorption experiments (Figure 4.2.2).

U is quantitatively removed from solution by magnetite after 29 days of interaction time. There are two most likely mechanisms for U(VI) removal including its sorption on the surface of the magnetite and precipitation as a solid mineral phase. U(VI) can be reduced to form mixed U(IV)/U(V) or U(VI)/U(V) oxy-(hydr)oxide species. [90] It has been shown that U removal strongly depends on pH, initial U concentration, U/Fe_3O_4 mass ratio, Fe(II)/Fe(III) ratio and E_h value. [30] In this work the pH was kept constantly at 7±0.5 to prevent removal of Fe(II) from the magnetite structure. According to the *Pourbaix* diagram (Figure 4.2.3) for $[U]=3\cdot10^{-5}$ M and 0.01 M NaCl as a background electrolyte, U is expected to precipitate in the form of $UO_3\cdot1\text{-}2H_2O$. One has to note, that magnetite is under those conditions not stable and might convert at the surface to maghemite. Only in the experiment where Fe(II) is added, pe value is in a range where magnetite can be stabilized. In Table 4.2.1 descriptions of the samples and the spectroscopic techniques used are summarized.

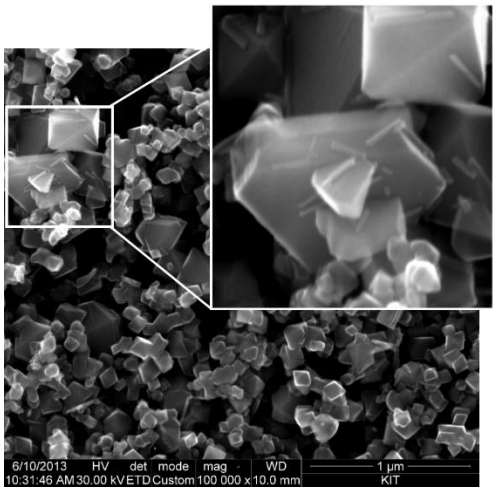

Figure 4.2.1. SEM image of magnetite.

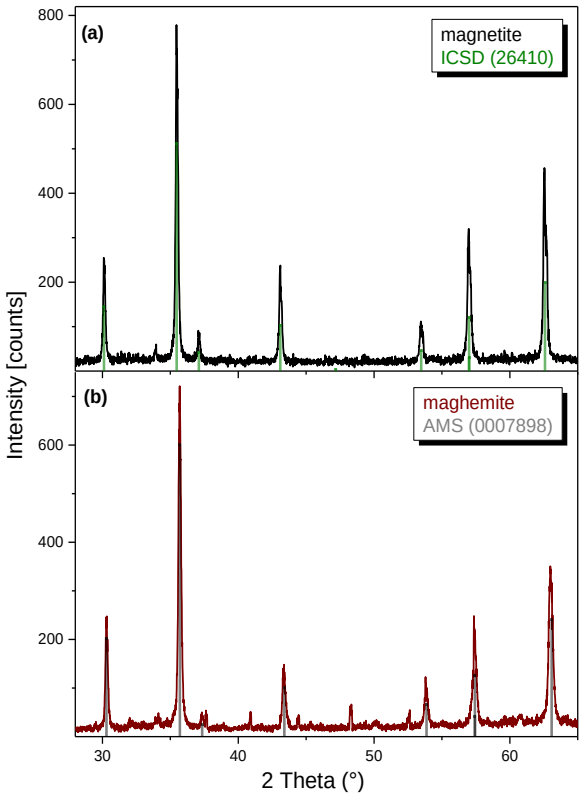

Figure 4.2.2. XRD patterns of magnetite (a) and maghemite (b) nanoparticles. The most intensive peak has a shift characteristic for the structure of maghemite. ICSD 26410 and AMS (0007898) XRD patterns are used as references.

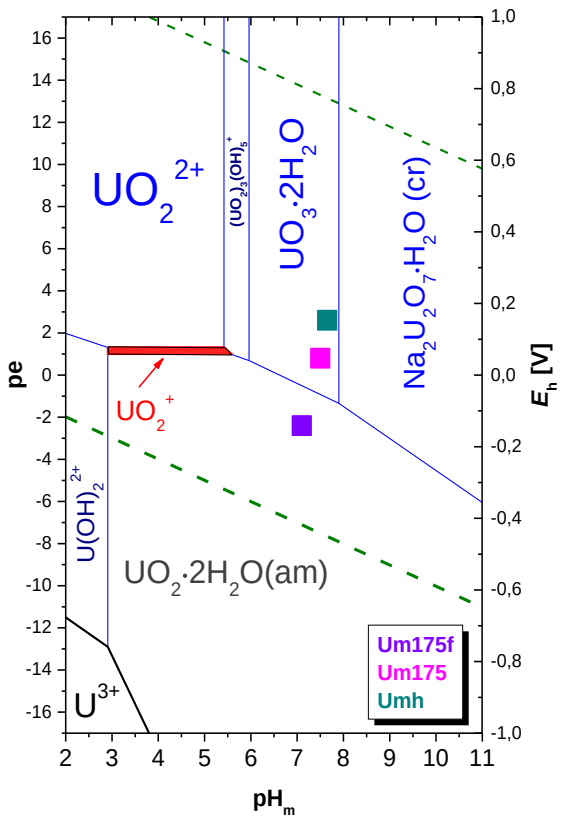

Figure 4.2.3. U *Pourbaix* diagram. The symbols correspond to experimental pH and E_h measurements for the Um175f, Um175 and Umh samples ($[U]_{tot} = 3\cdot10^{-5}$ M and I[NaCl] = 0.01 M).

Table 4.2.1. Name of samples and spectra, contact time of U with magnetite, amount of U removed by magnetite and maghemite for suspension containing $[U]=3\cdot10^{-5}$ M and [NaCl]=0.01 M, pH, E_h values and applied spectroscopy techniques.

Short name	Contact time, day	U removed, %	pH	E_h, mV	Technique
Um175	175	99.5	7.5	50	U M_4/L_3 edges HR-XANES, U 4*f*, Fe 2*p* XPS
Um175f	175 + 2 days with Fe(II)	99.5	7.1	-150	U M_4/L_3 edges HR-XANES, U 4*f*, Fe 2*p* XPS
Umh	55	99	7.7	160	U M_4/L_3 edges HR-XANES

4.2.2.1. U 4*f* and Fe 2*p* XPS

The O 1*s* binding energy at 530.2 eV was used to calibrate the energy positions of the U 4*f* peaks measured for the same sample. The U $4f_{5/2}$ and $4f_{7/2}$ XPS spectra for the Um175 and Um175f samples are depicted in Figure 4.2.4 a,b. Both spectra exhibit double peaks. The fitting of the spectra reveal that the two peaks part of the $4f_{7/2}$ spectrum have 380.5 eV and 381.8 eV energy positions characteristic for U(V) and U(VI), respectively. This result agrees with previous reports. [16] For the Um175f spectrum the intensities of the U(V) main peaks and the satellite structures clearly have risen after addition of Fe(II) to the Um175 sample, whereas the U(VI) peaks have reduced intensities (Figure 4.2.4 a,b). The best fit to the spectra reveal ~45% and ~55% U(V) for the Um175 and the Um175f samples, respectively. No main or satellite peaks characteristic for U(IV) are visible in any of the spectra, which is also not to be expected at the relatively high pe values. The amount of structural Fe(II) in the reacted magnetite is decreasing as can it be seen from the decreasing intensity of the Fe(II) peak at ~708.0 eV (Figure 4.2.4 c). At the same time, the intensity of the Fe(II) satellite peak (~716.5 eV) is increasing in the Um175f sample. This might indicate that the added $Fe(II)_{aq}$ preferably adsorbs on the surface of magnetite without significant structural rearrangement at nearly neutral pH values or the lower pe value of the suspension stabilizes the magnetite. [91] A recent study has shown that $Fe(II)_{aq}$ ions only exchange with structural Fe(II) in magnetite maintaining the Fe(II)/Fe(III) ratio close to close to the stoichiometric. [92] However, it is also shown that $Fe(II)_{aq}$ added to non-stoichiometric magnetite leads to the conversion to the compound with stoichiometric composition. [46] Recrystallization processes induced by addition of Fe(II) can, to some extent, promote the U(V) incorporation into octahedral magnetite sites as has been shown recently for ferrihydrite with sorbed U(VI). [17]

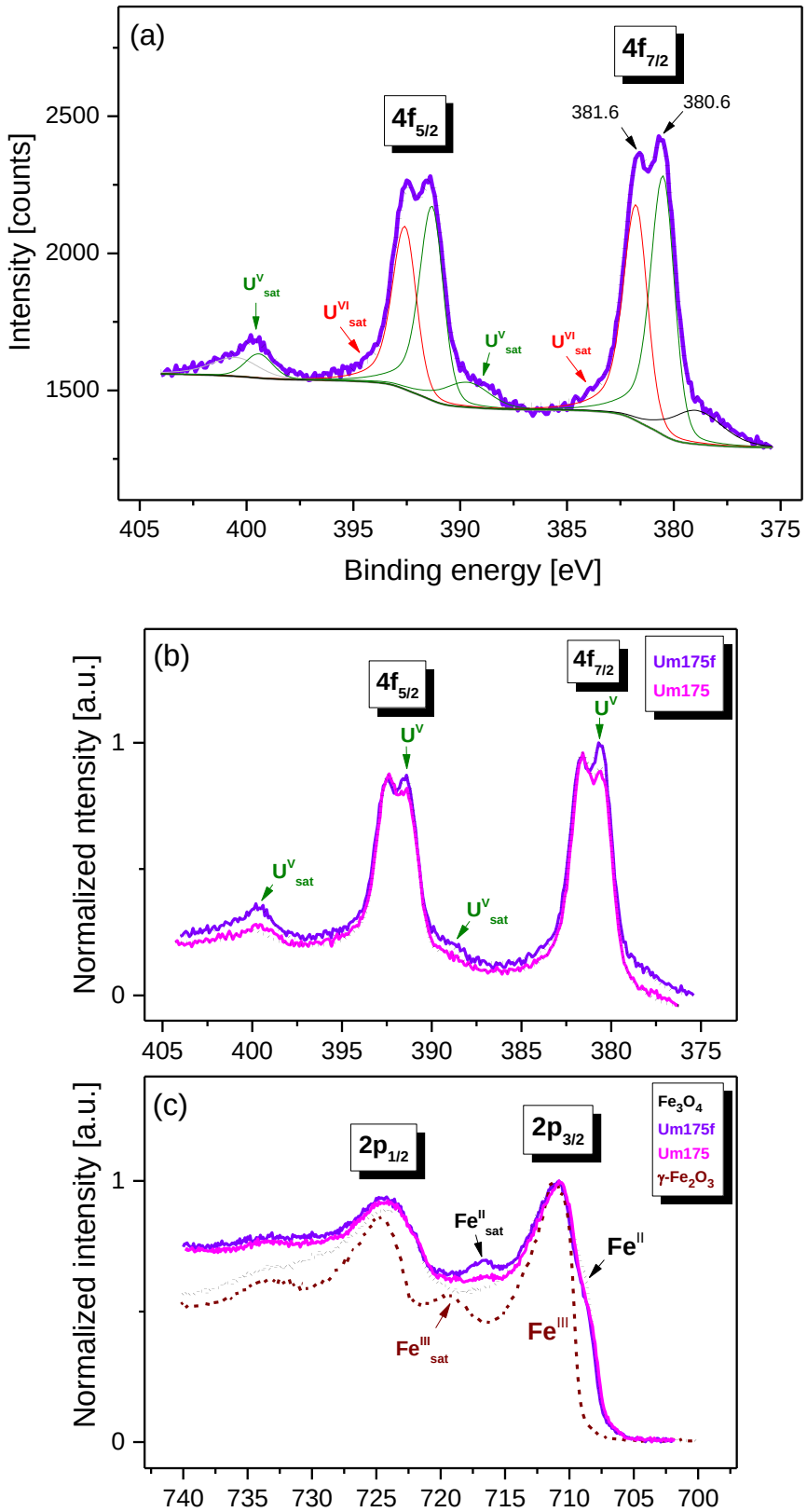

Figure 4.2.4. U 4*f* XPS spectrum of Um175f (violet) and its best fit (black) (a). Spectral features characteristic for U(V) and U(VI) are shown with green and red lines, respectively. U 4*f* XPS spectra of Um175f and Um175 (b). Fe 2*p* XPS spectra of stoichiometric Fe_3O_4, Um175f, Um175 and γ-Fe_2O_3 (c).

4.2.2.2. U L_3 edge HR-XANES

The U L_3 edge HR-XANES spectra of the Um175 and Um175f samples and the U_4O_9 and Umh reference materials are depicted in Figure 4.2.5 a',b'. The Umh sample contains only U(VI) as indicated by the 1.6 eV energy shift of the WL compared to the WL in the U_4O_9 spectrum. It has been shown that U_4O_9 consists of 50% U(IV) and 50% U(V). [35] The energy positions of the WLs of the spectra of the Um175 and Um175f samples and the Umh reference are very similar. The WLs are much broader and the post edge features at about 17186.5 eV are smeared out for the Um175 and Um175f spectra. These features are characteristic for the multiple scattering of the photoelectron from the two axial O atoms part of U(V)/U(VI)-*yl* short covalent bonds. The results suggest that the U(V) found by the XPS studies potentially present in the Um175 and Um175f samples does not form a uranyl type species. The U L_3 edge XANES for U(V)-*yl* shifts typically to lower energies compared to the U(VI)-*yl* spectrum. U(V)/U(VI) can form long bonds with O > 2 Å which are often assigned to uranate species. In this case a shift of the spectrum to higher energies compared to U(VI)-*yl* is observed. [30, 75] The broadening of the WL can be also caused by disorder effects due to large distribution of U(VI)-O_{axial} distances. Mixtures of U redox states often lead to ambiguous results by analyses of U L_3 edge XANES spectra due to the predominance of broad spectral features. The U L_3 edge HR-XANES technique is more sensitive compared to the conventional method but as it is demonstrated here, it is limited due to the still high core-lifetime broadening strongly contributing to the spectrum.

4.2.2.3. U M_4 edge HR-XANES

Compared to the U L_3 edge technique, U M_4 edge HR-XANES provides more details with respect to the U redox states in the samples. The U M_4 edge HR-XANES spectra of the Um175 and Um175f samples and the U_4O_9 and Umh reference compounds are shown in Figures 4.2.5 a,b. The energy positions of the C, D and E peaks are very similar for the Um175 and Umh spectra. This is clear evidence that U(VI) dominates in the Um175 sample. The missing U(V) contribution detected by XPS for this sample can be attributed to the different penetration depths of these two techniques. XPS probes only the surface layer (~1 nm), whereas the U M_4 edge HR-XANES is a bulk sensitive method. The comparison of the two spectroscopy techniques suggests that U(V) in the Um175 sample is formed explicitly in surface layers.

The main peak C of the Um175f spectrum is shifted about 0.2 eV towards the characteristic for U(V) peak B of U_4O_9. This experimental evidence confirms substantial U(V) contribution in the Um175f sample. Since the intensities of peaks D and E significantly decrease but do not shift in energy, it is likely that the U(V) does not form U-*yl* type of bonding (Section 4.1). The U M_4 edge HR-XANES results agree with the results obtained from the XPS analyses.

Although a reducing E_h was observed (Table 4.2.1) after adding Fe(II) no evidence for U(IV) has been found. No apparent U(VI) reduction to U(IV) was as well reported by Latta *et al*. by analyzing U redox behavior in stoichiometric magnetite by conventional U L_3 edge XANES; U(VI) was found to be reduced to U(IV) only when $Fe(II)/Fe_{TOT}$ in the solid was higher than 0.42. [46] The results of the presented study can be explained by the low $[H^+]$ and low magnetite stoichiometry, which does not provide favorable conditions for U(VI) reduction to U(IV). This assumption is supported by thermodynamic considerations. According to the *Pourbaix* diagram U(IV) formation is also not to be expected (Figure 4.2.3).

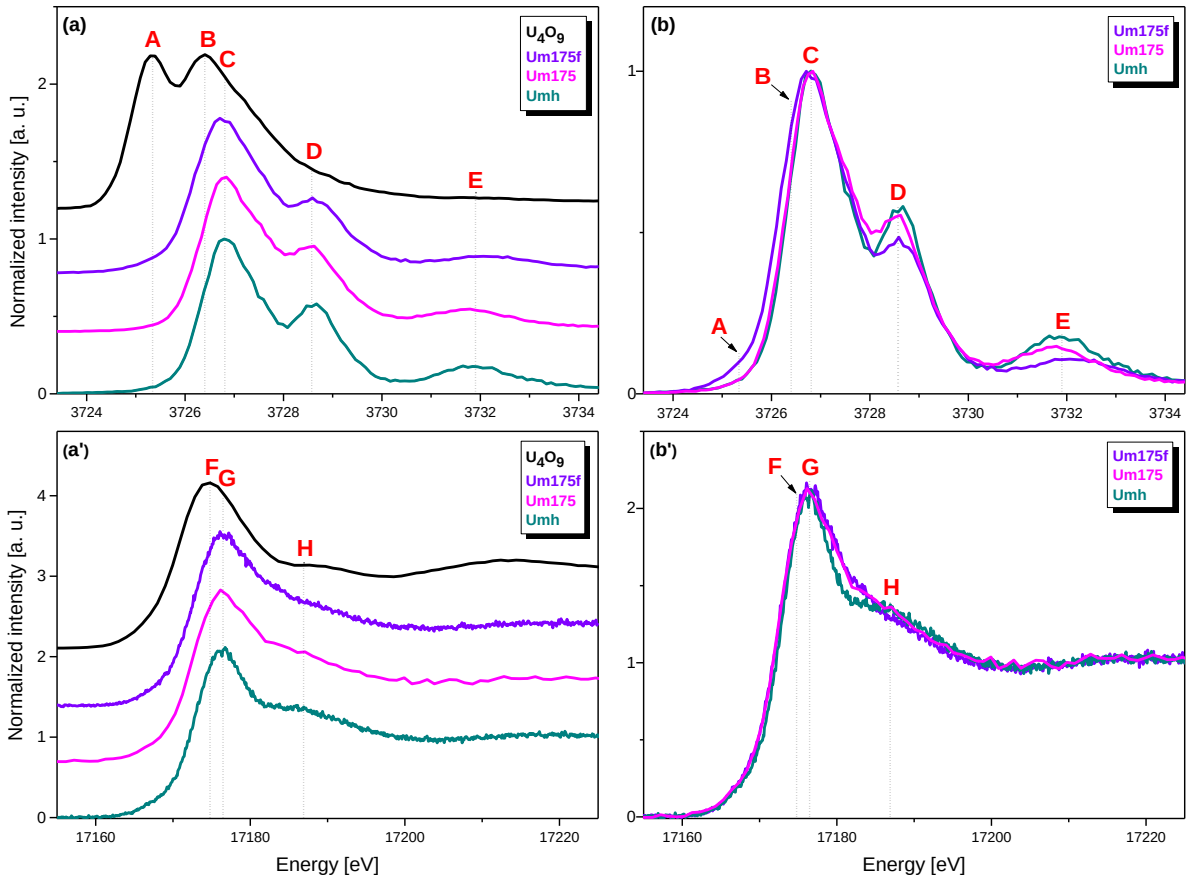

Figure 4.2.5. U M_4 (a, b) and U L_3 (a', b') edge HR-XANES spectra of U_4O_9 (black), Um175f (violet), Um175 (magenta) and Umh (marine-blue).

Table 4.2.2. Energy positions of the spectral peaks.

Edge	U M_4 (± 0.05 eV)				
Peak	A	B	C	D	E
[eV]	3725.4	3726.4	3726.8	3728.6	3731.9
Edge	U L_3 (± 0.05 eV)				
Peak	F	G	H		
[eV]	17174.8	17176.5	17186.8		

4.2.3. Conclusion

Under the given conditions of the present experiments magnetite reduces U(VI) to U(V) after long interaction (175 days). The addition of Fe(II) leads to an increasing U(V) content and may induce partial recrystallization of the magnetite leading to incorporation of U(V) in its structure. These results help to understand previous contradictory reports discussing identification of U(V) in magnetite reacted with U(VI). The U reduction kinetics strongly depend on the E_h/pH conditions, the stoichiometry of magnetite and the U concentration etc. The here presented investigations demonstrate that the U M_4 edge HR-XANES technique is very suitable for *in-situ* short and long-term studies aiming mechanistic understanding of the influence of these factors on the U redox behavior and kinetics. To avoid the oxidizing effect from intruded air during the long-term experiments further studies need to be performed with suitable sample cells, which are able to strictly control redox conditions. XPS apparently provides information predominantly from the sample surface, while the XAS signal is averaged over the bulk. One has to note that sample preparation and the need to transfer the sample to the XPS instrument may cause artifacts in measurements. Investigations of systems with environmentally relevant U concentrations lower than those investigated here will be possible at the CAT-ACT-Beamline, ANKA, which is expected to provide two orders of magnitude higher photon-flux compared to the INE-Beamline.

5. HR-XANES and RIXS investigations of U and Pu systems

Detailed speciation analyses of mixtures of *An* in different oxidation states using spectroscopy methods require spectra of suitable reference samples. Of fundamental interest is also to obtain information about the electronic structure of the *An* and their compounds by probing directly their unoccupied valence states using advanced HR-XANES and RIXS methods. [35, 55] The potential of these techniques has not yet been completely revealed and exhausted as up to date only a very few investigations of *An* systems are present in the literature. [35, 37, 50, 55] The intermediate oxidation states of the *An* are often unstable under ambient conditions therefore it is obligatory to develop and build suitable cells for synchrotron based experiments under controlled conditions, e.g. absence of O_2 etc. It is desirable to carefully monitor the changes of the *An* oxidation states before and after the experiments using alternative methods. An advanced approach is to perform the *An* oxidation states investigations directly at the experimental station at the Beamline and to probe *in-situ* the changes in the electronic and geometric structures of the *An* species. Such an *in-situ* cell can maintain well controlled reaction conditions, i.e. redox potential but can also comprise a combination of spectroscopy methods simultaneously applied on the sample.

This section presents results from the investigations of three different U and Pu systems. In the first part for the first time U(VI) and U(V) carbonate complexes in aqueous media are investigated using an *in-situ* spectroelectrochemical cell by U M_4 edge HR-XANES and RIXS techniques coupled with *in-situ* UV-Vis spectroscopy. The main part of this work includes the development, building and tests of the *in-situ* cell coupling spectroscopy with electrochemistry applied for these experiments.

5. HR-XANES and RIXS investigations of U and Pu systems

U is known to form several oxy-(hydr)oxide species with quite close compositions but different structures. XPS U 4*f* spectra of UO_3 polymorphs compared to a synthetic $UO_3 \cdot 1\text{-}2H_2O$ do not show any differences (within the analytical uncertainty) therefore they do not provide information about variations in the U electronic structure of these compounds. [27] In the second part a series of (α,β,γ)-UO_3 polymorphs and the synthetic U(VI)-*yl* compound meta-schoepite, widely used as a U(VI) reference in XAS studies, are for the first time investigated by the U M_4 edge HR-XANES method. A fingerprint approach is proposed and applied to compare the level of covalency of the U-*yl* bonds in the UO_3 polymorphs. The experimental results are supported by quantum chemical calculations with the FEFF code and thermodynamic considerations.

In the third part the electrochemically prepared Pu oxidation states Pu(III)-Pu(IV)-Pu(V)-Pu(VI) in perchlorate aqueous media and colloidal Pu(IV) are investigated by using Pu L_3 and M_5 edge HR-XANES techniques. Some of the experimental results are supported by quantum chemical calculations. The key part of this work is the development and tests of a set of cells for redox sensitive Pu sample aqueous solutions.

For the first time a set of liquid cells and an *in-situ* cell for experiments fulfilling the technical and safety requirements of the U/Pu $M_{4,5}$ edge HR-XANES/RIXS experiments have been built and successfully applied as a major part of this Doctoral Project.

5.1. *In-situ* spectroscopy of the electrochemical reduction of U(VI) to U(V) in carbonate complexes

5.1.1. Introduction

It has been shown that U-*yl* carbonates are one of the main species formed under aerobic conditions after a few years of SNF storage. [93] U-*yl* carbonate complexes are the most relevant species found in groundwater as well as in sea and ocean waters. [94] From all identified minerals, U-*yl* carbonates are the only mineral group where U(V) is known to be stabilized in the crystal structure. [95] Not much is known about the chemical and physical properties of $[U^{V}O_2]^{+}$ due to its thermodynamic instability. Several studies exist including laboratory synthesized U(V) in inorganic and organic compounds. [77, 90, 96] A very recent EXAFS study was reported for a U(V) carbonate complex formed during a ferrihydrite transformation to goethite catalyzed by Fe(II). [17] A few available studies utilizing U $L_{1,3}$ edge XAFS based methods are reported for electrochemically prepared U(V) tricarbonato complexes. [97, 98] Other methods used for investigations of these complexes include UV-Vis, Raman, NMR, powder XRD techniques as well as theoretical calculations. [99-106]

One of the main challenges in studying U(V) compounds is their high chemical instability leading to disproportionation reactions, which demands well controlled conditions (i.e. an inert atmosphere) during the experiments. One of the best approaches is to maintain the redox potential of U(V) by an electrochemical setup. U(VI)-U(V) electrochemistry in carbonate media is an established method with well-defined stability conditions for U(V) species: It is often combined with UV-Vis spectroscopy for characterization of the U oxidation states. [97, 107]

5.1. *In-situ* spectroscopy of the electrochemical reduction of U(VI) to U(V) in carbonate complexes

The synchrotron based X-ray methods provide the opportunity to combine two different spectroscopy tools; UV-Vis spectroscopy gives information mainly about molecular speciation, X-ray based methods are used to study materials on the atomic level (Figure 5.1.1). The application of in-situ based electrochemistry eliminates the artefacts resulting from alteration of the samples during their storage and transportation prior the spectroscopic measurements.

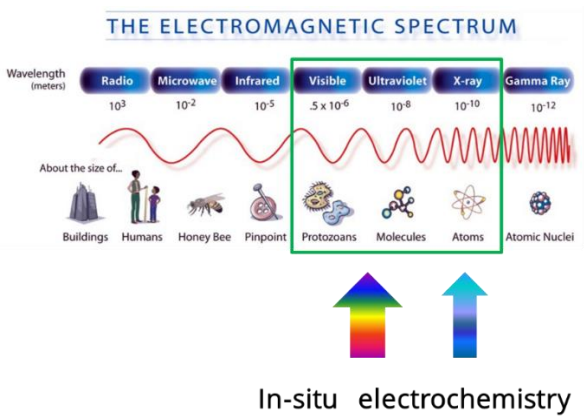

Figure 5.1.1. The entire electromagnetic spectrum and used in-situ techniques used for molecular and atomic characterization of U species. (source www.ck12.org)

The main aims of this work include:

1) Development and building of a compact *in-situ* spectroelectrochemical cell for studying the reduction of U(VI) to U(V) with the potential to be applied for other redox states and other *An*. The cell can uniquely combine electrochemistry with UV-Vis and HR-XANES/RIXS investigations;
2) Adoption of the cell for operation in the temporary controlled area of the INE-Beamline. The cell fulfils all technical and safety requirements for investigations of radiotoxic samples at the INE-Beamline;
3) Application of the *in-situ* cell to study the change of the U 5*f* unoccupied valence states upon reduction of U(VI) to U(V) free from experimental artefacts by the U M_4 edge HR-XANES and 3*d*4*f* RIXS techniques. Generation of U(VI) and U(V) reference samples for speciation investigations of U.

5.1.2. Materials and Methods

5.1.2.1. Preparation of U stock solution

The stock solution of $Na_4[U^{VI}O_2(CO_3)_3]$ was prepared by dissolving freshly precipitated $UO_3 \cdot 1\text{-}2H_2O$ in 1.5 M Na_2CO_3 with continuous shaking of the mixture for several hours. The resulting yellow colour solution was filtered through 40 µm Millipore filter and the pH was adjusted to 11.8 with 0.5 M NaOH. The resulting solution was then analyzed for total U concentration ([U]). A 0.035 M U solution was used for bulk electrochemistry experiments, whereas a diluted 0.020 M U solution was studied by cyclic voltammetry (CV) measurements. Both solutions have been purged with Ar gas at least for 8 hours before using them for the electrochemical reactions. All procedures were carried out in an Ar glovebox (1-2 ppm O_2, < 1 ppm CO_2) at the INE laboratories.

5.1.2.2. Electrochemical procedures

5.1.2.2.1. Cyclic voltammetry

CV measurements were performed using a VoltaLab 21/PGP20 potentiostat using the 0.02 M U aqueous solution and 0.5 mm Ø Pt wires as working and counter electrodes and two different types of reference electrodes: Ag/AgCl [E_0=195 mV] electrode with a Vycor glass frit and a Hg/HgO [E_0=127 mV] electrode with ceramic frit designed for alkaline (1.5 M Na_2CO_3, pH=11.8) solution (both from ALS Co., Ltd).

CV consists of cycling the potential (E) of an electrode, which is immersed in a solution, and measuring the resulting current (*i*). The potential of this working electrode is controlled versus a reference electrode (Hg/HgO was finally used for CV and bulk electrochemistry). The controlling potential, which is applied across these two electrodes, can be considered as an excitation signal. This excitation signal sweeps E of the electrode between two values. The CV is a graphical representation of *i* (*y*-axis) versus E (*x*-axis). Because E varies linearly with time, the *x*-axis can also be thought of as a time axis. The CV is performed for the qualitative analysis of the redox reactions taking place at the electrodes in a homogeneous chemical system. [108] The CV scan rate can be different and varies between 10 mV/s and 100 mV/s depending on the performance of the used potentiostat. In this case, only a single scan rate of 10 mV/s is available. More advanced instrumentation enables switching E and variable scanning rates (from 0 mV to -870 mV) applied to determine more precisely the reducing and oxidizing potentials in the system under study. A CV is obtained by measuring *i* at the working electrode during the potential scan. [108] *i* can he considered as the response signal to the potential excitation signal.

5.1.2.2.2. Bulk electrolysis

For bulk electrolysis a Pt-mesh (80 µm, 25×35 mm) was used as a working electrode, Pt-spiral (0.5 mm Ø, 23 cm length) as a counter electrode and Hg/HgO as a reference electrode (all from ALS Co., Ltd). A 0.035 M U stock solution was added to the compact *in-situ* spectroelectrochemical cell developed and built within this doctoral project. The counter electrode was positioned inside a borosilicate tube with a glass frit at the bottom (16-40 µm pore size) to prevent the contact of the electrolyte formed at the working electrode with the oxidizing agents, e.g. the oxygen (O_2) continuously evolving at the counter electrode (Equation 1).

$$4OH^- \rightarrow O_2\uparrow + 2H_2O + 4e^- \qquad (1)$$

O_2 was evacuated through the polypropylene tube (0.2 mm Ø) connected at the higher part of the glass tube electrode compartment to a cover of the first containment vessel. A basic schematic principle of the electrochemical cell operation is shown in Figure 5.1.2.

The 1 mm space between the two containments of the cell was flushed with He to remove the evolving O_2 and the aerosol, i.e. products of the electrochemical reaction. Both were collected by an aerosol particle filter (DIN-30X, Topas Gmbh) installed at the opposite site of the outer He flushing adapter (6 mm Ø**,** Festo AG). The negative potential of -775 mV, determined from the CV measurements, was applied to reduce U(VI) to U(V) (Equation 2)

$$[U^{VI}O_2(CO_3)_3]^{4-} + e^- \rightarrow [U^{V}O_2(CO_3)_3]^{5-} \qquad (2)$$

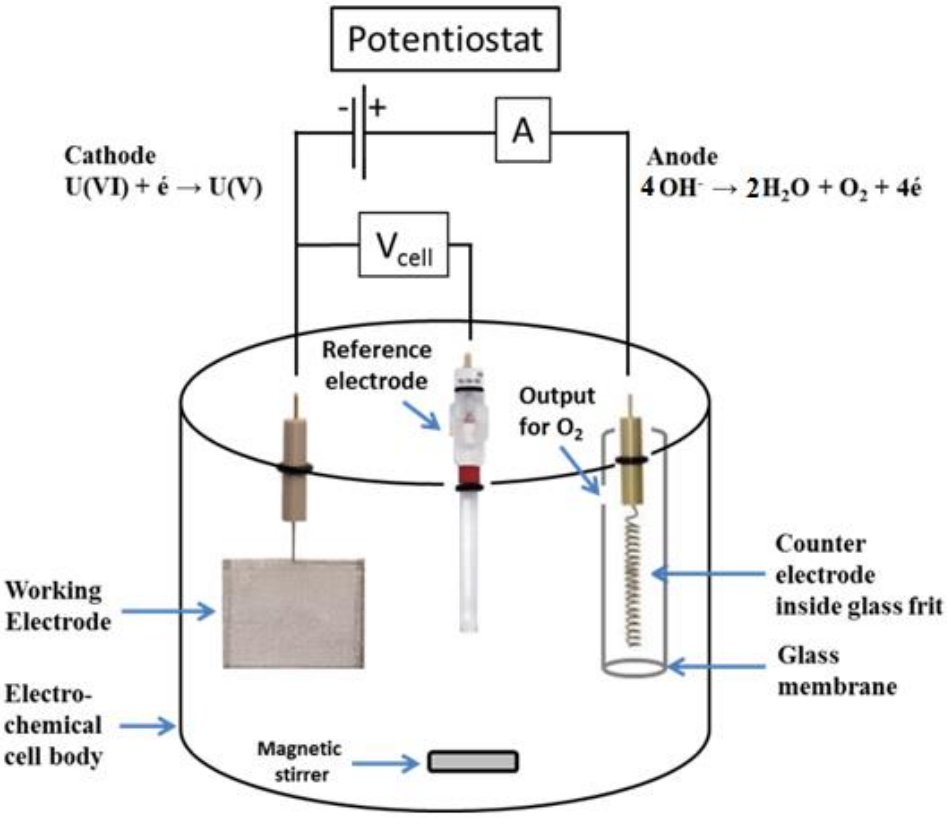

Figure 5.1.2. Basic principle of three-electrode bulk electrochemical cell setup and operation.

5.1.2.3. *In-situ* UV-Vis spectroscopy

UV-Vis spectra were continuously recorded in the range 360-520 nm in transmission mode during the *in-situ* electrochemical process using compact USB4000 UV-Vis spectrometer, D-2000 Deuterium lamp as a UV light source and a UV-Vis bifurcated optical fibers (all OceanOptics Gmbh) with a cord diameter of 400 µm. 100 spectra with 100 nm acquisition time were recorded and averaged to obtain the individual spectra presented in Figure 5.1.7. SpectraSuit Software (OceanOptics Gmbh) was used for analyses of the spectra.

5.1.2.4. U M_4 edge HR-XANES/RIXS spectroscopy

U M_4 edge HR-XANES and RIXS maps were measured using the X-ray emission spectrometer at the INE-Beamline (ANKA) as described in Section 3.2. Five spectra were recorded and averaged for each of the two U(VI) and U(V) species recorded before and after electrolysis, respectively. The spectral energy range was from 3722 eV to 3750 eV with a 0.1 eV step size. 3*d*4*f* RIXS maps were measured for emission energies from 3327 eV to 3338 eV with 0.33 eV step size and incident energies from 3720 to 3740 eV with 0.2 eV step size. To improve the spectral resolution an aluminum pinhole with a diameter of ~1 mm aperture was installed in front of the *in-situ* spectroelectrochemical cell at about 50 mm distance. To increase the signal to noise ratio all measurements were carried out inside a He glovebox installed around the spectrometer and the cell (O_2 < 1000 ppm).

5.1.2.5. Spectral area fitting

The areas of the different peaks of the U M_4 edge HR-XANES spectra for $[U^{VI}O_2(CO_3)_3]^{4-}$ and $[U^{V}O_2(CO_3)_3]^{5-}$ are estimated by fitting the spectra with PseudoVoigt type profiles [47, 50] obtained by convoluting a Gaussian with a Lorenzian type profile using the Fityk program. [109] The spectra were normalized to the intensity of the post-edge region equal to 1. First, an arctangent function with a fixed step 0.5 and energy position 3737.2 eV describing the post-edge jump was used. Second, the peaks A and C were fitted with two PseudoVoigt profiles, whereas the peak B was modelled with one Gaussian profile (Figure 5.1.10; Table 5.1.1).

5.1.3. Results and Discussion

5.1.3.1. *In-situ* spectroelectrochemical cell

A 3*D* design of the *in-situ* spectroelectrochemical cell developed, built and applied within this doctoral project is presented in Figure 5.1.3.

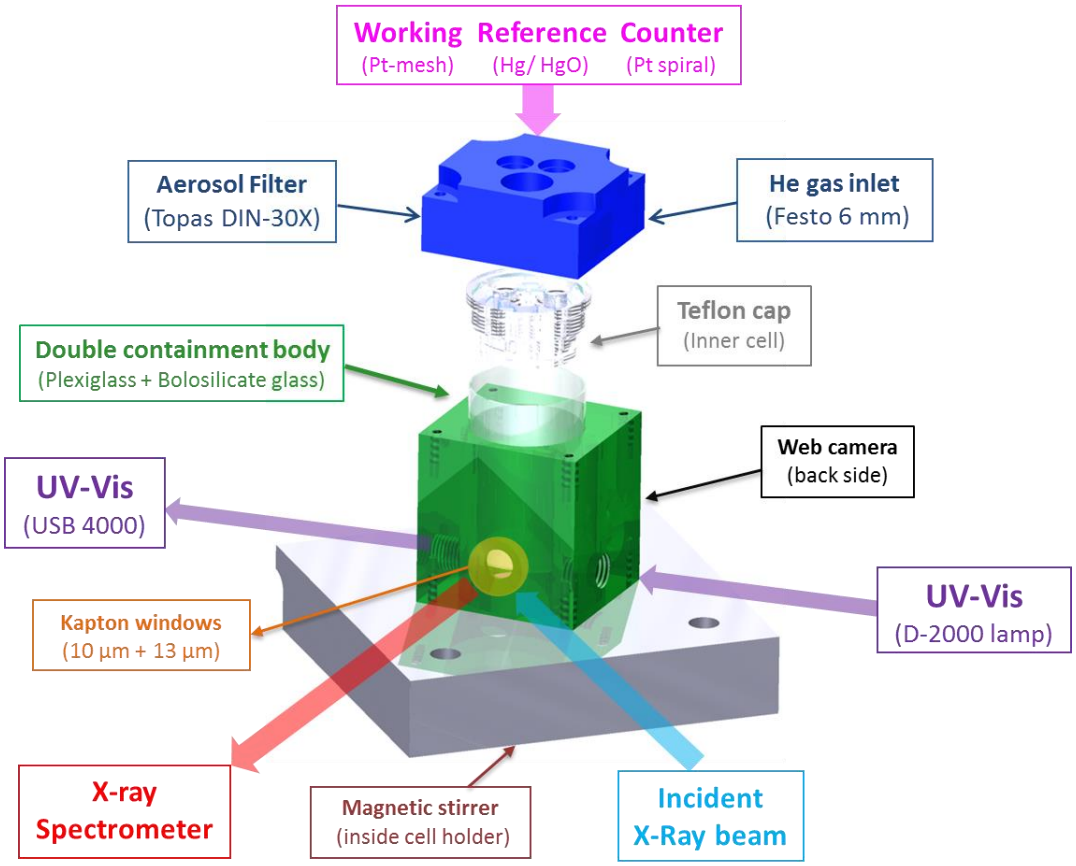

Figure 5.1.3. 3*D* model of the *in-situ* spectroelectrochemical cell comprising: three electrodes; an inlet and an outlet for the He gas flow; a filter for aerosol particles, cell body with an implemented double containment; a window for a web camera; UV-Vis light source attached to the cell; UV-Vis spectrometer connected to the cell via an optical fiber; magnetic stirrer implemented on the bottom of the cell; windows for incident X-ray beam and emitted X-ray fluorescence; double containment with exchangeable Kapton windows (10-100 µm) which can be used for different measurements.

5.1. *In-situ* spectroscopy of the electrochemical reduction of U(VI) to U(V) in carbonate complexes

The design development, building and tests of the final cell have been carried out during eight months; two prototype cells have been assessed within this time. An advantage of the cell compared with those previously reported is the implemented UV-Vis setup, which allows simultaneous UV-Vis, electrochemistry and XAFS measurements at the beamline. In addition, this cell is designed for XAFS experiments at low photon energies 3000-4000 eV. Two Kapton windows with 10 and 13 µm thickness absorbing only a few percent of the photons (~15% at 3727 eV) but possessing long-term mechanical and chemical stability are implemented. A picture of the *in-situ* spectroelectrochemical cell during experiments at the INE-Beamline is shown in Figure 5.1.4.

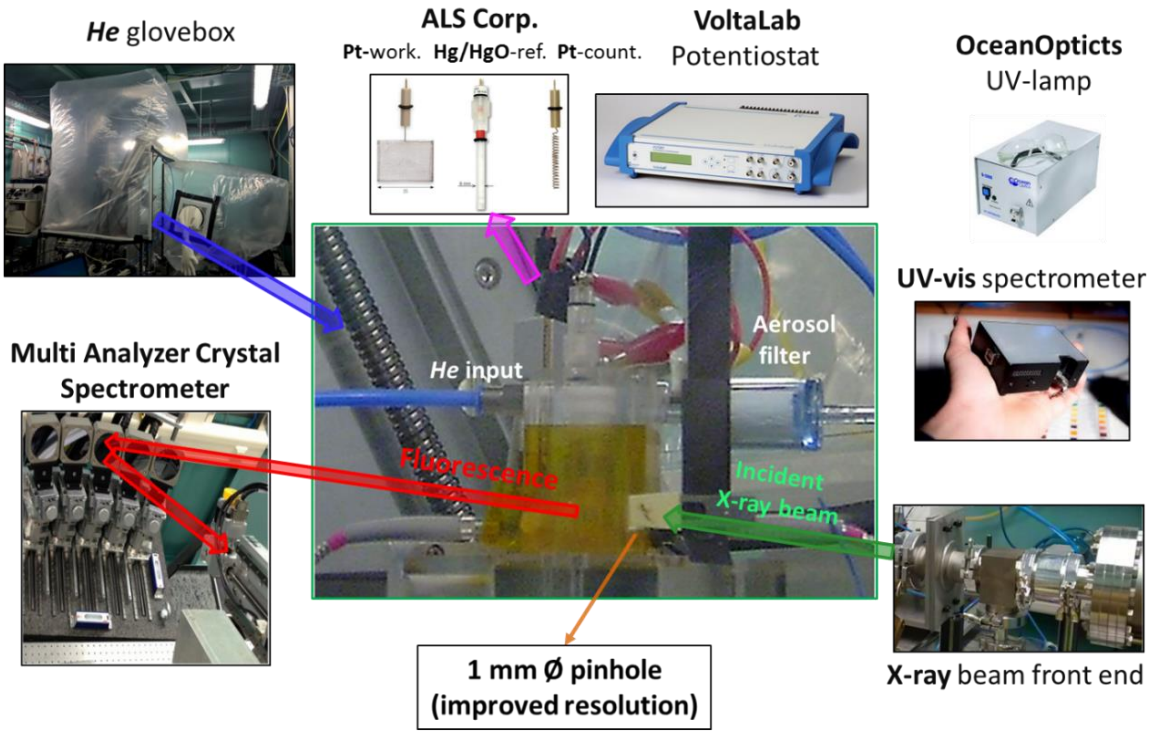

Figure 5.1.4. Picture of the *in-situ* spectroelectrochemical cell installed at the INE-Beamline inside the He glovebox. The MAC-Spectrometer and used instrumentation are shown too.

5.1. *In-situ* spectroscopy of the electrochemical reduction of U(VI) to U(V) in carbonate complexes

The size of the cell (15 cm in height and 10 cm in width) was designed to fit into the transfer chambers of the gloveboxes at the INE laboratories and the INE-Beamline. The necessary double containment of the cell was achieved by inner and outer parts made from borosilicate glass and Plexiglas, respectively. Windows with 6 mm Ø equipped with 10 µm (inner) and 13 µm (outer) Kapton films were introduced in the two containments. The connection of the main body and the cover of the assembled cell was glued with a 50 µm thick Kapton tape. The windows, the two UV-Vis fibers attached to the outer part of the cell and the end of the working Pt-mesh electrode were positioned at the same height. The magnetic module was attached on the bottom inside of the cell and fixed with a 1mm thick Al plate by four screws. The setup was stable during the experiment, which took place for more than 12 hours. No evaporation of the solution due to heating caused by the magnetic stirrer and the elevated temperature inside the He glovebox (42 °C) was noticed.

5.1.3.2. Cyclic voltammetry and chronoamperometry

Prior to the electrochemical experiments CV were recorded by scanning the E within the desired range to determine the reduction and oxidation potential of the system under study. [108] Using different scan rates allows the determination of more precise potentials. The only scan rate available for the used potentiostat of 10 mV/sec resulted in broad and flat cathodic and anodic peaks, P_c and P_a, respectively, separated (ΔE_p) by 190 mV (Figure 5.1.5). In the recent study of Ikeda *et al*. ΔE_p was estimated to vary between 250 and 400 mV, which depends mainly on the scan rate of the CV. [97]

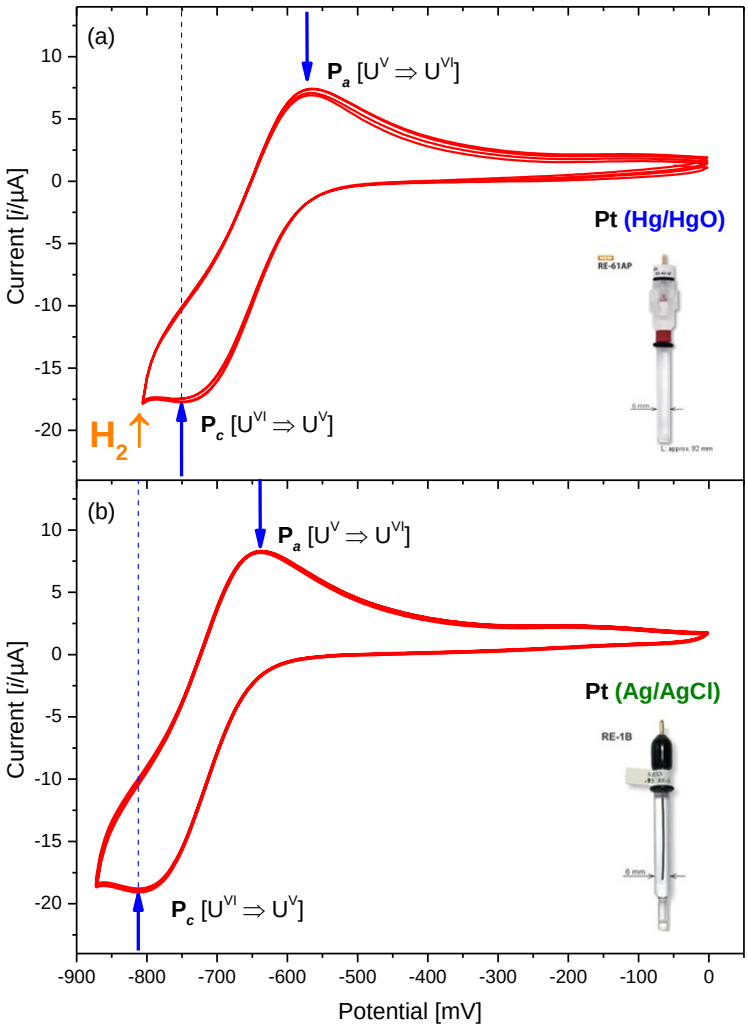

Figure 5.1.5. Cyclic voltamogramms of U tricarbonato complexes measured with scan rate of 10 mV/sec for Hg/HgO (a) and Ag/AgCl (b) reference electrodes.

P_c and P_a peaks are very broad at low scanning rates and become much sharper with a slight shift to lower potentials. [97] The first tests showed that U(VI) can be reduced to U(V) without forming any U(IV) precipitates or other artefacts. The reducing E determined for the Hg/HgO and Ag/AgCl reference electrodes differs by approximately 65 mV (Figure 5.1.5, blue lines), which is in agreement with their different E_0 values [Ag/AgCl, E_0=195 mV] and [Hg/HgO, E_0=127 mV]. Finally, a Hg/HgO electrode has been used for all experiments due to the much higher stability of the frit membrane compared to that of the Ag/AgCl electrode which quickly corroded at pH=11.8. To estimate the reduction kinetics of U(VI), preliminary tests were done in Ar glovebox in laboratory conditions. A nearly complete reduction of U(VI) to U(V) was recorded within ~2 hours (Figure 5.1.6). The reduction process proceeds very fast in the first 20 minutes resulting into ~50% reduction of U(VI). The reduction rate slows down considerably after 40 minutes of electrolysis due to a decreasing U(VI) concentration and related to this electron transfer rate, which is described by a square root dependency on the current density. [110]

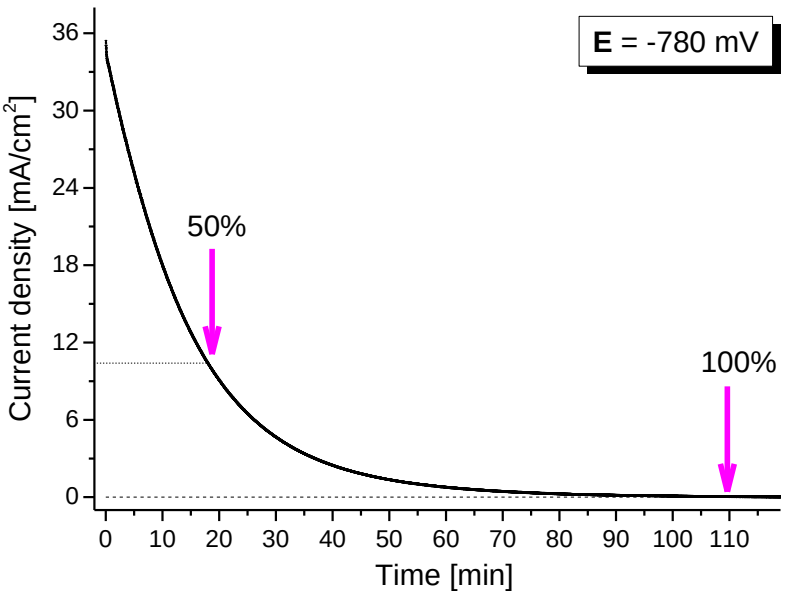

Figure 5.1.6. Decrease of the current density during U(VI) reduction to U(V) in 1.5 M Na_2CO_3 aqueous solution. Complete U(VI) reduction is achieved within 2 hours for the electrochemical setup used.

5.1.3.3. *In-situ* UV-Vis spectroscopy

The UV-Vis spectroscopic technique can be used for molecular speciation of U. It is sensitive to the coordination symmetry of the studied U complexes. [111] UV-Vis spectra were continuously recorded during the experiment. The clearly resolved eight bands of the U(VI)-*yl* fine structure are measured for the U(VI) tricarbonato complex (Figure 5.1.7) before starting the reaction and agree well with results from previous studies. [101] [97]

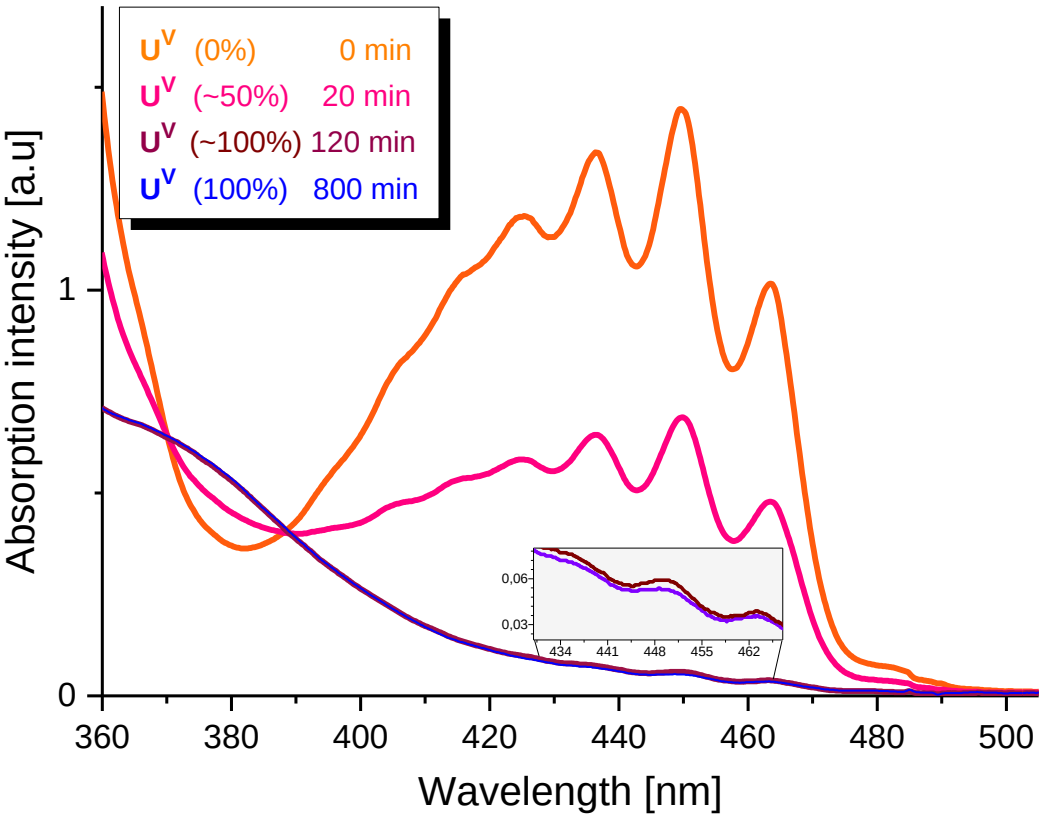

Figure 5.1.7. *In-situ* measured UV-Vis spectra: U(VI) (orange), 50% reduced U(VI) (magenta), 100% reduced U(VI) to U(V) (brown and violet). The time passed after the beginning of the electrochemical reaction is indicated. Photographs of the U(VI) and U(V) tricarbonato complexes in aqueous carbonate media as prepared under laboratory conditions (top-right).

During the U(VI) reduction to U(V) the intensity of the absorption bands decreases (Figure 5.1.7, magenta curve). U(V) has no bands in the monitored region (Figure 5.1.7, brown curve); The broad band characteristic for U(V) is in the Vis-NIR region, which is not measured in this study due to the limited spectral range of the spectrometer. [112]

U(V) was stable for more than 12 hours while the redox potential was kept constant (Figure 5.1.7, brown and violet curves).

The orange curve in Figure 5.1.5 represents the UV-Vis absorption spectrum of the U(VI) ion in 1.5 M Na_2CO_3. The absorption spectrum is characterized by a very weak and broad absorption in the visible range between 380 nm and 490 nm with a characteristic fine structure as well as an intense absorption in the UV range that extends nearly continuous to lower wavelengths. The intense absorption in the UV range (not shown) has no structure and does not offer characteristic features for spectroscopic speciation. [111] The fine structure of the low-energy absorption band is due to coupling of electronic transitions with the symmetric stretching vibration of the U(VI)-*yl* entity. [113] [114, 115] The absorption spectrum of U(VI) exhibits a band with significantly lower intensity in the visible range compared to that in the UV range (not shown here). The reason for this significant decrease has been discussed for a long time in terms of highest occupied molecular orbital (HOMO) and lower unoccupied molecular orbital (LUMO). [116, 117] Only detailed studies on $Cs_2(UO_2)Cl_4$ single crystals unambiguously showed a symmetry forbidden nature of the HOMO-LUMO transitions and explained the nature of the absorption bands. [37, 114, 118]

5.1.3.4. U M_4 edge HR-XANES/RIXS

The 3*d*4*f* RIXS map of U(VI) exhibits three resolved main regions (indicated by green, yellow and magenta arrows) (Figure 5.1.8 a). In the U(V) RIXS map one region appears as a very broad asymmetric structure with two distinguishable shoulders (see the arrows in Figure 5.1.8); The 3*d*4*f* RIXS data is useful to obtain information about the U electronic structure, i.e. the U 5*f* states which are largely responsible for the unique properties of the U compounds. [35] The HR-XANES spectrum corresponds to a cut parallel to *x*-axis through this plane at the maximum of the emission line resulting in a significantly reduced spectral broadening (white arrow). [47, 53] The U M_4 edge HR-XANES spectra of the U(VI) and U(V) tricarbonato complexes are depicted in Figure 5.1.9 (a, b).

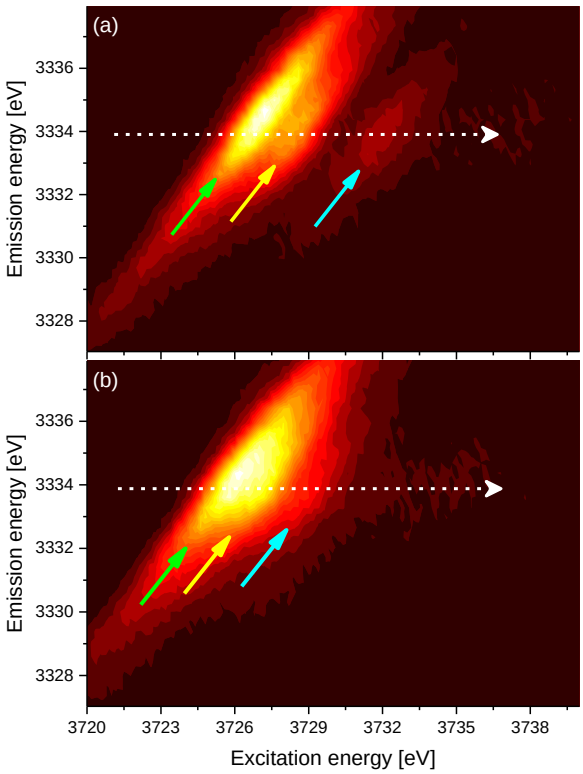

Figure 5.1.8. 3*d*4*f* RIXS maps of $[U^{VI}O_2(CO_3)_3]^{4-}$ (a) and $[U^{V}O_2(CO_3)_3]^{5-}$ (b).

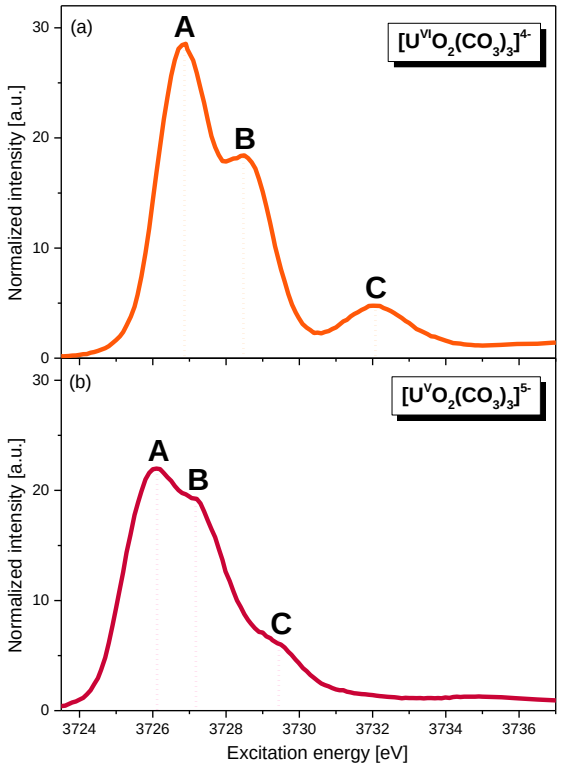

Figure 5.1.9. U M_4 edge HR-XANES spectra of $[U^{VI}O_2(CO_3)_3]^{4-}$ (a) and $[U^{V}O_2(CO_3)_3]^{5-}$ (b).

The U M_4 edge HR-XANES spectrum of U(VI) (Figure 5.1.9 a) exhibits an intense main peak (A) at 3726.9 eV with two well resolved higher energy features (B and C) at 3728.5 eV and 3732.0 eV (Table 5.1.1) characteristic for the U(VI)-*yl* structure. [35, 37, 51]. These peaks have been assigned to transitions of $3d_{3/2}$ electrons to $5f\delta/5f\varphi$ (A), $5f\pi$ (B) and $5f\sigma$ (C) unoccupied valence orbitals of U(VI) in the U(VI)-*yl* entity. [37] This assignment is valid also for the U(V) compound as found by DFT calculations. [97] In the U(V) spectrum, the main peak A, exhibits significantly less intensity and is shifted by ~0.8 eV to lower energies compared to that of U(VI). This energy shift is due to the better screening of the core-hole by the addition electron in the U(V) compound. The decrease in absorption intensity is a consequence of the less available unoccupied 5*f* states in U(V) ($[Rn]5f^1$) compared to the empty 5*f* shell in U(VI) ($[Rn]5f^0$). The energy positions of the peaks B and C shift significantly to lower energies and become closer to the main peak A (U(VI): A-B=1.6 eV, U(V), A-C=5.1 eV; U(V): A-B=1.0 eV, A-C=3.4 eV). Clearly, the U M_4 edge HR-XANES method provides quantitative information about the change in energy distances between the 5*f* based orbitals due to addition of an electron. This electron was previously found in the $5f\delta$ orbital of U(V) and leads to pronounced reduction of the area of peak A. [97] Since the measurements are performed *in-situ*, any experimental artefact can be neglected. As a result, it can be postulated that one additional electron leads to ~41% decrease of the area of the first peak and ~20% of the area of the whole U M_4 edge HR-XANES spectrum of $[U^{V}O_2(CO_3)_3]^{5-}$ compared to that of $[U^{VI}O_2(CO_3)_3]^{4-}$ (Table 5.1.1). This might be due to a reduced level of hybridization of 5*f* with *p* orbitals for the U(V) compound. The $5f\delta$ and the $5f\varphi$ orbitals are non-bonding orbitals therefore the area of this peak A should not be influenced by changes of mixing of metal 5*f* with ligand *p* orbitals. The height of a peak is proportional to the absorption cross section, whereas the area of the peak to the oscillatory strength for the transitions to atomic and molecular orbitals of U. [119]

Currently performed quantum chemical calculations will allow to compare experimental with theoretical results and to verify the obtained results. U M_4 edge HR-XANES has a substantial advantage over the conventional U $L_{1,3}$ edge XANES. Due to larger core-hole broadening effects influencing the U $L_{1,3}$ edge XANES spectra the energy shift between U(V) and U(VI) is rather small and the main absorption peak is dominated by a broad featureless structure. [97]

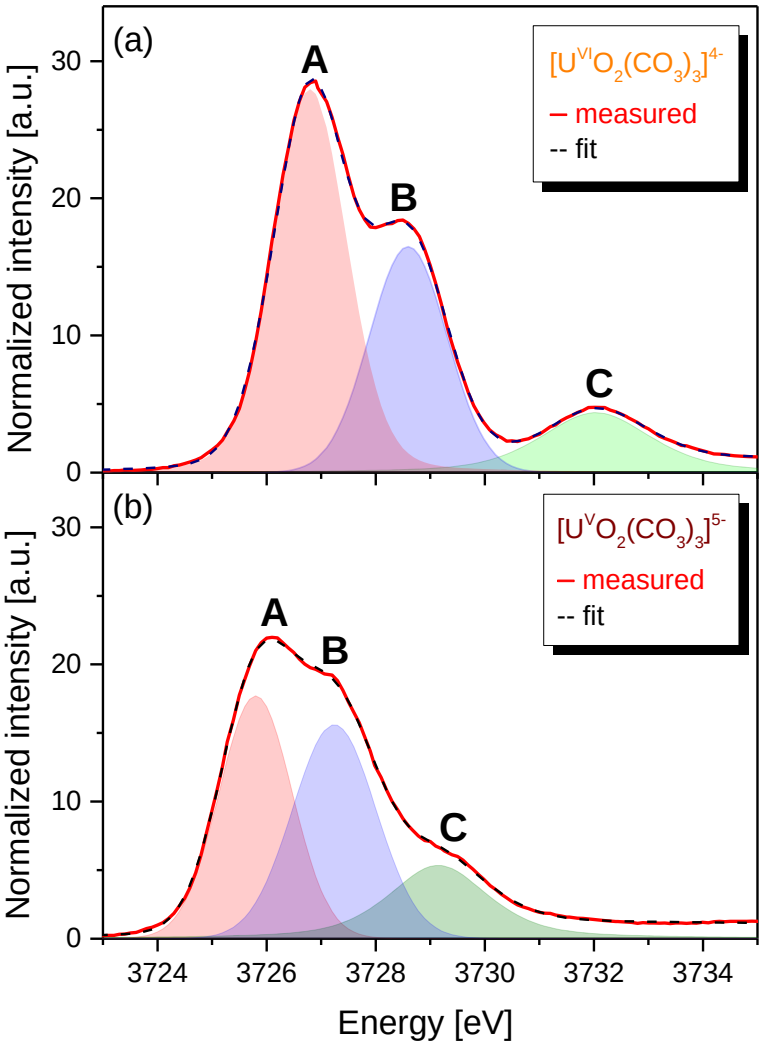

Figure 5.1.10. Measured (red) and best model (black dotted) spectra of the normalized U M_4 edge HR-XANES spectra of $[U^{VI}O_2(CO_3)_3]^{4-}$ (a) and $[U^{V}O_2(CO_3)_3]^{5-}$ (b).

Table 5.1.1. Energy positions and areas of the peaks for the U M_4 edge HR-XANES spectra of $[U^{VI}O_2(CO_3)_3]^{4-}$ and $[U^{V}O_2(CO_3)_3]^{5-}$; (Peak positions: OriginPro 9.1 program is used; error bars: ± 0.05 eV; areas: Fityk 0.9.8 program; error bars: ± 0.5 a.u.)

		Energy position			
Specie	A, [eV]	B, [eV]	C, [eV]	B-A, [eV]	C-A, [eV]
$[U^{VI}O_2(CO_3)_3]^{4-}$	3726.9	3728.5	3732.0	1.6	5.1
$[U^{V}O_2(CO_3)_3]^{5-}$	3726.1	3727.1	3729.5	1.0	3.4
		Peak area			
Specie	A, [a.u.]	B, [a.u.]	C, [a.u.]		
$[U^{VI}O_2(CO_3)_3]^{4-}$	51.0	29.4	13.5		
$[U^{V}O_2(CO_3)_3]^{5-}$	29.9	29.7	15.2		

5.1.4. Conclusion

A novel spectroelectrochemical cell for *in-situ* electrochemistry, XAFS and UV-Vis experiments was designed, constructed and applied. A study of U(VI) reduction to the U(V) in the form of tricarbonato complex was performed for the first time using coupled *in-situ* UV-Vis and U M_4 edge HR-XANES/RIXS spectroscopies. Significant differences in electronic structures of these complexes is found. It is revealed that the main spectral peak A shifts by 0.8 eV to lower energies confirming the reduction of U(VI) to U(V), which is independently and simultaneously verified by the UV-Vis measurements. The energy distance between the A and the B peaks changes by -0.6 eV, and between the A and C peaks by -1.7 eV for the U(V) compared to the U(VI) compound. These clear spectral changes measured *in-situ* can be used in future speciation analyses for identification of U(V)-*yl* species. The here presented results are very valuable for verification and improvement of theoretical approaches for calculations of the electronic structure of U(V). Further analyses will elucidate if the differences obtained for the U M_4 edge HR-XANES spectra are comparable to transmission mode and conventional fluorescence mode measurements. It is still under discussion if the HR-XANES spectra are directly proportional to the absorption cross section.

5.2. Probing covalency in the UO_3 polymorphs by a fingerprint approach

5.2.1. Introduction

Both structural and electronic properties of the uranium oxides are of fundamental and practical interest primarily due to the role of UO_2 in the nuclear fuel cycle. [120, 121] UO_2 frequently is exposed to oxidizing conditions and other binary oxides like, for example, U_4O_9 and U_3O_8 form at different stages of the nuclear fuel cycle. [122] UO_3 has the highest oxygen content among the uranium oxides (except U-*yl* peroxides, $UO_4 \cdot xH_2O$). The chemical and physical properties of its polymorphs are also important to mining, milling, refinement and conversion processes that precede isotope enrichment within a nuclear fuel cycle. [123]

In this study it is demonstrated a finger print approach for detection of changes in the bond lengths between U and the two axial O atoms in uranyl type of bonding. It presents the results of theoretical *ab-initio* full-multiple-scattering (FMS) HR-XANES simulations for α-UO_3, β-UO_3 and γ-UO_3 phases by the FEFF 9.6 code. [62] Available thermodynamic data are used to explain the spectroscopic results. [3]

5.2.2. Materials and Methods

5.2.2.1. Sample preparations

The α-UO_3 and β-UO_3 phases were synthesized as reported in, [124] γ-UO_3 was a commercial (Cameco Corp.), UO_3·1-2H_2O was prepared as described. [125] CaU_2O_7 was synthesized by recrystallizing UO_3·1-2H_2O in concentrated $CaCl_2$ aqueous solution. Each compound with about 10 wt % of U was mixed with cellulose powder and pressed into a pellet.

5.2.2.2. Analysis methods

Samples were analyzed by synchrotron based XRD as described in Section 3.4. U M_4 edge HR-XANES spectra were measured at the INE-Beamline as described in Section 3.2. Four spectra were collected for each sample. The spectral energy range was from 3710 eV to 3780 eV with 0.1 eV step size. Thermodynamic data of Gibbs free energies of formation of U-O compounds were used from Neck *et al*. [20]

5.2.2.3. Quantum chemical calculations

The U M_4 edge HR-XANES spectra were calculated with the FEFF9.6 *ab-initio* quantum chemical code based on the full-multiple-scattering theory (FMS). The algorithm for the FMS method has been described elsewhere. [126] Phase shifts of the photoelectron were calculated in the framework of the self-consistent crystal muffin-tin (MT) potential scheme with 15% overlapping MT spheres. The spectra have been simulated using several types of exchange potentials: non-local, Dirac-Fock, Hedin-Lundquist or Dirac-Hara potentials. The best agreement with experiment has been achieved for the spectra calculated with the Hedin-Lundquist potential in Final State Rule (FSR) approximation for core-hole, reducing the $3d_{3/2}$ core-hole life-time broadening (3.5 eV) to 2 eV and correcting the Fermi energy for $UO_3 \cdot 1\text{-}2H_2O$ and CaU_2O_7 by 0.5 eV. The atomic potentials were calculated self consistently for cluster sizes of about 7.0 Å around the absorber (including 101 atoms), while FMS calculations of U M_4 edge HR-XANES were performed for cluster of 10 Å radii (285 atoms). For the simulations of the HR-XANES spectra, we have used the crystallographic data presented in Table 5.2.1. (Calculations were performed by Yulia Podkovyrina, South Federal University, Russia; FEFF input files for calculations are given in Appendix, Table AII.1)

Table 5.2.1. Crystallographic data used for calculations of the U M_4 edge HR-XANES spectra.

Phase	Space group	Crystal system	Atomic parameters	#ICSD
α-UO_3	P-3m1 (#164)	Trigonal	a=b=3.97 c=4.16 $\alpha=\beta=90°$ $\gamma=120°$	31628
β-UO_3	P121 1 (#4)	Monoclinic	a=3.91 b=14.33 c=10.34 $\alpha=\beta=\gamma=90°$	14314
γ-UO_3	I41/amd (#141)	Tetragonal	a=b=6.90 c=19.97 $\alpha=\beta=\gamma=90°$	1093
$UO_3 \cdot 1\text{-}2H_2O$	Pbcn (#60)	Orthorhombic	a=14.68 b=14.02 c=16.71 $\alpha=\beta=\gamma=90°$	156714
CaU_2O_7	R-3m (#166)	Trigonal	a=b=c=6.26 $\alpha=36.32$, $\beta=\gamma=90°$	31631

5.2.3. Results and Discussions

UO_3 polymorphs and $UO_3 \cdot 1\text{-}2H_2O$ can be synthesized by using uranyl nitrate hexa-hydrate as a starting material (Figure 5.2.1).

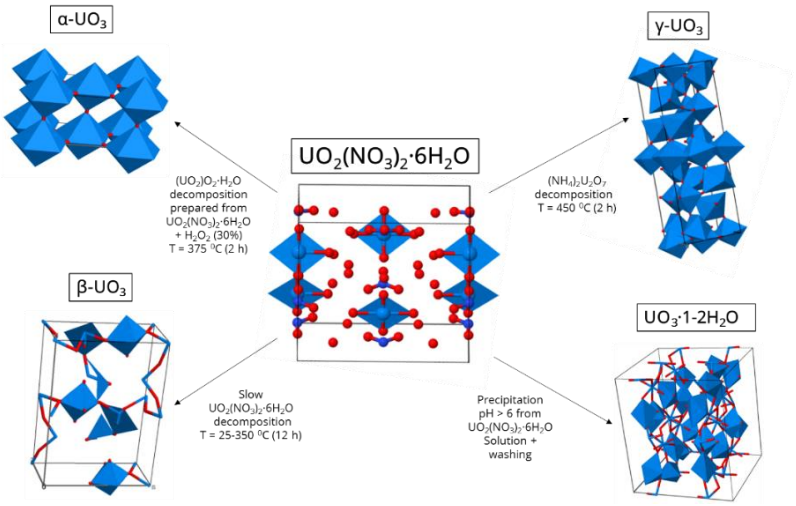

Figure 5.2.1. Description of formation routes of α-UO_3, β-UO_3, γ-UO_3 and $UO_3 \cdot 1\text{-}2H_2O$ synthesized from $UO_2(NO_3)_2 \cdot 6H_2O$.

The powder XRD patterns measured for the studied compounds correspond well with the spectra published in the ICSD database (Figure 5.2.2).

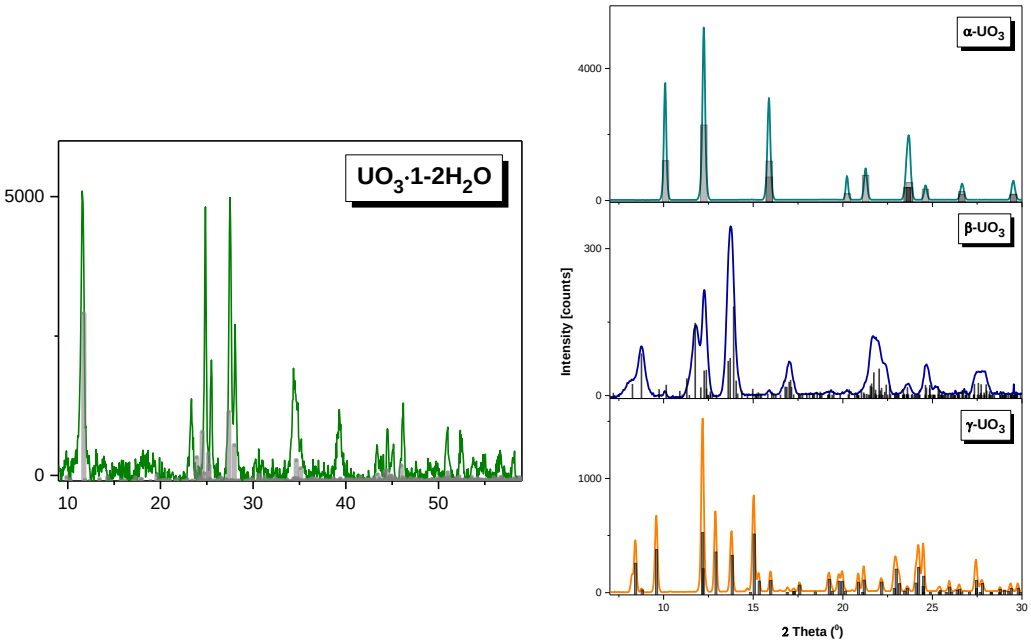

Figure 5.2.2. Powder XRD patterns of α-UO_3, β-UO_3, γ-UO_3 polymorphs (SUL-BL) and $UO_3 \cdot 1\text{-}2H_2O$ (Brucker Diffr.) together with XRD patterns published in the ICSD database (Table 5.2.1). XRD of CaU_2O_7 is not available.

5.2.3.1. U M_4 edge HR-XANES

The U M_4 edge HR-XANES spectra of the three UO_3 polymorphs are plotted along with the spectra of $UO_3 \cdot 1\text{-}2H_2O$ and CaU_2O_7 in Figure 5.2.3. All U M_4 edge HR-XANES spectra have three distinct spectral features marked with A (~3727 eV), B (~3729 eV) and C (~3732 eV) (Figure 5.2.3a). The nature of the peaks A, B and C is described in Section 5.1.

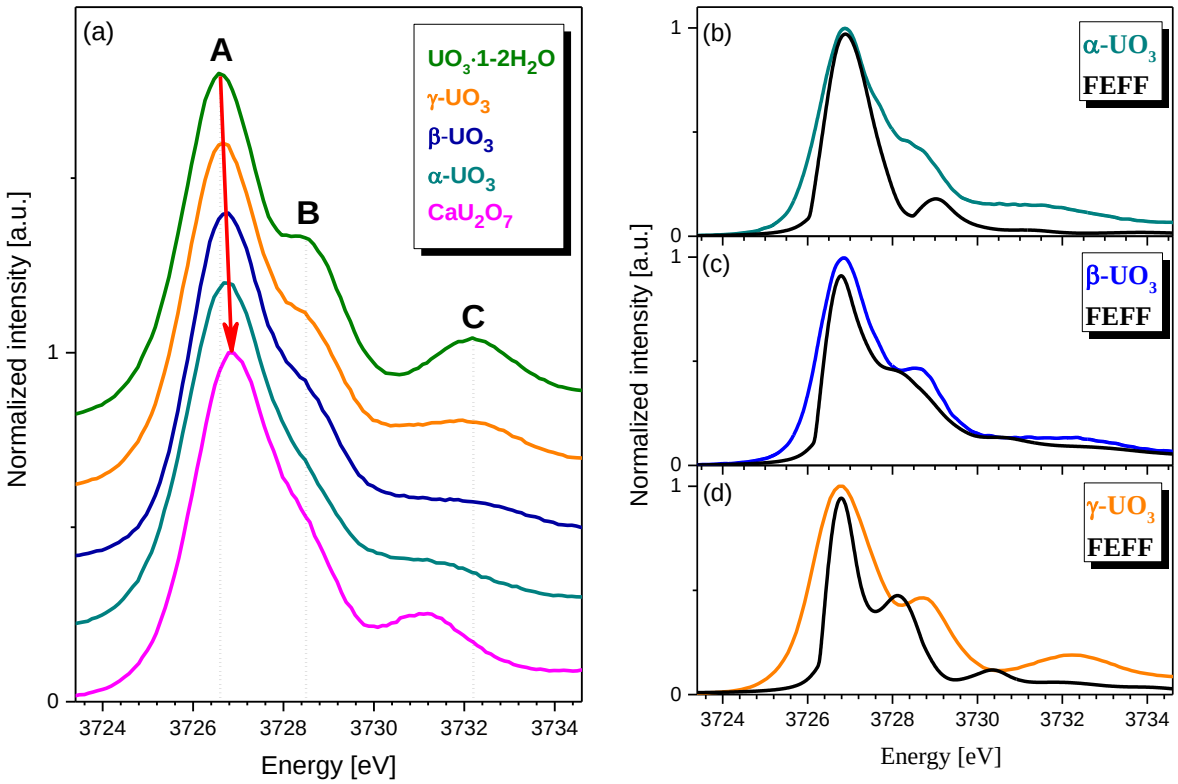

Figure 5.2.3. U M_4 edge HR-XANES spectra of $UO_3 \cdot 1\text{-}2H_2O$, γ-UO_3, β-UO_3, α-UO_3, and CaU_2O_7, (a), experimental and theoretical spectra for α-UO_3 (b), β-UO_3 (c) and γ-UO_3 (d) phases.

The hybridized U 5*f* and 6*p* orbitals form sigma covalent bonds mainly with 2*p* orbitals of the O_{axial} atoms therefore the energy position of peak C is essentially influenced by variations of the U-O_{axial} bond length. [35] U forms short 1.77 Å (U-*yl*) and longer, > 1.9 Å, (U-*ate*) U-O_{axial} bonds in $UO_3 \cdot 1\text{-}2H_2O$ (1.78 Å) and CaU_2O_7 (1.91 Å), respectively (Table 5.2.2). These differences in bond lengths are reflected by the energy positions of peaks A, B and C.

Peak A is shifted to higher energies (+0.3 eV), whereas peaks B (-0.2 eV) and particularly C (-1.1 eV) are shifted to lower energies for CaU_2O_7 compared to $UO_3 \cdot 1\text{-}2H_2O$. The elongation of the U-O_{axial} (0.13 Å) in CaU_2O_7 leads to less electronic density in the vicinity of U, i.e. decreased covalency of the U-O_{axial} bond; [114] as a result, due to worse screening of the core-hole, the main peak A is shifted to higher energies compared to this peak in the $UO_3 \cdot 1\text{-}2H_2O$ spectrum. Figure 5.2.3 also demonstrates that the intensities of the peaks B and C decrease within the $UO_3 \cdot 1\text{-}2H_2O$, γ-$UO_3$, β-$UO_3$ and α-UO_3 series (Figure 5.2.3 a). Herein it is assumed that these variations of intensities might be related to the covalency of the U-O_{axial} bond, i.e. higher covalency leads to higher intensity of these peaks. However, the peak C in CaU_2O_7 spectrum exhibits an intensity comparable to that in $UO_3 \cdot 1\text{-}2H_2O$, which indicates that the comparison of small changes in intensities of these peaks is only meaningful within a series of compounds with similar chemical compositions.

Table 5.2.2. Average U-O bond lengths for α-UO_3, β-UO_3, γ-UO_3, $UO_3 \cdot 1\text{-}2H_2O$ and CaU_2O_7.

Compound/value	U-O short, [Å]	U-O long, [Å]
α-UO_3	2.08	2.40
β-UO_3	1.70	2.25
γ-UO_3	1.83	2.27
$UO_3 \cdot 1\text{-}2H_2O$	1.78	2.36
CaU_2O_7	1.91	2.31

The energy position of peak B can be in principle influenced by variations of the U-O_{axial}, but also by changes in bonding distances between U and the equatorial ligands. Up to several different U sites with variable U-O_{axial} bond lengths are present in α-UO_3, β-UO_3 and γ-UO_3. α-UO_3 has two non-equivalent U positions; U forms bonds with the O_{axial} atoms with two different average bond lengths, i.e. U(1)-O_{axial1}=2.08 Å and U(2)-O_{axial2}=2.40 Å.

The U atoms in β-UO_3 can be divided into three groups: U(1) and U(2) have seven oxygen neighbours at distances varying between 1.69 Å and 2.72 Å, U(3) is coordinated by six oxygen atoms U(3)-O_{axial1}=1.79 Å, U(3)-O_{axial2}=2.17 Å, which form a deformed octahedron, U(4) and U(5) have six oxygen neighbours and form U-*yl* type of bonding. [127] In γ-UO_3 all U atoms are surrounded by six oxygen atoms in distorted octahedral environment; the average U-O_{axial} bond length is ~1.83 Å. [128] The energy positions of features A, B and C are related to the average U-O_{axial} distances for the three UO_3 compounds. The spectra of α-UO_3 and γ-UO_3 are similar to the spectra of CaU_2O_7 and UO_3·1-2H_2O, respectively. Therefore, in average the U-O_{axial} bonds with 1.83 Å bond length appear to have more covalent character in γ-UO_3 compared to α-UO_3, which has an average U-O_{axial} bond length of 2.08 Å (Table 5.2.2).

For each UO_3 phase, the theoretical spectrum is a sum of weighted spectra obtained by placing the absorbing U atom at each non-equivalent crystallographic site. The FEFF9.6 code reproduces all spectral features at the correct energy positions for α-UO_3 and β-UO_3 (Figure 5.2.3 b, c); some intensity differences are present. For γ-UO_3 the distances between features A and B (A-B), and B and C (B-C) are larger for the experimental (A-B ~ 2.0 eV, B-C ~ 3.5 eV) compared to the calculated (A-B ~ 1.7 eV, B-C ~ 2.2 eV) spectra (Figure 5.2.3 d).

5.2.3.2. Thermodynamic approach

Additional insights into the nature of the U-O bonds in the polymorphic phases of UO_3 can be derived by comparing standard molar Gibbs energies of formation $\Delta fG°_m$ of crystalline UO_3, UO_{2+x} phases and a U(VI)-*yl* type of compound. These compounds are systematically studied and thermodynamic parameters are summarized in several reviews and thermodynamic databases. [129-131]

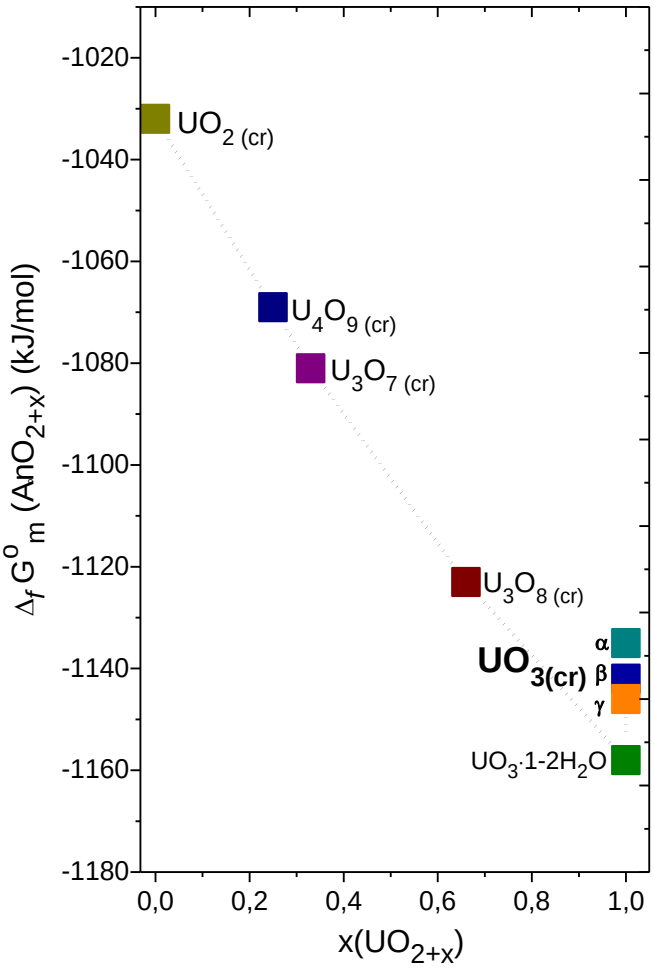

Figure 5.2.4. Standard molar Gibbs energies of formation of UO_{2+x} as a function of x. (Retrieved from [20])

$\Delta fG°_m$ of crystalline UO_{2+x} phases adopted from Guillaumont *et al.* [129] and Neck *et al.* [20] are plotted in Figure 6.2.4. As $\Delta fG°_m$ is the free energy released during the bond formation [132], the lower the energy, the stronger must be the U-O bond. According to this, the covalent character of the U-O bonds would increase in the order α-UO_3 (-1135 kJ/mol) < β-UO_3 (-1142 kJ/mol) < γ-UO_3 (-1146 kJ/mol) < $UO_3 \cdot 1\text{-}2H_2O$ (-1158 kJ/mol) as demonstrated in Figure 5.2.4. This result agrees well with the spectroscopy results, which clearly suggest an increasing weight of U-O short covalent bonds in the materials following the same trend.

5.2.4. Conclusion

It is demonstrated that a fingerprint approach using U M_4 edge HR-XANES can be effectively applied for the characterization of U-*yl* and U-*ate* type of U-O_{axial} bonding. Using this approach it is shown that U-O_{axial} bonds have likely more covalent character in γ-UO_3 compared to α-UO_3. The order of the increase in covalency in the materials is found to be the same from the spectroscopy and the thermodynamic results based on free Gibbs energies of formations (α-UO_3 < β-UO_3 < γ-UO_3 < UO_3·1-2H_2O). The U M_4 edge HR-XANES spectra of the UO_3 polymorphs are performed within the full-multiple-scattering (FMS) formalism. The input parameters are varied to obtain best agreement between theory and experiment. The FEFF9.6 code emerges as a useful tool for calculation of U M_4 edge HR-XANES spectra, as it successfully reproduced all spectral features for some of the studied compounds.

5.3. Study of the Pu oxidation states in perchloric acid

5.3.1. Introduction

Transuranium elements (Np, Pu, Am etc.) with various isotopic compositions generated in nuclear fuels during irradiation in a nuclear fission reactor represent long-term radiotoxic elements. Due to their ability to exist in different redox states, which greatly determines their chemical properties like for example solubility, the precise speciation analyses is of great importance for assessing and predicting their long-term radioecological behavior. This is relevant to Pu, which has been demonstrated to coexist in four (III, IV, V and VI) oxidation states in solution under environmentally relevant conditions. [19] The possibility for Pu to exist in higher oxidation states in a solid form of PuO_{2+x} was shown experimentally for a PuO_2 thin film, interacted with water [133] and later also confirmed theoretically. [134] The stabilization of Pu(V) in a thin PuO_2 films was questioned by Neck *et al*. and a $Pu(V)_{2x}Pu(IV)_{1-2x}O_{2+x}$(s,hyd) mixed compound was described as a result of thermodynamic calculations. [20]

The main goals of this section include:

1) Development, building and testing of a cell for investigations of Pu species in a liquid phase with the potential to be applied for other redox states and other *An*. The cell fulfils the technical and safety requirements for investigations of radioactive samples at the INE-Beamline and is optimized for experiments with X-ray beam with 3-4 keV energy;
2) Probing the Pu 5*f* and 6*d* unoccupied valence states of Pu(III), Pu(IV), Pu(V), and Pu(VI) by the Pu M_5 and L_3 edge HR-XANES as well as 3*d*4*f* RIXS. It is also aimed to provide Pu(III), Pu(IV), Pu(V), and Pu(VI) HR-XANES reference spectra for speciation investigations of Pu in laboratory and environmental studies. The Pu L_3 edge EXAFS technique is applied for characterization of the local atomic environment of Pu. The quantum chemical FEFF9.5 code is applied to complement and assist the interpretation of the Pu L_3 edge HR-XANES spectra.

5.3.2. Material and Methods

5.3.2.1. Pu oxidation states preparation

Pure solutions of Pu in a given oxidation state [0.01-0.03 M Pu(III), Pu(IV), Pu(V), and Pu(VI)] in 1 M $HClO_4$/$NaClO_4$ media were prepared electrochemically in an inert gas glove box starting from a purified colloid free 0.05 M Pu(III/IV) stock solution in 1 M $HClO_4$. The successive electrochemical steps are briefly outlined: an aliquot of the Pu(III/IV) stock solution was quantitatively reduced to Pu(III) at a potential of E = -400 mV [all E values are measured versus Ag/AgCl + 3 M NaCl]. Rapid oxidation of Pu(III) at E = 900 mV yielded a solution of 91% $Pu(IV)_{aq}$/9% $Pu(VI)_{aq}$. This specie was used for Pu L_3 edge HR-XANES and XAFS measurements. The later prepared $Pu(IV)_{aq}$ contained 6% of $Pu(VI)_{aq}$ and was used for Pu M_5 edge HR-XANES/RIXS measurements. Subsequent oxidation at E=1900 mV led to pure Pu(VI) solutions. An aliquot of the latter was neutralized with 1 M NaOH [final pH~4] and carefully reduced to pure Pu(V) by applying a potential of E=600 mV. For all spectroscopy measurements, a 350 µl aliquot was taken from each fraction before the following electrochemical step. Vis-NIR spectra of the samples were recorded before and after the synchrotron based measurements. For the Pu(V) sample, 7% of the initial Pu(VI) had transformed to other Pu oxidation states [Pu(IV) + Pu(VI)]. 0.004 M colloidal Pu(IV) solution in 1 M $HClO_4$ [96% $Pu(IV)_{col}$ + 4% $Pu(IV)_{aq}$] was obtained by separation of Pu(IV) colloids from a supersaturated Pu(IV) solution using a 10 kD (2 nm) ultrafiltration step and used for all spectroscopic measurements. 100% purity was achieved for the Pu(III) and Pu(VI) solutions. (Pu oxidation state preparations were done by Dr. David Fellhauer, INE).

5.3.2.2. Pu L_3 edge XAFS and L_3/M_5 edges HR-XANES/RIXS measurements

The Pu L_3 edges HR-XANES, Pu M_5 edge HR-XANES/XANES/RIXS and L_3 edge XAFS were measured as described in Sections 3.1 and 3.2. The spectral energy range was from 17973 eV to 18103 eV with 0.5 eV step size for L_3 edge HR-XANES and 3760 eV to 3840 eV with 0.1 eV step size for M_5 edge HR-XANES/XANES. 3*d*4*f* RIXS maps were measured for emission energies from 3335 eV to 3355 eV with 0.33 eV step size and incident energies from 3770 to 3793 eV with 0.5 eV step size. An in-house designed inert-gas cell [54] was used for the Pu L_3 edge HR-XANES and EXAFS measurements. For M_5 edge HR-XANES/XANES/RIXS another suitable cell has been designed, tested and used for the measurements. The cell is described later in this section.

3*d*4*f* RIXS maps are useful to determine the correct maximum emission energy for measuring HR-XANES spectra. The Pu M_5 edge HR-XANES/XANES/3*d*4*f* RIXS were recorded two times. In September 2014 $Pu(III)_{aq}$, $Pu(IV)_{col}$ and $Pu(VI)_{aq}$ were studied. The Pu M_5 edge HR-XANES were measured at E_{emis}=3350.0 eV. In March 2015 Pu M_5 edge HR-XANES/XANES/3*d*4*f* RIXS were recorded for $Pu(IV)_{col}$ and $Pu(IV)_{aq}$. The 3*d*4*f* RIXS maps were measured at E_{emis}=3345.8 eV. The different emission energies can be explained by variations of the alignment of the spectrometer and have no physical meaning.

Pu L_3 edge EXAFS spectra were Fourier transformed (FT) and modeled with the ARTEMIS software (IFEFFIT). [135] The single and multiple scattering paths used to model the experimental spectra were calculated by the FEFF8.2 code. A k range of 2.7-9.5 $Å^{-1}$ was used. A shell by shell approach was applied to model the data in R space within a range of R from 1.05 to 3.7 Å for $Pu(IV)_{col}$ and from R=1.05 to 2.55 Å for the aqueous Pu species.. The amplitude reduction factor was set to unity and was fixed during the fitting process.

5.3.2.3. Quantum chemical calculations

Ab-initio quantum chemical calculations of Pu L_3 edge HR-XANES spectra and Pu *d* and *f* density of states (DOS) were performed with the FEFF 9.5 code based on the multiple scattering theory. [126] Structures of the Pu aqueous species were optimized using TURBOMOLE and DFT/BP86 with TZVP basis sets. For colloidal $Pu(IV)_{aq}$ L_3 edge HR-XANES PuO_2 crystal structure was collected from ICSD (55456). Clusters containing from 10 to 440 atoms were used for the calculation of scattering potentials. The core-hole lifetime broadening was reduced by 2.5 eV to obtain better agreement between experimental and theoretical spectra. Both dipole and dipole + quadrupole transitions are considered. All parameters used in the calculations are listed in Table 5.3.1. (Pu structures refinements were done by Dr. Bernd Schimmelpfennig, INE).

Table 5.3.1. Input parameters for Pu L_3 edge XANES FEFF9.5 calculations; * self-consistent field (SCF): controls FEFF's automated self-consistent potential calculations; ** when it is not used the f electron density is fixed at the atomic value in order to obtain well converged SCF potentials; *** used to customize the energy grid.

Specie	Edge	SCF*	Exchange Card	Unfreezef **	Egrid Card ***	Multipole	Atomic cluster size, Å
$Pu(III)_{aq}$	L_3	5.0 1 100 0.05 6	0 0 -2.5	yes	-15 0 0.2	dip/dip+quad	10
$Pu(IV)_{aq}$	L_3	5.0 1 100 0.05 6	0 0 -2.5	yes	-15 0 0.2	dip/dip+quad	10
$Pu(IV)_{col}$	L_3	5.0 1 100 0.05 6	0 0 -2.5	yes	-15 0 0.2	dip/dip+quad	240
$Pu(V)_{aq}$	L_3	5.0 1 100 0.05 6	0 0 -2.5	yes	-15 0 0.2	dip/dip+quad	10
$Pu(VI)_{aq}$	L_3	5.0 1 100 0.05 6	0 0 -2.5	yes	-15 0 0.2	dip/dip+quad	10

5.3.3. Results and Discussion

By synchrotron based investigations of Pu it is necessary to ensure that the Pu oxidation states, especially of air sensitive Pu(III) and Pu(V), are not affected during handling and transportation. X-ray induced radiation damage can also take place. Hence, the Pu oxidation states were verified before and after the HR-XANES and XAFS experiments using the Vis-NIR spectroscopy technique. This is a well-established method for Pu oxidation state analysis. [136] Vis-NIR spectra of four electrochemically prepared $Pu(III)_{aq}$-$Pu(VI)_{aq}$ oxidation states and $Pu(IV)_{col}$ measured before and after the Pu L_3 edges HR-XANES measurements are plotted in Figure 5.3.1. The Vis-NIR spectra were very similar for the species used for the Pu M_5 edge HR-XANES/RIXS as well. No significant changes in the oxidation states were detected: the spectra for $Pu(IV)_{aq}$ show insignificant variations of about 2%. One exception is $Pu(V)_{aq}$ as 7% of the initial $Pu(V)_{aq}$ has disproportionated to [$Pu(IV)_{aq}$ + $Pu(VI)_{aq}$].

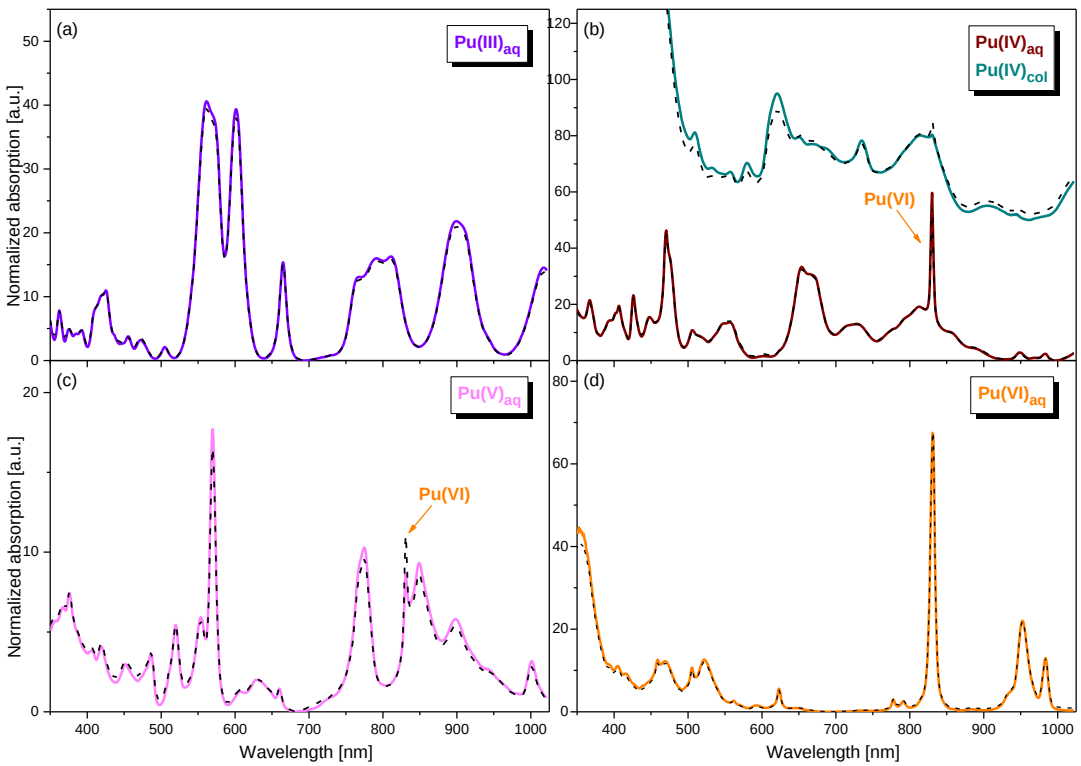

Figure 5.3.1. Vis-NIR spectra of $Pu(III)_{aq}$ (a), $Pu(IV)_{aq}$ (b, bottom), $Pu(IV)_{col}$ (b, top), $Pu(V)_{aq}$ (c) and $Pu(VI)_{aq}$ (d) before (coloured curve) and after (black dashed curve) the experiments.

5.3.3.1. Pu L_3 edge HR-XANES

The conventionally measured Pu L_3 edge XANES and HR-XANES spectra are plotted in Figures 5.3.2.

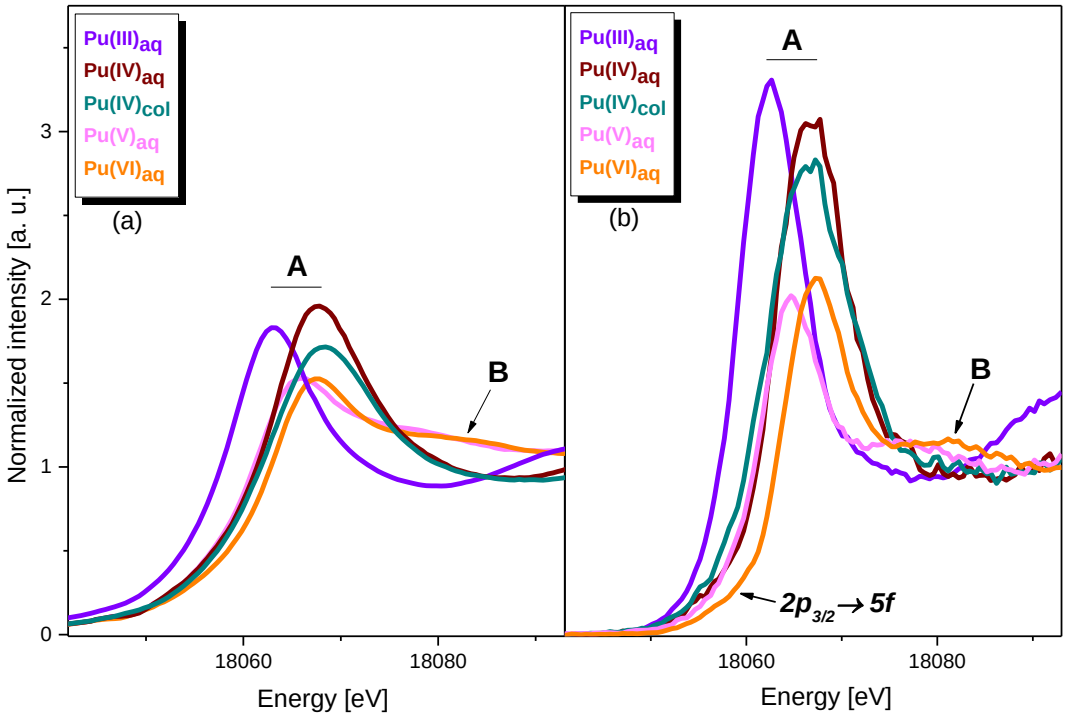

Figure 5.3.2. Conventional Pu L_3 edge (a) and HR-XANES (b) of $Pu(III)_{aq}$, $Pu(IV)_{aq}$, $Pu(IV)_{col}$, $Pu(V)_{aq}$ and $Pu(VI)_{aq}$.

The WLs (peak A) have higher intensities for all HR-XANES spectra compared to the conventional XANES. Additionally, the $Pu(V)_{aq}$ and $Pu(VI)_{aq}$ HR-XANES spectra exhibit better energy resolved post-edge features. The energy distance (ΔE) between features B and C measures the bond length (R) between Pu and the axial oxygen atoms (O_{axial}): $\Delta E \cdot R^2 = const$ for actinyl-type oxygen bonding typical for $Pu(V)_{aq}$ and $Pu(VI)_{aq}$. [19, 137] It is estimated, that the energy distance between WL and post-edge is 1.7 eV larger for $Pu(V)_{aq}$ compared to $Pu(VI)_{aq}$ and agrees with the change in U-O_{axial} bond distances, which is decreasing from 1.82 Å in $Pu(V)_{aq}$ to 1.74 Å in $Pu(VI)_{aq}$. The HR-XANES spectra allow for more precise evaluation of these distances compared to the conventional spectra.

The energy positions of the most intense feature A of the HR-XANES spectra range from 18059.7 eV for $Pu(III)_{aq}$ to 18064.3 eV for $Pu(VI)_{aq}$ (Table 5.3.2). It is often used for Pu oxidation states analyses.

Table 5.3.2. Energy positions of spectral features for the $Pu(III)_{aq}$, $Pu(IV)_{aq}$, $Pu(IV)_{col}$, $Pu(V)_{aq}$ and $Pu(VI)_{aq}$ for Pu L_3 and M_5 edge HR-XANES spectra. (error bars: ± 0.25 eV (L_3 edge), ± 0.05 eV (M_5 edge)).

Specie	A, [eV]	ΔE, [eV]	B, [eV]	(B-A), [eV]
		L_3 edge		
$Pu(III)_{aq}$	18062.4	0	-	-
$Pu(IV)_{aq}$	18066.8	4.5	-	-
$Pu(IV)_{col}$	18066.8	4.5	-	-
$Pu(V)_{aq}$	18064.8	2.4	18077.3	12.5
$Pu(VI)_{aq}$	18067.5	5.1	18081.7	14.2
		M_5 edge		
$Pu(III)_{aq}$	3774.7	0	-	-
$Pu(IV)_{aq}$	3776.4	1.7	-	-
$Pu(IV)_{col}$	3776.1	1.4	-	-
$Pu(VI)_{aq}$	3777.0	2.3	3781.2	4.2

Quantum chemical calculations performed with the FEFF9.5 code are depicted in Figure 5.3.3. The Pu *d* and *f* density of states (*d*-, *f*-DOS) are plotted along with the Pu L_3 edge HR-XANES spectra. The L_3 edge HR-XANES describes excitation of $2p_{3/2}$ electrons predominately to *d* and *s* unoccupied states as implied by dipole selections rules (the angular momentum quantum number changes by ± 1). All spectra are described mainly by the unoccupied *d*-DOS as it has been previously observed for U. [55], [68]

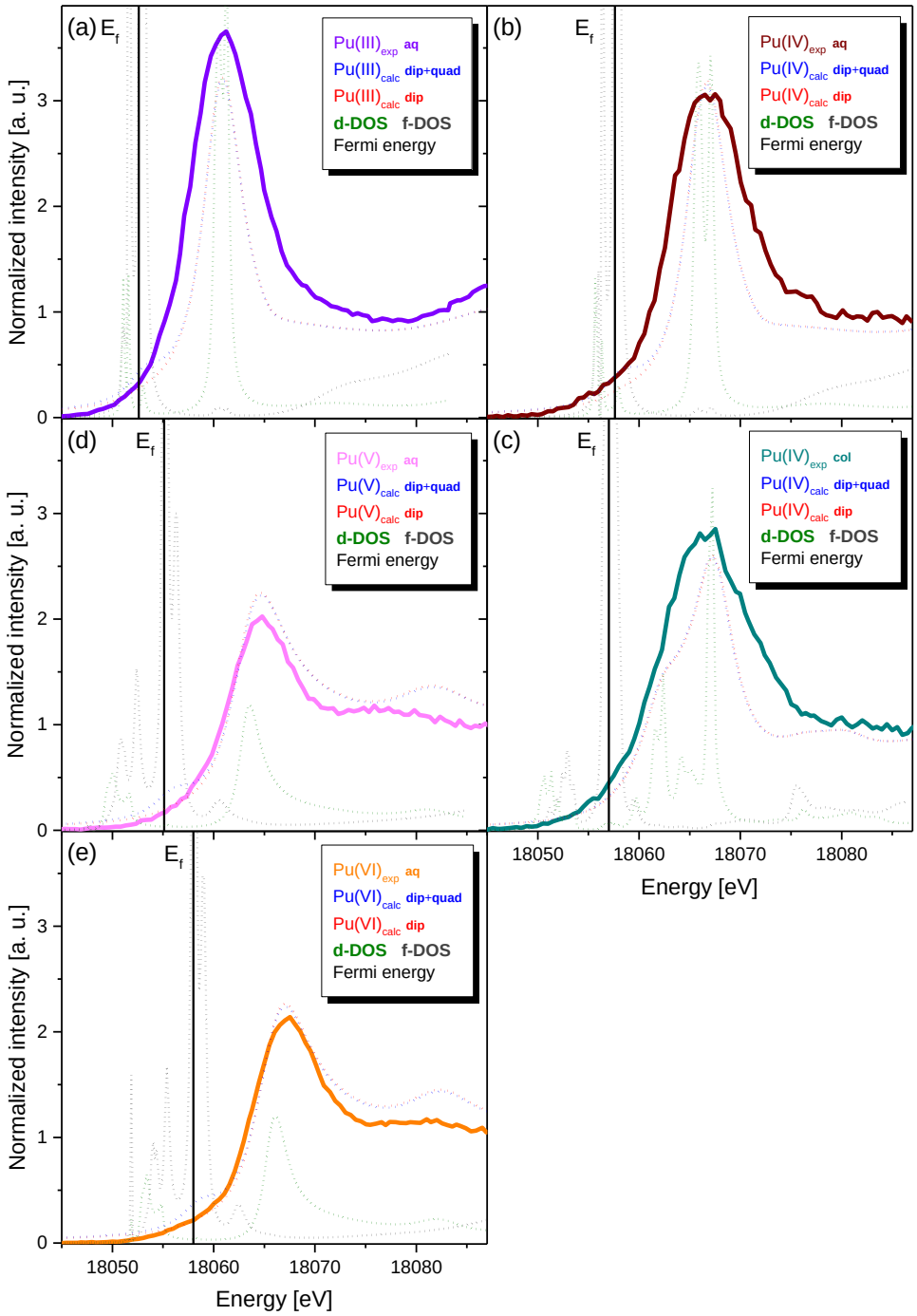

Figure 5.3.3. Pu L_3 edge HR-XANES spectra, FEFF9.5 calculations of HR-XANES spectra and *d*- and *f*-DOS of aqueous $Pu(III)_{aq}$ (a), $Pu(IV)_{aq}$ (b), $Pu(IV)_{col}$ (c), $Pu(V)_{aq}$ (d) and $Pu(VI)_{aq}$ (e).

The Pu L_3 edge HR-XANES spectra of $Pu(V)_{aq}$ and $Pu(VI)_{aq}$ suggest the presence of a pre-edge feature not visible in the conventional spectrum. The still large core-hole and experimental broadening affect the spectra and prevent detection of these weak absorption resonances. A pre-edge is mainly expected for higher Pu oxidation states of the $(PuO_2)^{2+}$ ion, Pu(VI) (Figure 5.3.3 e), due to a higher number of *f* electron vacancies in the 5*f* shell. Possible contributions of transitions to *f* states to the pre-edge region of the spectra have been explored. A pre-edge absorption resonance appears in the spectra only by considering dipole and quadrupole transitions in the calculations, whereas no pre-edge is found when dipole transitions are included (Figure 5.3.3 e). The spectrum of $Pu(VI)_{aq}$ calculated by FEFF9.5 has the best agreement with the experimental HR-XANES spectrum. A well resolved multi peak structure arises in the *d*-DOS of $Pu(IV)_{col}$ spectrum and a double peak in the *d*-DOS of $Pu(IV)_{aq}$. The peak A and post-edge peak positions in $Pu(VI)_{aq}$ agree well with the experimental spectrum, whereas in $Pu(V)_{aq}$ the post-edge is shifted considerably to higher energies. This indicates that the calculated Pu-O_{axial} distance (1.74 Å) is shorter by 0.08 Å as compared to the experimentally determined Pu-O_{axial} bond distance (1.82 Å). EXAFS analyses confirm this observation.

5.3.3.2. Pu L_3 edge EXAFS

The Pu L_3 edge FT-EXAFS spectra in R-space are presented in Figure 5.3.4.

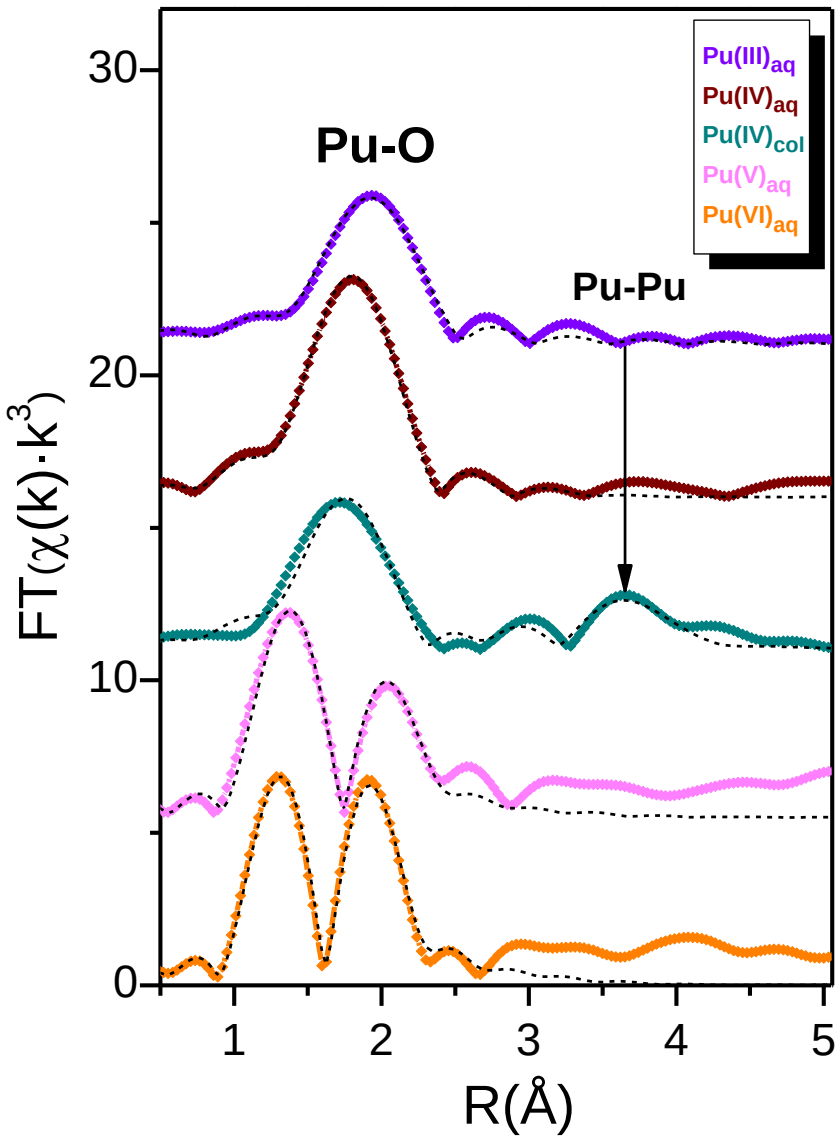

Figure 5.3.4. R-space fit results for the $Pu(III)_{aq}$, $Pu(IV)_{aq}$, $Pu(IV)_{col}$, $Pu(V)_{aq}$ and $Pu(VI)_{aq}$ Fourier transformed magnitude of EXAFS data (coloured rhombs) and their best fits (dash dot line). The arrow indicated Pu-Pu coordination peak in $Pu(IV)_{col}$.

Pu(III) and Pu(IV) are bound to the O atoms of water molecules: coordination number (N)=10.5(8) at 2.48(1) Å (Pu(III)) and N=11.2(5) at 2.34(1) Å (Pu(IV)) (Table 5.3.3). An additional peak at about 3.78 Å is found in the $Pu(IV)_{col}$ spectrum, which is assigned to the Pu second coordination sphere. The low amplitude of this peak indicates coordination to a small number of Pu atoms (6) compared to stoichiometric bulk PuO_2 (12) and may account for disorder and low dimensions of the colloids. [138] The Pu(V) and Pu(VI) FT-EXAFS spectra exhibit two intense peaks. The peak at lower Pu-O distance originates from the O_{axial} atoms of the plutonyl ion, whereas the second intense peak describes the scattering of the photoelectron from the equatorial O atoms of the water ligands. The fit analyses show that the axial and equatorial Pu-O distances are 1.74(1) Å (Pu(VI)), 1.82(1) Å (Pu(V)) and 2.39(1) Å (Pu(VI)), 2.50(1) Å (Pu(V)), respectively (Table 5.3.3). The results are in a good agreement with those obtained in a previous Pu oxidation states EXAFS study. [19] Additional plots of EXAFS data and best fits are given in Appendix, Figures AIII.1-3.

Table 5.3.3. EXAFS fit results: SP - scattering path, N – coordination number, R – bond distance, σ^2 - Debye-Waller factor, ΔE_0 – energy shift of the ionization potential, S_0^2 – amplitude reduction factor and r - goodness of fit parameter. Errors are given in the parentheses as the last decimal in the fit value.

Sample	SP	N	R, [Å]	ΔE_0, [eV]	$\sigma^2[\cdot 10^{-3}Å^2]$	S_0^2	r
$Pu(III)_{aq}$	Pu-O1	10.5 (8)	2.48 (1)	-3.2 (8)	10 (2)	1.0	0.001
$Pu(IV)_{aq}$	Pu-O1	11.2 (5)	2.34 (1)	-4.4 (5)	10 (1)	1.0	0.001
$Pu(IV)_{col}$	Pu-O1	7.9 (1)	2.30 (1)	4.2 (8)	10 (1)	1.0	0.006
	Pu-Pu	6.2 (9)	3.78 (2)				
$Pu(V)_{aq}$	Pu-O1	2.0 (4)	1.82 (2)	5.2 (7)	3 (2)	1.0	0.005
	Pu-O2	2.7 (3)	2.50 (1)				
$Pu(VI)_{aq}$	Pu-O1	1.7 (2)	1.74 (1)	5.5 (9)	6 (5)	1.0	0.002
	Pu-O2	3.6 (4)	2.39 (1)	2.5 (9)	4 (5)		

5.3.3.3. Pu M_5 edge HR-XANES

For the first time ever aqueous Pu species have been analyzed applying the HR-XANES technique at the Pu M_5 edge. One essential part of these experiments performed at the INE-Beamline was the design development, manufacture and tests of a suitable liquid cell. The main challenge was to avoid the chemical reaction of the $HClO_4$ solution with the polyether ether ketone (PEEK) cell and the 13 µm thick Kapton window embedded onto the frame made from a Kapton tape (Figure 5.3.5).

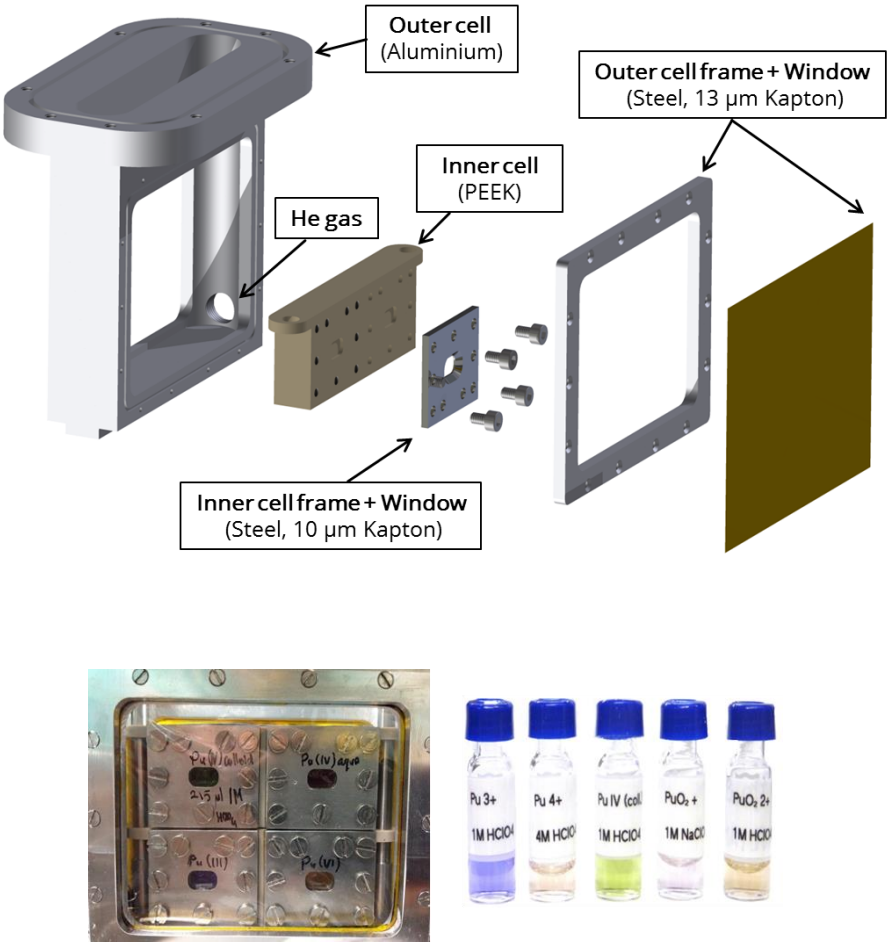

Figure 5.3.5. 3*D* design (top) and a photograph (bottom left) of the *An* $M_{4,5}$ edge HR-XANES liquid cell (top). In the first version of the cell 10 µm PP has been used as a window material; as a result the colour of the Pu oxidation states can be distinguished and correlate well with the colours of the laboratory prepared Pu oxidation states (photograph bottom right) used for the Pu M_5 edge HR-XANES/RIXS measurements.

1M $HClO_4$ was found to be appropriate as no chemical damage of the cell and the window as well as no significant evaporation was observed after the acid solution remained in the cell for seven days. Four of the liquid cells were placed in an inert gas cell, which has an adapted design of the standard INE-Beamline inert-gas cell, [54] including larger windows and an inner volume (Figure 5.3.5). A single Pu M_5 edge HR-XANES spectrum was measured for 60 min for a sample containing 0.05 M Pu. The intensity measured at the maximum of the WL of the Pu M_4 edge HR-XANES spectrum was 1760 counts/s at 122 mA ring current. Two scans were sufficient to obtain a high signal to noise ratio and to check for the reproducibility of the spectral features (Figure 5.3.6 a, b, c, d).

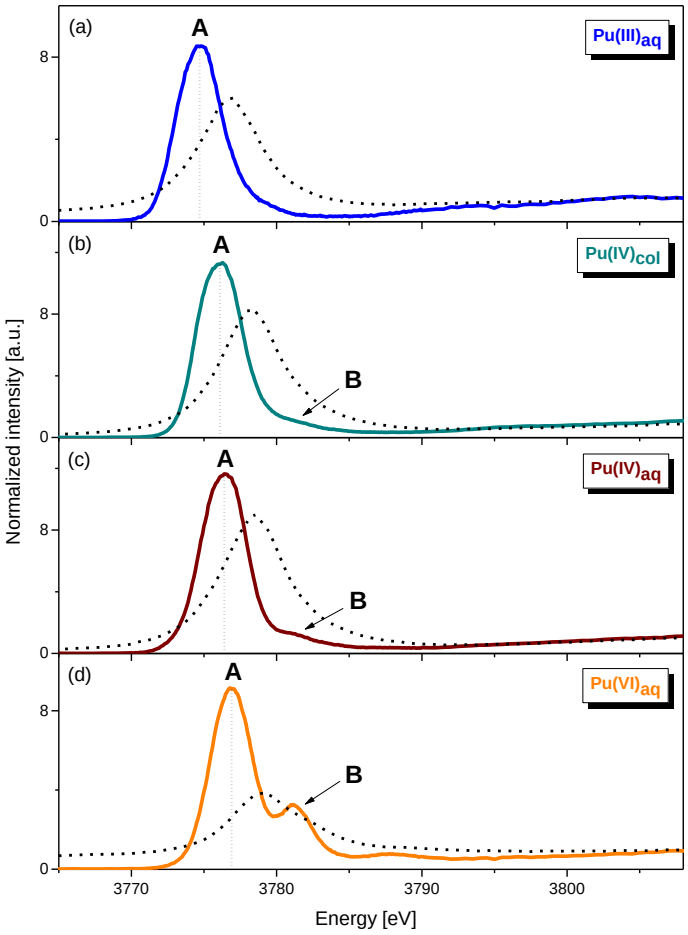

Figure 5.3.6. Conventional Pu M_5 edge (black dashed curves) and HR-XANES (coloured curves) spectra of $Pu(III)_{aq}$ (a), $Pu(IV)_{col}$ (b), $Pu(IV)_{aq}$ (c), and $Pu(VI)_{aq}$ (d).

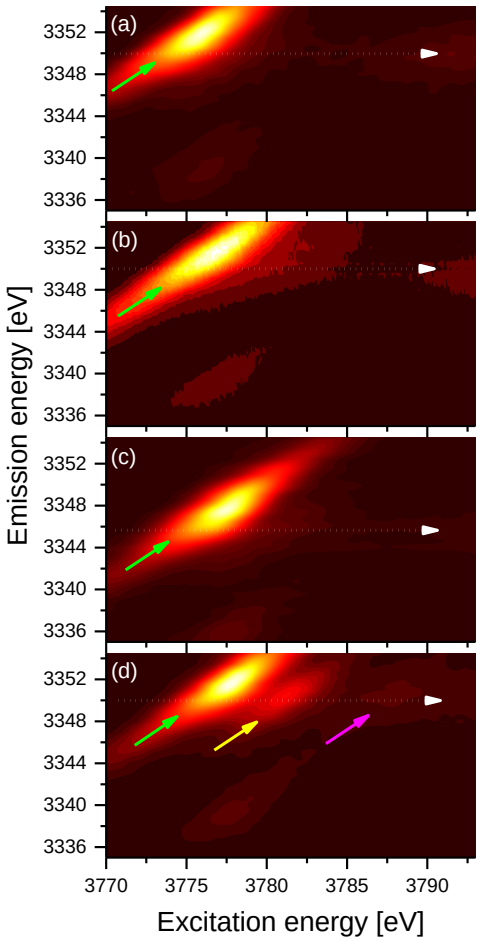

Figure 5.3.7. 3*d*4*f* RIXS maps of $Pu(III)_{aq}$ (a), $Pu(IV)_{col}$ (b), $Pu(IV)_{aq}$ (c), and $Pu(VI)_{aq}$ (d).

The Pu M_5 edge HR-XANES spectra obtained for the $Pu(III)_{aq}$, $Pu(IV)_{col}$, $Pu(IV)_{aq}$ and $Pu(VI)_{aq}$ species are plotted in Figure 5.3.5 in comparison to conventional M_5 edge XANES spectra recorded in total fluorescence yield detection mode. The spectra exhibit narrower transition features compared to the conventional measurements due to smaller contribution of core-hole lifetime broadening effects. The Pu M_5 edge HR-XANES describe transitions of $3d_{5/2}$ electrons to unoccupied U 5*f* states. The 5*f* valence states of *An* have a significant role in the chemical bonding. [37, 139] The main absorption peak of the HR-XANES spectra shifts to higher energies following the trend $Pu(III)_{aq}$ (0 eV) < $Pu(IV)_{col}$ (+1.4 ± 0.05 eV) < $Pu(IV)_{aq}$ [+ 6% $Pu(VI)_{aq}$] (+1.7 ± 0.05 eV) < $Pu(VI)_{aq}$ (+2.3 ± 0.05 eV) (Table 5.3.2). The spectrum of Pu(VI) exhibits additional structures not observed in the conventional measurement. Pu(VI) is bound to two axial O atoms ($Pu\text{-}O_{axial}$) forming short, linear bonds with a geometry analogous to the uranyl moiety. The Pu M_5 edge HR-XANES resembles that of the U M_4 edge U(VI) spectrum of $UO_3 \cdot 1\text{-}2H_2O$ discussed in Section 5.2. The absorption resonances A and B can be assigned similarly to electronic transitions from the $3d_{5/2}$ core level to $5f\delta/5f\phi$, $5f\pi$ (A), and $5f\sigma$ (B) orbitals. The varying intensities and energy positions arise from differences in valence electronic configuration ($5f^0$ for U(VI) and $5f^2$ for Pu(VI)) but can be as well influenced by the increased nuclear charge of Pu compared to U as well as the bonding interactions with the axial and equatorial ligands. How the Pu M_5 edge HR-XANES spectrum is affected by these factors will be investigated by future quantum chemical calculations and comparison with suitable reference systems.

Figure 5.3.6 depicts the Pu M_5 edge HR-XANES spectrum of the $Pu(IV)_{col}$ and the 94% $Pu(IV)_{aq}$ + 6% $Pu(VI)_{aq}$ samples. The method is clearly very sensitive to small variations of the Pu oxidation states as the spectrum containing 6% of Pu(VI) shifts with +0.3 eV to higher energies. In addition, a structure grows in intensity at the energy position (3782.2 eV) characteristic for the main absorption peak of Pu(VI) (arrow in Figure 5.3.8).

The Pu L_3 edge HR-XANES technique has much lower sensitivity. This is demonstrated in Figure 5.3.2 b. It is well visible that there is no energy shift between the Pu L_3 edge XANES and HR-XANES spectra of $Pu(IV)_{aq}$ and $Pu(IV)_{col}$. Note that about 9% $Pu(VI)_{aq}$ were present in the $Pu(IV)_{aq}$ sample.

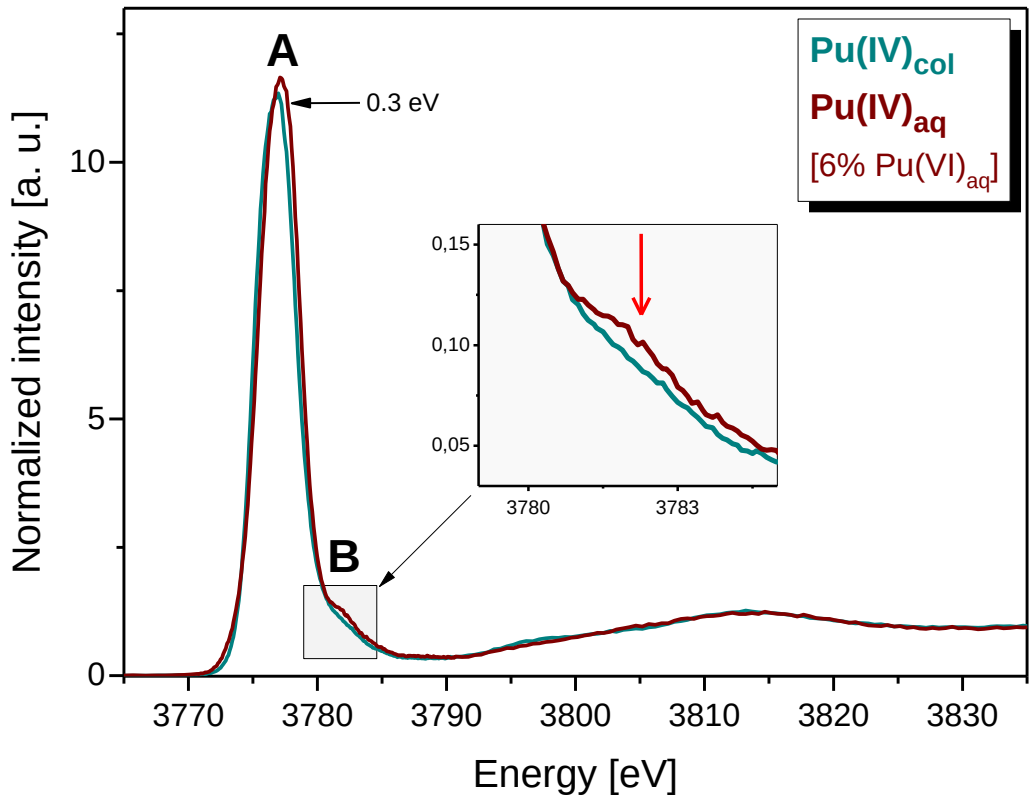

Figure 5.3.8. Pu M_5 edge HR-XANES spectra of $Pu(IV)_{col}$ and [$Pu(IV)_{aq}$ + 6% $Pu(VI)_{aq}$]. Peak B is enlarged in the inset.

The peaks visible in the HR-XANES spectra can be clearly correlated to the more intensive structures of the 3*d*4*f* RIXS maps (Figure 5.3.7). All 3*d*4*f* RIXS maps exhibit also weak resonances located at lower emission energy corresponding to $4f_{5/2} \rightarrow 3d_{5/2}$ transitions.

The HR-XANES spectra are cut through the RIXS maps (see arrows in Figure 5.3.7) at the energy positions of the maxima of the normal emission lines measured well above the Pu M_5 absorption edge (3778 eV). These normal emission lines overlap for the different Pu oxidation states. It is well visible that the absorption resonances are shifted by ~1.35 eV to higher emission energies compared to the normal emission in the 3*d*4*f* RIXS maps. This indicates that the $3d^9 5f^{n+1}$ electronic configuration in the intermediate state of e.g. Pu(VI) screens better the core-hole compared to the completely ionized case $3d^9 5f^n$. Interestingly, the effect is not that strong for U(VI) (Section 5.1, Figure 5.3.6) as the main resonance is shifted only by about +1 eV compared to the normal emission. This can be explained with the more delocalized *f* states of U compared to Pu and therefore weaker interaction of the electron excited in the 5*f* states with the core-hole for U compared to Pu.

5.3.4. Conclusion

Pu L_3 and M_5 edge HR-XANES and 3*d*4*f* RIXS spectra of Pu(III), Pu(IV), Pu(V) and Pu(VI) in aqueous solution as well as colloidal Pu(IV) have been measured. The spectra have reduced spectral broadening resulting in better energy resolved features for all regions of the spectra. Pu M_5 edge HR-XANES spectra measure relative energies of Pu 5*f* valence orbitals and thereby can help to benchmark and drive improvement in theoretical calculations of electronic structures of Pu. In addition, the HR-XANES technique is valuable in speciation investigations as it provides increased sensitivity to minor contributions of Pu oxidation states in samples containing mixtures. It is expected that the resolution and photon flux will increase at the new CAT-ACT Beamline (ANKA), which will allow performing the analyses of *An* oxidation states for diluted samples. In principle, HR-XANES should allow to detect experimentally the 2-4% of Pu(V) in the $Pu(V)_{2x}Pu(IV)_{1-2x}O_{2+x}$(s,hyd) compound, which has been postulated based on thermodynamic calculations by Neck and colleague. [20]

It is demonstrated that the 3*d*4*f* RIXS can be used as a tool for investigations of the level of delocalization of 5*f* valence orbitals of *An* for samples in solid, liquid phase and during chemical reactions as well as under extreme conditions.

6. Summary and Outlook

In this Doctoral Project it was for the first time unambiguously demonstrated that the U(V) redox state is stable for up to 373 days when incorporated in octahedral sites of magnetite nanoparticles at concentrations of 1000 ppm of U(VI) when co-precipitated with magnetite. The stabilization of U(V) in the structure of magnetite did not appear to depend on the U concentration. U concentrations (3000-10000 ppm) above the solubility limit (~1000 ppm) of U(VI) led to precipitation of U(VI) phases, which recrystallize to UO_{2+x} after more than 10 days interaction with the magnetite particles. The results clearly demonstrated that there are redox and recrystallization processes with relatively slow (> 10 days) kinetics. U(V) is also found to substantially contribute after reaction of Fe(II) with U(VI) sorbed for 175 days on the magnetite nanoparticles. The unambiguous characterization of U(V) is a breakthrough in a long discussion and will likely motive future broad application of the U M_4 edge HR-XANES for geochemical speciation investigations of U. In such type of investigations, the short-term U redox speciation and kinetics can been studied in more details under controlled pH/E_h conditions by *in-situ* U M_4 edge HR-XANES experiments. In combination with *in-situ* XRD, this allows for the recrystallization processes of Fe to be followed during the formation process of magnetite. It has been demonstrated that a fingerprint approach using U M_4 edge HR-XANES can be effectively applied for characterization of U-*yl* and U-*ate* type of U-O_{axial} chemical bonds. Using this approach it was shown that U-O_{axial} bonds likely have more covalent character in γ-UO_3 compared to α-UO_3. The order of the increase in covalency in the UO_3 polymorphs was found to be the same as suggested by the spectroscopy and the thermodynamic results based on comparison of Gibbs free energies of formation (α-UO_3 < β-UO_3 < γ-UO_3 < $UO_3 \cdot 1\text{-}2H_2O$). These studies also demonstrated the very high sensitivity of the *An* $M_{4,5}$ edge HR-XANES to small changes of the U-O_{axial} chemical bond.

It was shown that both $M_{4,5}$ and L_3 edges HR-XANES and RIXS immerge as highly valuable for investigations of 5*f* and 6*d* valence states of *An*. For the first time an *in-situ* cell combining electrochemistry with UV-Vis and U M_4 edge HR-XANES has been developed, built and applied for the characterization of the U 5*f* valence states of U(VI) and U(V) carbonate complexes that are free from experimental artefacts. Changes in the relative energies of the 5f based orbitals of the U and the energy shift of the absorption edge induced by the presence of an additional electron in the 5*fδ* orbital of U(V) are measured. The oscillator strengths for $3d_{3/2} \rightarrow 5f\delta$ transitions are compared for U(VI) and U(V) by evaluating the areas of the first most intense spectral peaks. The 5*fδ* orbital is the LUMO and has non-bonding character for both compounds, i.e. no ligand orbitals have significant contributions. The larger relative change in the area of the 5*fδ* peak compared to the area of the entire spectrum upon reduction of U(VI) to U(V) suggests less mixing of 2*p* ligand with metal 5*f* valence orbitals. These results indicate reduced covalency of the U-ligand bonding for the U(V) compound and will be verified with quantum chemical calculations currently being carried out. The area of each peak is proportional to the 5*f* content of the molecular orbital, which this peak probes. The U M_4 edge HR-XANES results compared to equivalent measurements performed in conventional transmission and total fluorescence yield mode in order to validate if the HR-XANES is directly proportional to the absorption cross section.

As a following step the *in-situ* cell can be upgraded for spectroscopic studies of the complete environmentally relevant U oxidation states series U(IV)-U(V)-U(VI) and of redox reactions of other *An*.

A set of inert gas liquid cells have been designed built and applied for Pu L_3 and M_5 edge HR-XANES/RIXS investigations of Pu(III)-Pu(IV)-Pu(V)-Pu(VI) in perchloric acid for the first time. The changes of the Pu 5*f* and 6*d* unoccupied states and the energy shifts of the absorption edges of the spectra as a function of the additional 5*f* electrons upon reduction of Pu from Pu(III) to Pu(VI) have been measured. Due to difficulties in stabilizing Pu(V) for sufficiently high Pu concentrations, it was not possible to measure the Pu M_5 edge HR-XANES/RIXS spectra of the this Pu specie. Comparison of Pu with U *3d4f* RIXS demonstrated that this technique can be used for precise measurements of the level of localization of 5*f* orbitals of *An*. It also revealed that the Pu L_3 edge HR-XANES can be applied for detection of small changes in the Pu-O bond distances for $(PuO_2)^{2+}$ containing species. This is particularly important for samples with low Pu content (< 200 ppm), which is below the limit of detection for EXAFS measurements.

The work presented in this dissertation demonstrated the high sensitivity of the *An* $M_{4,5}$ edge HR-XANES techniques compared to the *An* L_3 edge XANES/HR-XANES for detection of *An* oxidation states present in small amounts in mixtures. Reference spectra are needed for speciation analyses of U and Pu in laboratory and environmental systems, and have been measured. Currently the methods under development are expected to provide quantitative information.

In a future experiment at the CAT-ACT beamline at ANKA, it will be attempted to detect for the first time experimentally the 2-4% of Pu(V) shown by thermodynamic calculation by Neck and colleagues to exist in the $Pu(V)_{2x}Pu(IV)_{1-2x}O_{2+x}$ (s,hyd) compound. [20].

List of References

[1] C. Walther, J. Rothe, B. Brendebach, M. Fuss, M. Altmaier, C.M. Marquardt, S. Buechner, H.R. Cho, J.I. Yun, A. Seibert, New insights in the formation processes of Pu(IV) colloids, Radiochim Acta, 97 (2009) 199-207.

[2] H. Geckeis, J. Lutzenkirchen, R. Polly, T. Rabung, M. Schmidt, Mineral-Water Interface Reactions of Actinides, Chem Rev, 113 (2013) 1016-1062.

[3] M. Altmaier, X. Gaona, T. Fanghanel, Recent Advances in Aqueous Actinide Chemistry and Thermodynamics, Chem Rev, 113 (2013) 901-943.

[4] O.N. Batuk, S.D. Conradson, O.N. Aleksandrova, H. Boukhalfa, B.E. Burakov, D.L. Clark, K.R. Czerwinski, A.R. Felmy, J.S. Lezama-Pacheco, S.N. Kalmykov, D.A. Moore, B.F. Myasoedov, D.T. Reed, D.D. Reilly, R.C. Roback, I.E. Vlasova, S.M. Webb, M.P. Wilkerson, Multiscale Speciation of U and Pu at Chernobyl, Hanford, Los Alamos, McGuire AFB, Mayak, and Rocky Flats, Environ Sci Technol, 49 (2015) 6474-6484.

[5] M.A. Denecke, Actinide speciation using X-ray absorption fine structure spectroscopy, Coordin Chem Rev, 250 (2006) 730-754.

[6] S.D. Conradson, B.D. Begg, D.L. Clark, C. den Auwer, M. Ding, P.K. Dorhout, F.J. Espinosa-Faller, P.L. Gordon, R.G. Haire, N.J. Hess, R.F. Hess, D.W. Keogh, G.H. Lander, D. Manara, L.A. Morales, M.P. Neu, P. Paviet-Hartmann, J. Rebizant, V.V. Rondinella, W. Runde, C.D. Tait, D.K. Veirs, P.M. Villella, F. Wastin, Charge distribution and local structure and speciation in the UO2+x and PuO2+x binary oxides for x <= 0.25, J Solid State Chem, 178 (2005) 521-535.

[7] M.L. Schlegel, C. Bataillon, K. Benhamida, C. Blanc, D. Menut, J.L. Lacour, Metal corrosion and argillite transformation at the water-saturated, high-temperature iron-clay interface: A microscopic-scale study, Appl Geochem, 23 (2008) 2619-2633.

[8] S. Music, M. Gotic, S. Popovic, X-Ray-Diffraction and Fourier-Transform Infrared-Analysis of the Rust Formed by Corrosion of Steel in Aqueous-Solutions, J Mater Sci, 28 (1993) 5744-5752.

[9] W. Wolski, Ordered Maghemite in Rust, Corrosion, 46 (1990) 743-745.

[10] E. Mattsson, Retrieval of Corrosion Information - Literature - Report of Efc Committee on Information and Documentation in the Field of Corrosion, Brit Corros J, 16 (1981) 125-131.

[11] B.J. Merkel, B. Planer-Friedrich, C. Wolkersdorfer, Uranium in the Aquatic Environment Proceedings of the International Conference Uranium Mining and Hydrogeology III and the International Mine Water Association Symposium Freiberg, Germany, 15-21 September 2002, in, Springer Berlin Heidelberg, Berlin, Heidelberg, 2003.

[12] R.C. Ewing, Long-term storage of spent nuclear fuel, Nat Mater, 14 (2015) 252-257.

[13] B.H. Jeon, S.D. Kelly, K.M. Kemner, M.O. Barnett, W.D. Burgos, B.A. Dempsey, E.E. Roden, Microbial reduction of U(VI) at the solid-water interface, Environ Sci Technol, 38 (2004) 5649-5655.

[14] S.D. Kelly, K.M. Kemner, E.J. O'Loughlin, J.B. Fein, D.A. Fowle, M.I. Boyanov, B.A. Bunker, N. Yee, J.D. Coates, Xafs investigations of interactions of U(VI) with Bacillus subtilis, green rust, and bio-oxidizing Dechlorosoma suillum., Abstr Pap Am Chem S, 222 (2001) U419-U419.
[15] C.S. Spirakis, The roles of organic matter in the formation of uranium deposits in sedimentary rocks, Ore Geology Reviews, 11 (1996) 53-69.
[16] E.S. Ilton, J.F. Boily, E.C. Buck, F.N. Skomurski, K.M. Rosso, C.L. Cahill, J.R. Bargar, A.R. Felmy, Influence of Dynamical Conditions on the Reduction of U-VI at the Magnetite-Solution Interface, Environ Sci Technol, 44 (2010) 170-176.
[17] M.S. Massey, J.S. Lezama-Pacheco, M.E. Jones, E.S. Ilton, J.M. Cerrato, J.R. Bargar, S. Fendorf, Competing retention pathways of uranium upon reaction with Fe(II), Geochim Cosmochim Ac, 142 (2014) 166-185.
[18] T.A. Marshall, K. Morris, G.T.W. Law, J.F. W. Mosselmans, P. Bots, H. Roberts, S. Shaw, Uranium fate during crystallization of magnetite from ferrihydrite in conditions relevant to the disposal of radioactive waste, Mineral Mag, 79 (2015) 1265-1274.
[19] S.D. Conradson, I. Al Mahamid, D.L. Clark, N.J. Hess, E.A. Hudson, M.P. Neu, P.D. Palmer, W.H. Runde, C.D. Tait, Oxidation state determination of plutonium aquo ions using x-ray absorption spectroscopy, Polyhedron, 17 (1998) 599-602.
[20] V. Neck, M. Altmaier, T. Fanghanel, Thermodynamic data for hydrous and anhydrous PuO2+x(S), J Alloy Compd, 444 (2007) 464-469.
[21] A.P. Novikov, S.N. Kalmykov, S. Utsunomiya, R.C. Ewing, F. Horreard, A. Merkulov, S.B. Clark, V.V. Tkachev, B.F. Myasoedov, Colloid transport of plutonium in the far-field of the Mayak Production Association, Russia, Science, 314 (2006) 638-641.
[22] A.B. Kersting, D.W. Efurd, D.L. Finnegan, D.J. Rokop, D.K. Smith, J.L. Thompson, Migration of plutonium in ground water at the Nevada Test Site, Nature, 397 (1999) 56-59.
[23] E.S. Ilton, S.M. Heald, Reduction of uranyl by trace to minor structural Fe(II) in phyllosilicates, Geochim Cosmochim Ac, 69 (2005) A471-A471.
[24] T.B. Scott, G.C. Allen, P.J. Heard, A.C. Lewis, D.F. Lee, The extraction of uranium from groundwaters on iron surfaces, P Roy Soc a-Math Phy, 461 (2005) 1247-1259.
[25] I.A. Teterin, A.S. Baev, V.M. Kulakov, A.L. Gubskii, A.P. Kovtun, S.B. Pirkes, G.N. Makushova, T.A. Krasovskaia, Xps Spectrum Structure of Low-Energy Electrons of Oxygen-Containing-Compounds of Lanthanides, Dokl Akad Nauk Sssr+, 259 (1981) 416-419.
[26] E.S. Ilton, J.F. Boily, P.S. Bagus, Beam induced reduction of U(VI) during X-ray photoelectron spectroscopy: The utility of the U4f satellite structure for identifying uranium oxidation states in mixed valence uranium oxides, Surf Sci, 601 (2007) 908-916.
[27] E.S. Ilton, P.S. Bagus, XPS determination of uranium oxidation states, Surf Interface Anal, 43 (2011) 1549-1560.

[28] C.J. Dodge, A.J. Francis, J.B. Gillow, G.P. Halada, C. Eng, C.R. Clayton, Association of uranium with iron oxides typically formed on corroding steel surfaces, Environ Sci Technol, 36 (2002) 3504-3511.
[29] M.C. Duff, J.U. Coughlin, D.B. Hunter, Uranium co-precipitation with iron oxide minerals, Geochim Cosmochim Ac, 66 (2002) 3533-3547.
[30] F. Huber, D. Schild, T. Vitova, J. Rothe, R. Kirsch, T. Schafer, U(VI) removal kinetics in presence of synthetic magnetite nanoparticles, Geochim Cosmochim Ac, 96 (2012) 154-173.
[31] P.S. Nico, B.D. Stewart, S. Fendorf, Incorporation of Oxidized Uranium into Fe (Hydr)oxides during Fe(II) Catalyzed Remineralization, Environ Sci Technol, 43 (2009) 7391-7396.
[32] E.J. O'Loughlin, S.D. Kelly, K.M. Kemner, XAFS Investigation of the Interactions of U-VI with Secondary Mineralization Products from the Bioreduction of Fe-III Oxides, Environ Sci Technol, 44 (2010) 1656-1661.
[33] D.M. Singer, S.M. Chatman, E.S. Ilton, K.M. Rosso, J.F. Banfield, G.A. Waychunas, U(VI) Sorption and Reduction Kinetics on the Magnetite (111) Surface, Environ Sci Technol, 46 (2012) 3821-3830.
[34] H. Veeramani, D.S. Alessi, E.I. Suvorova, J.S. Lezama-Pacheco, J.E. Stubbs, J.O. Sharp, U. Dippon, A. Kappler, J.R. Bargar, R. Bernier-Latmani, Products of abiotic U(VI) reduction by biogenic magnetite and vivianite, Geochim Cosmochim Ac, 75 (2011) 2512-2528.
[35] K.O. Kvashnina, S.M. Butorin, P. Martin, P. Glatzel, Chemical State of Complex Uranium Oxides, Phys Rev Lett, 111 (2013).
[36] M.O. Krause, J.H. Oliver, Natural Widths of Atomic K-Levels and L-Levels,K-Alpha X-Ray-Lines and Several Kll Auger Lines, J Phys Chem Ref Data, 8 (1979) 329-338.
[37] T. Vitova, J.C. Green, R.G. Denning, M. Loble, K. Kvashnina, J.J. Kas, K. Jorissen, J.J. Rehr, T. Malcherek, M.A. Denecke, Polarization Dependent High Energy Resolution X-ray Absorption Study of Dicesium Uranyl Tetrachloride, Inorg Chem, 54 (2015) 174-182.
[38] A.L. Ulery, L.R. Drees, A. Soil Science Society of, Methods of Soil Analysis: Mineralogical methods, Soil Science Society of America, 2008.
[39] A.L. Ulery, L.R. Drees, A. Soil Science Society of, Methods of Soil Analysis: Mineralogical methods. Part 5, Soil Science Society of America, 2008.
[40] J.J. Rehr, R.C. Albers, Theoretical approaches to x-ray absorption fine structure, Rev Mod Phys, 72 (2000) 621-654.
[41] E.A. Stern, Structure Determination by X-Ray Absorption, Contemp Phys, 19 (1978) 289-310.
[42] D.E. Sayers, S.M. Heald, M.A. Pick, J.I. Budnick, E.A. Stern, J. Wong, X-Ray-Beam Line at the Nsls for X-Ray Absorption Studies in Material Science, Nucl Instrum Methods, 208 (1983) 631-635.
[43] T. Reich, G. Bernhard, G. Geipel, H. Funke, C. Hennig, A. Rossberg, W. Matz, N. Schell, H. Nitsche, The Rossendorf Beam Line ROBL - a dedicated experimental station for XAFS measurements of actinides and other radionuclides, Radiochim Acta, 88 (2000) 633-637.

[44] E.A. Hudson, L.J. Terminello, B.E. Viani, J.J. Bucher, D.K. Shuh, N.M. Edelstein, M. Denecke, T. Reich, Structure of uranium sorption complexes on alumino-silicate mineral studied by X-ray absorption spectroscopy., Abstr Pap Am Chem S, 211 (1996) 100-GEOC.
[45] E.J. O'Loughlin, S.D. Kelly, R.E. Cook, R. Csencsits, K.M. Kemner, Reduction of Uranium(VI) by mixed iron(II/iron(III) hydroxide (green rust): Formation of UO2 manoparticies, Environ Sci Technol, 37 (2003) 721-727.
[46] D.E. Latta, C.A. Gorski, M.I. Boyanov, E.J. O'Loughlin, K.M. Kemner, M.M. Scherer, Influence of Magnetite Stoichiometry on U-VI Reduction, Environ Sci Technol, 46 (2012) 778-786.
[47] F.M.F. De Groot, M.H. Krisch, J. Vogel, Spectral sharpening of the Pt L edges by high-resolution x-ray emission, Physical Review B - Condensed Matter and Materials Physics, 66 (2002) 1951121-1951127.
[48] P. Glatzel, U. Bergmann, High resolution 1s core hole X-ray spectroscopy in 3d transition metal complexes - electronic and structural information, Coordin Chem Rev, 249 (2005) 65-95.
[49] E. Kleymenov, J.A. van Bokhoven, C. David, P. Glatzel, M. Janousch, R. Alonso-Mori, M. Studer, M. Willimann, A. Bergamaschi, B. Henrich, M. Nachtegaal, Five-element Johann-type x-ray emission spectrometer with a single-photon-counting pixel detector, Rev Sci Instrum, 82 (2011).
[50] P. Glatzel, T.C. Weng, K. Kvashnina, J. Swarbrick, M. Sikora, E. Gallo, N. Smolentsev, R.A. Mori, Reflections on hard X-ray photon-in/photon-out spectroscopy for electronic structure studies, J Electron Spectrosc, 188 (2013) 17-25.
[51] T. Vitova, M.A. Denecke, J. Göttlicher, K. Jorissen, J.J. Kas, K. Kvashnina, T. Prüßmann, J.J. Rehr, J. Rothe, Actinide and lanthanide speciation with high-energy resolution X-ray techniques, Journal of Physics: Conference Series, 430 (2013) 012117.
[52] J.P. Rueff, S. Raymond, A. Yaresko, D. Braithwaite, P. Leininger, G. Vankó, A. Huxley, J. Rebizant, N. Sato, Pressure-induced f -electron delocalization in the U-based strongly correlated compounds U Pd3 and U Pd2 Al3: Resonant inelastic x-ray scattering and first-principles calculations, Physical Review B - Condensed Matter and Materials Physics, 76 (2007).
[53] K. Hamalainen, D.P. Siddons, J.B. Hastings, L.E. Berman, Elimination of the Inner-Shell Lifetime Broadening in X-Ray-Absorption Spectroscopy, Phys Rev Lett, 67 (1991) 2850-2853.
[54] J. Rothe, S. Butorin, K. Dardenne, M.A. Denecke, B. Kienzler, M. Loble, V. Metz, A. Seibert, M. Steppert, T. Vitova, C. Walther, H. Geckeis, The INE-Beamline for actinide science at ANKA, Rev Sci Instrum, 83 (2012).
[55] T. Vitova, K.O. Kvashnina, G. Nocton, G. Sukharina, M.A. Denecke, S.M. Butorin, M. Mazzanti, R. Caciuffo, A. Soldatov, T. Behrends, H. Geckeis, High energy resolution x-ray absorption spectroscopy study of uranium in varying valence states, Phys Rev B, 82 (2010).
[56] K.O. Kvashnina, Y.O. Kvashnin, S.M. Butorin, Role of resonant inelastic X-ray scattering in high-resolution core-level spectroscopy of actinide materials, J Electron Spectrosc, 194 (2014) 27-36.

[57] J.L. Campbell, T. Papp, WIDTHS OF THE ATOMIC K–N7 LEVELS, Atomic Data and Nuclear Data Tables, 77 (2001) 1-56.
[58] S.M. Butorin, D.K. Shuh, K.O. Kvashnina, J.H. Guo, L. Werme, J. Nordgren, Chemical Reduction of Actinides Probed by Resonant Inelastic X-ray Scattering, Anal Chem, 85 (2013) 11196-11200.
[59] F. de Groot, High-Resolution X-ray Emission and X-ray Absorption Spectroscopy, Chem Rev, 101 (2001) 1779-1808.
[60] B. Ravel, M. Newville, ATHENA, ARTEMIS, HEPHAESTUS: data analysis for X-ray absorption spectroscopy using IFEFFIT, J Synchrotron Radiat, 12 (2005) 537-541.
[61] A. Ankudinov, S. Conradson, J.J. Rehr, Self-consistent calculations of XANES in Pu hydrates., Abstr Pap Am Chem S, 214 (1997) 52-Geoc.
[62] J.J. Rehr, J.J. Kas, F.D. Vila, M.P. Prange, K. Jorissen, Parameter-free calculations of X-ray spectra with FEFF9, Phys Chem Chem Phys, 12 (2010) 5503-5513.
[63] M.P. Seah, L.S. Gilmore, G. Beamson, XPS: Binding energy calibration of electron spectrometers 5 - Re-evaluation of the reference energies, Surf Interface Anal, 26 (1998) 642-649.
[64] J.F. Moulder, J. Chastain, Handbook of X-ray Photoelectron Spectroscopy: A Reference Book of Standard Spectra for Identification and Interpretation of XPS Data, Physical Electronics, 1995.
[65] J. Goettlicher, A. Kotelnikov, N. Suk, A. Kovalski, T. Vitova, R. Steininger, Sulfur K X-ray absorption near edge structure spectroscopy on the photochrome sodalite variety hackmanite, Z Kristallogr, 228 (2013) 157-171.
[66] A.P. Hammersley, S.O. Svensson, M. Hanfland, A.N. Fitch, D. Häusermann, Two-dimensional detector software: From real detector to idealised image or two-theta scan, High Pressure Research, 14 (1996) 235-248.
[67] T.A. Marshall, K. Morris, G.T.W. Law, F.R. Livens, J.F.W. Mosselmans, P. Bots, S. Shaw, Incorporation of Uranium into Hematite during Crystallization from Ferrihydrite, Environ Sci Technol, 48 (2014) 3724-3731.
[68] A. Walshe, T. Prussmann, T. Vitova, R.J. Baker, An EXAFS and HR-XANES study of the uranyl peroxides [UO2(eta(2)-O-2)(H2O)(2)]center dot nH(2)O (n=0, 2) and uranyl (oxy)hydroxide [(UO2)(4)O(OH)(6)]center dot 6H(2)O, Dalton T, 43 (2014) 4400-4407.
[69] M.I. Boyanov, E.J. O'Loughlin, E.E. Roden, J.B. Fein, K.M. Kemner, Adsorption of Fe(II) and U(VI) to carboxyl-functionalized microspheres: The influence of speciation on uranyl reduction studied by titration and XAFS, Geochim Cosmochim Ac, 71 (2007) 1898-1912.
[70] J. Baumgartner, A. Dey, P.H.H. Bomans, C. Le Coadou, P. Fratzl, N.A.J.M. Sommerdijk, D. Faivre, Nucleation and growth of magnetite from solution, Nat Mater, 12 (2013) 310-314.
[71] J.P. Jolivet, C. Chaneac, E. Tronc, Iron oxide chemistry. From molecular clusters to extended solid networks, Chem Commun, (2004) 481-487.

[72] L. Vayssieres, C. Chaneac, E. Tronc, J.P. Jolivet, Size tailoring of magnetite particles formed by aqueous precipitation: An example of thermodynamic stability of nanometric oxide particles, J Colloid Interf Sci, 205 (1998) 205-212.
[73] R.M. Cornell, U. Schwertmann, The iron oxides : structure, properties, reactions, occurrences, and uses, Wiley-VCH, Weinheim, 2003.
[74] M. Wilke, G.M. Partzsch, R. Bernhardt, D. Lattard, Determination of the iron oxidation state in basaltic glasses using XANES at the K-edge, Chem Geol, 213 (2004) 71-87.
[75] A.V. Soldatov, D. Lamoen, M.J. Konstantinovic, S. Van den Berghe, A.C. Scheinost, M. Verwerft, Local structure and oxidation state of uranium in some ternary oxides: X-ray absorption analysis, J Solid State Chem, 180 (2007) 54-61.
[76] B. Kosog, H.S. La Pierre, M.A. Denecke, F.W. Heinemann, K. Meyert, Oxidation State Delineation via U L-III-Edge XANES in a Series of Isostructural Uranium Coordination Complexes, Inorg Chem, 51 (2012) 7940-7944.
[77] G.M. Jones, P.L. Arnold, J.B. Love, Oxo-Group-14-Element Bond Formation in Binuclear Uranium(V) Pacman Complexes, Chem-Eur J, 19 (2013) 10287-10294.
[78] Y. Podkovyrina, Pidchenko, I., Pruesmann, T., Bahl., S., Soldatov, A., Vitova, T., Probing covalency in UO3 polymorphs by U M4 edge HR-XANES, in: 16th International Conference on X-ray Absorption Fine Structure Karlsruhe, Germany, 2016.
[79] L. Krall, B. Sandstrom, E.L. Tullborg, L.Z. Evins, Natural uranium in Forsmark, Sweden: The solid phase, Appl Geochem, 59 (2015) 178-188.
[80] J. Suksi, K. Rasilainen, P. Pitkanen, Variations in U-234/U-238 activity ratios in groundwater - A key to flow system characterisation?, Phys Chem Earth, 31 (2006) 556-571.
[81] J.H. Jang, B.A. Dempsey, W.D. Burgos, Solubility of schoepite: Comparison and selection of complexation constants for U(VI), Water Res, 40 (2006) 2738-2746.
[82] K. Muller, V. Brendler, H. Foerstendorf, Aqueous Uranium(VI) Hydrolysis Species Characterized by Attenuated Total Reflection Fourier-Transform Infrared Spectroscopy, Inorg Chem, 47 (2008) 10127-10134.
[83] C. Hennig, Evidence for double-electron excitations in the L-3-edge x-ray absorption spectra of actinides, Phys Rev B, 75 (2007).
[84] S.D. Conradson, D. Manara, F. Wastin, D.L. Clark, G.H. Lander, L.A. Morales, J. Rebizant, V.V. Rondinella, Local structure and charge distribution in the UO2-U4O9 system, Inorg Chem, 43 (2004) 6922-6935.
[85] Y. Suzuki, S.D. Kelly, K.M. Kemner, J.F. Banfield, Radionuclide contamination - Nanometre-size products of uranium bioreduction, Nature, 419 (2002) 134-134.
[86] S. Van den Berghe, J.P. Laval, M. Verwerft, B. Gaudreau, E. Suard, Study of the pyrochlore-related structure of α-Cs2U4O12 by powder neutron and X-ray diffraction, Solid State Sci, 4 (2002) 1257-1264.

[87] C. Fillaux, J.C. Berthet, S.D. Conradson, P. Guilbaud, D. Guillaumont, C. Hennig, P. Moisy, J. Roques, E. Simoni, D.K. Shuh, T. Tyliszczak, I. Castro-Rodriguez, C. Den Auwer, Combining theoretical chemistry and XANES multi-edge experiments to probe actinide valence states, Cr Chim, 10 (2007) 859-871.
[88] J. Bruno, P. Oy, Deep Groundwater Redox Reactions in the Palmottu Uranium Deposit: The Role of Uranium and Iron in These Processes, Posiva Oy, 1996.
[89] R.M. Cornell, U. Schwertmann, The Iron Oxides: Structure, Properties, Reactions, Occurrences and Uses, Wiley, 2003.
[90] N. Belai, M. Frisch, E.S. Ilton, B. Ravel, C.L. Cahill, Pentavalent Uranium Oxide via Reduction of [UO2](2+) Under Hydrothermal Reaction Conditions, Inorg Chem, 47 (2008) 10135-10140.
[91] J.P. Jolivet, P. Belleville, E. Tronc, J. Livage, Influence of Fe(Ii) on the Formation of the Spinel Iron-Oxide in Alkaline-Medium, Clay Clay Miner, 40 (1992) 531-539.
[92] C.A. Gorski, R.M. Handler, B.L. Beard, T. Pasakarnis, C.M. Johnson, M.M. Scherer, Fe Atom Exchange between Aqueous Fe2+ and Magnetite, Environ Sci Technol, 46 (2012) 12399-12407.
[93] P.C. Burns, R.C. Ewing, A. Navrotsky, Nuclear Fuel in a Reactor Accident, Science, 335 (2012) 1184-1188.
[94] M. Maloubier, P.L. Solari, P. Moisy, M. Monfort, C. Den Auwer, C. Moulin, XAS and TRLIF spectroscopy of uranium and neptunium in seawater, Dalton T, 44 (2015) 5417-5427.
[95] P.C. Burns, R.J. Finch, Wyartite: Crystallographic evidence for the first pentavalent-uranium mineral, Am Mineral, 84 (1999) 1456-1460.
[96] C. Boisson, J.C. Berthet, M. Lance, M. Nierlich, J. Vigner, M. Ephritikhine, Synthesis of Organouranium(V) Compounds by Oxidation of Neutral Tetravalent Precursors - Crystal-Structures of [U(Eta-C(5)Me(5))(Nme(2))(3)(Oc4h8][Bph(4)] and [U(Eta-C(5)Me(5))(2)(Net(2))(2)][Bph(4)], the First Cationic Uranium(V) Complexes, J Chem Soc Chem Comm, (1995) 543-544.
[97] A. Ikeda, C. Hennig, S. Tsushima, K. Takao, Y. Ikeda, A.C. Scheinost, G. Bernhard, Comparative study of uranyl(VI) and -(V) carbonato complexes in an aqueous solution, Inorg Chem, 46 (2007) 4212-4219.
[98] T.I. Docrat, J.F.W. Mosselmans, J.M. Charnock, M.W. Whiteley, D. Collison, F.R. Livens, C. Jones, M.J. Edmiston, X-ray absorption spectroscopy of tricarbonatodioxouranate(V), [UO2(CO3)(3)](5-), in aqueous solution, Inorg Chem, 38 (1999) 1879-1882.
[99] D. Cohen, Preparation and Spectrum of Uranium(V) Ions in Aqueous Solutions, J Inorg Nucl Chem, 32 (1970) 3525-&.
[100] D.W. Wester, J.C. Sullivan, Electrochemical and Spectroscopic Studies of Uranium(Iv), Uranium(V), and Uranium(Vi) in Carbonate-Bicarbonate Buffers, Inorg Chem, 19 (1980) 2838-2840.
[101] K. Mizuguchi, Y.Y. Park, H. Tomiyasu, Y. Ikeda, Electrochemical and Spectroelectrochemical Studies on Uranyl Carbonato and Aqua Complexes, J Nucl Sci Technol, 30 (1993) 542-548.

[102] C. Madic, D.E. Hobart, G.M. Begun, Raman Spectrometric Studies of Actinide(V) and Actinide(Vi) Complexes in Aqueous Sodium-Carbonate Solution and of Solid Sodium Actinide(V) Carbonate Compounds, Inorg Chem, 22 (1983) 1494-1503.
[103] P.G. Allen, J.J. Bucher, D.L. Clark, N.M. Edelstein, S.A. Ekberg, J.W. Gohdes, E.A. Hudson, N. Kaltsoyannis, W.W. Lukens, M.P. Neu, P.D. Palmer, T. Reich, D.K. Shuh, C.D. Tait, B.D. Zwick, Multinuclear Nmr, Raman, Exafs, and X-Ray-Diffraction Studies of Uranyl Carbonate Complexes in near-Neutral Aqueous-Solution - X-Ray Structure of [C(Nh2)(3)](6)[(Uo2)(3)(Co3)(6)]Center-Dot-6.5h(2)O, Inorg Chem, 34 (1995) 4797-4807.
[104] E.T. Strom, D.E. Woessner, W.B. Smith, C-13 Nmr-Spectra of the Uranyl Tricarbonate-Bicarbonate System, Abstr Pap Am Chem S, 181 (1981) 222-INOR.
[105] P. Pyykko, J. Li, N. Runeberg, Quasi-Relativistic Pseudopotential Study of Species Isoelectronic to Uranyl and the Equatorial Coordination of Uranyl, J Phys Chem-Us, 98 (1994) 4809-4813.
[106] L. Gagliardi, I. Grenthe, B.O. Roos, Theoretical study of the structure of tricarbonatodioxouranate, Inorg Chem, 40 (2001) 2976-2978.
[107] T.W. Newton, F.B. Baker, A Uranium(V)-Uranium(VI) Complex and Its Effect on the Uranium (V) Disproportionation Rate, Inorg Chem, 4 (1965) 1166-1170.
[108] P.T. Kissinger, W.R. Heineman, Cyclic voltammetry, Journal of Chemical Education, 60 (1983) 702.
[109] M. Wojdyr, Fityk: a general-purpose peak fitting program, J Appl Crystallogr, 43 (2010) 1126-1128.
[110] D.E. Morris, Redox energetics and kinetics of uranyl coordination complexes in aqueous solution, Inorg Chem, 41 (2002) 3542-3547.
[111] G. Meinrath, Uranium(VI) speciation by spectroscopy, J Radioanal Nucl Ch, 224 (1997) 119-126.
[112] K. Mizuoka, S. Tsushima, M. Hasegawa, T. Hoshi, Y. Ikeda, Electronic spectra of pure uranyl(V) complexes: Characteristic absorption bands due to a (UO2+)-O-V core in visible and near-infrared regions, Inorg Chem, 44 (2005) 6211-6218.
[113] E. Rabinowitch, R.L. Belford, Spectroscopy and photochemistry of uranyl compounds, Macmillan, 1964.
[114] R.G. Denning, Electronic-Structure and Bonding in Actinyl Ions, Struct Bond, 79 (1992) 215-276.
[115] L.S. Natrajan, Developments in the photophysics and photochemistry of actinide ions and their coordination compounds, Coordin Chem Rev, 256 (2012) 1583-1603.
[116] P. Brint, Mccaffer.Aj, Electronic-Spectra and Magnetic Circular-Dichroism of Uranyl Ion, Mol Phys, 25 (1973) 311-322.
[117] R.L. Dekock, E.J. Baerends, P.M. Boerrigter, J.G. Snijders, On the Nature of the 1st Excited-States of the Uranyl-Ion, Chem Phys Lett, 105 (1984) 308-316.

[118] R.G. Denning, T.R. Snellgrove, D.R. Woodwark, Electronic-Structure of Uranyl-Ion .1. Electronic-Spectrum of Cs2uo2cl4, Mol Phys, 32 (1976) 419-442.
[119] J. Stöhr, NEXAFS Spectroscopy, Springer, 1992.
[120] K.B. Alberman, J.S. Anderson, Oxyde Des Urans, Angew Chem-Ger Edit, 61 (1949) 416-416.
[121] D.J. Hill, Nuclear energy for the future, Nat Mater, 7 (2008) 680-682.
[122] H.R. Hoekstra, S. Siegel, The Uranium-Oxygen System - U3o8-Uo3, J Inorg Nucl Chem, 18 (1961) 154-165.
[123] I. Zwiebel, Nuclear chemical engineering. (Part of the McGraw-Hill Series in Nuclear Engineering) Manson Benedict, Professor, Nuclear Engineering, M.I.T., and Thomas H. Pigford, Associote Professor, Nuclear Engineering, M.I.T. McGraw Hill Book Company, Inc., New York (1957). 594 pages. $9.50, Aiche J, 4 (1958) 8J-8J.
[124] R.M. Dell, V.J. Wheeler, Chemical Reactivity of Uranium Trioxide .1. Conversion to U3o8, Uo2 and Uf4, T Faraday Soc, 58 (1962) 1590-&.
[125] D. Gorman-Lewis, J.B. Fein, P.C. Burns, J.E.S. Szymanowski, J. Converse, Solubility measurements of the uranyl oxide hydrate phases metaschoepite, compreignacite, Na-compreignacite, becquerelite, and clarkeite, J Chem Thermodyn, 40 (2008) 980-990.
[126] J.J. Rehr, J.J. Kas, M.P. Prange, A.P. Sorini, Y. Takimoto, F. Vila, Ab initio theory and calculations of X-ray spectra, Cr Phys, 10 (2009) 548-559.
[127] P.C. Debets, Structure of Beta-Uo3, Acta Crystallogr, 21 (1966) 589-&.
[128] R. Engmann, P.M.D. Wolff, Crystal Structure of Gamma-U3, Acta Crystallogr, 16 (1963) 993-&.
[129] R. Guillaumont, F.J. Mompean, O.N.E. Agency, Update on the Chemical Thermodynamics of Uranium, Neptunium, Plutonium, Americium and Technetium, Elsevier, 2003.
[130] R.J. Lemire, N.E.A.D. Bank, O.N.E. Agency, Chemical Thermodynamics of Neptunium and Plutonium, Elsevier, 2001.
[131] F.J. Mompean, M. Illemassène, J. Perrone, Chemical Thermodynamics of Compounds and Complexes of U, Np, Pu, Am, Tc, Se, Ni and Zr With Selected Organic Ligands, Elsevier Science, 2005.
[132] J.J. Roy, L.F. Grantham, D.L. Grimmett, S.P. Fusselman, C.L. Krueger, T.S. Storvick, T. Inoue, Y. Sakamura, N. Takahashi, Thermodynamic properties of U, Np, Pu, and Am in molten LiCl-KCl eutectic and liquid cadmium, J Electrochem Soc, 143 (1996) 2487-2492.
[133] J.M. Haschke, T.H. Allen, L.A. Morales, Reaction of plutonium dioxide with water: Formation and properties of PuO2+x, Science, 287 (2000) 285-287.
[134] P.A. Korzhavyi, L. Vitos, D.A. Andersson, B. Johansson, Oxidation of plutonium dioxide, Nat Mater, 3 (2004) 225-228.
[135] B. Ravel, M. Newville, ATHENA and ARTEMIS: Interactive graphical data analysis using IFEFFIT, Phys Scripta, T115 (2005) 1007-1010.

[136] M.H. Lee, Y.J. Park, W.H. Kim, Absorption spectroscopic properties for Pu (III, IV and VI) in nitric and hydrochloric acid media, J Radioanal Nucl Ch, 273 (2007) 375-382.
[137] C. Den Auwer, E. Simoni, S. Conradson, C. Madic, Investigating actinyl oxo cations by X-ray absorption spectroscopy, Eur J Inorg Chem, (2003) 3843-3859.
[138] S.D. Conradson, B.D. Begg, D.L. Clark, C. Den Auwer, F.J. Espinosa-Faller, P.L. Gordon, N.J. Hess, R. Hess, D.W. Keogh, L.A. Morales, M.P. Neu, W. Runde, C.D. Tait, D.K. Veirs, P.M. Villella, Speciation and unusual reactivity in PuO2+x, Inorg Chem, 42 (2003) 3715-3717.
[139] R.G. Denning, Electronic structure and bonding in actinyl ions and their analogs, J Phys Chem A, 111 (2007) 4125-4143.

Appendix

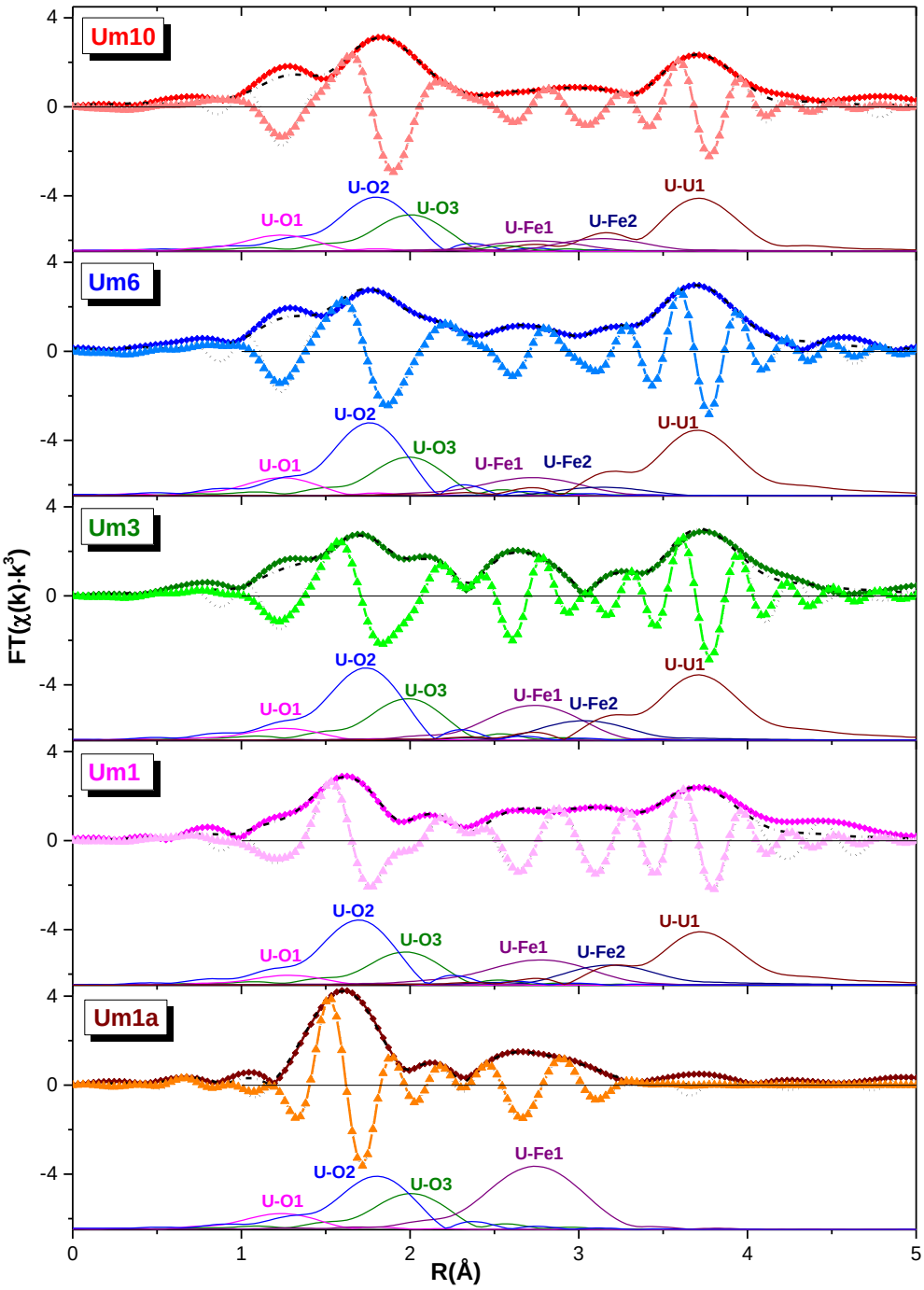

Figure AI.1. R-space fit results for the Um10, Um6, Um3, Um1 and Um1a samples; magnitude of the FT-EXAFS (colored rhombs) and their best fits (black dash dot line); imaginary parts of the FT-EXAFS (light colored triangles) and their best fits (black dash line). The magnitudes of the FT-EXAFS fits for the different shells are shown vertically shifted.

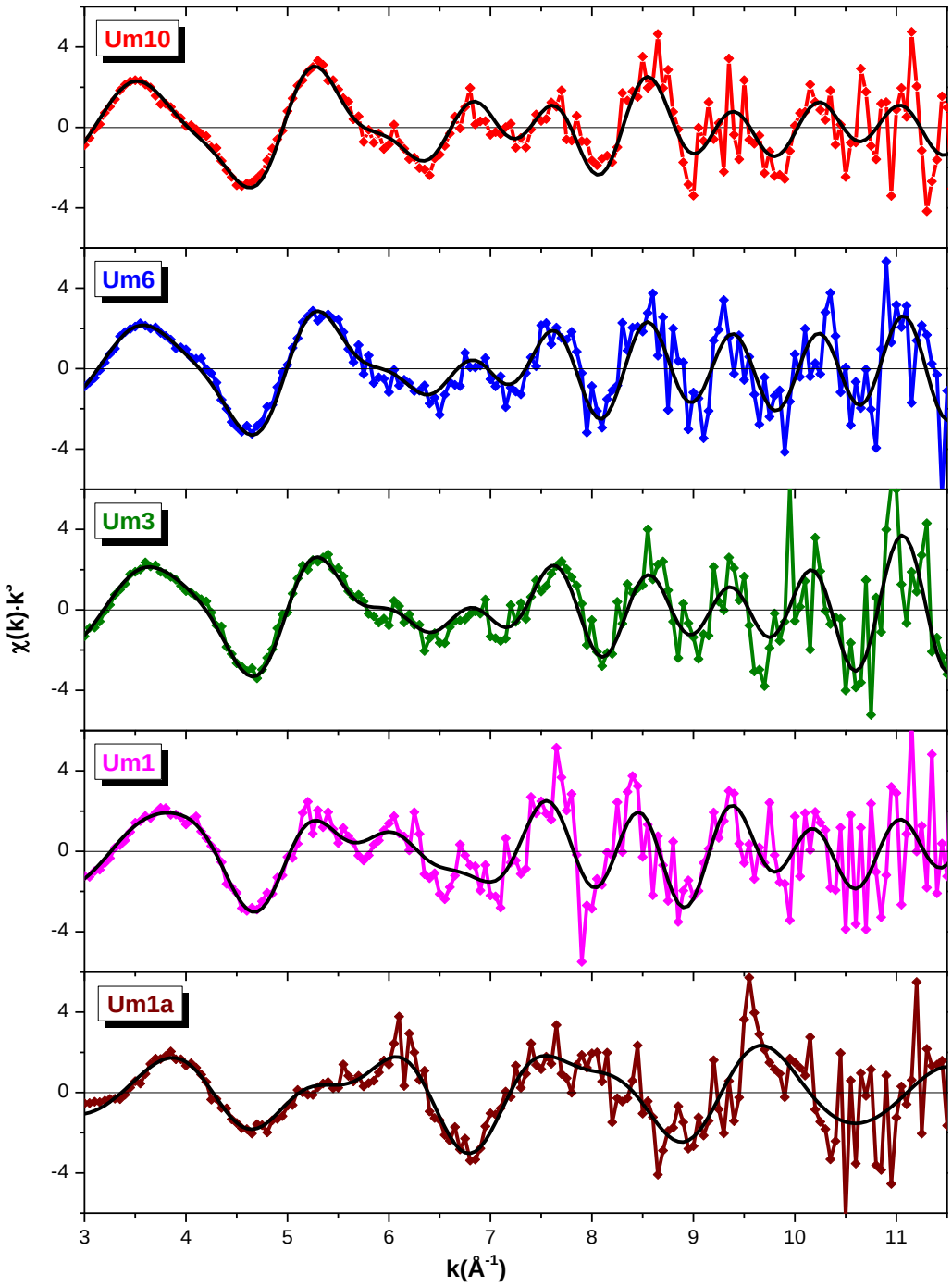

Figure AI.2. k^3-weighted filtered $\chi(k)$ for the Um10, Um6, Um3, Um1, and Um1a samples (colored rhombs) and their best fits (black solid line).

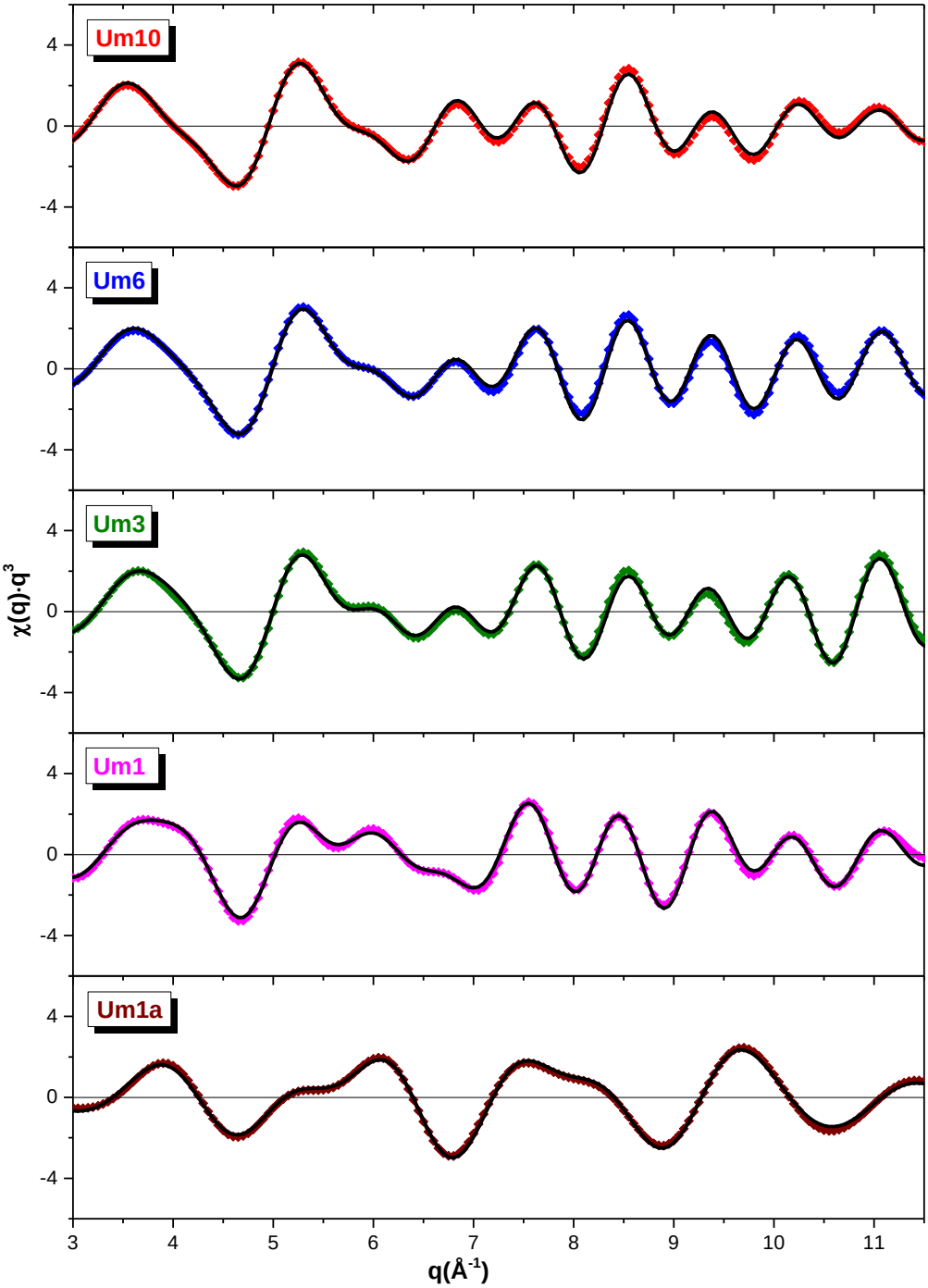

Figure AI.3. Back-transformed EXAFS for the Um10, Um6, Um3, Um1 and Um1a samples (colored rhombs) and their best fits (black solid line).

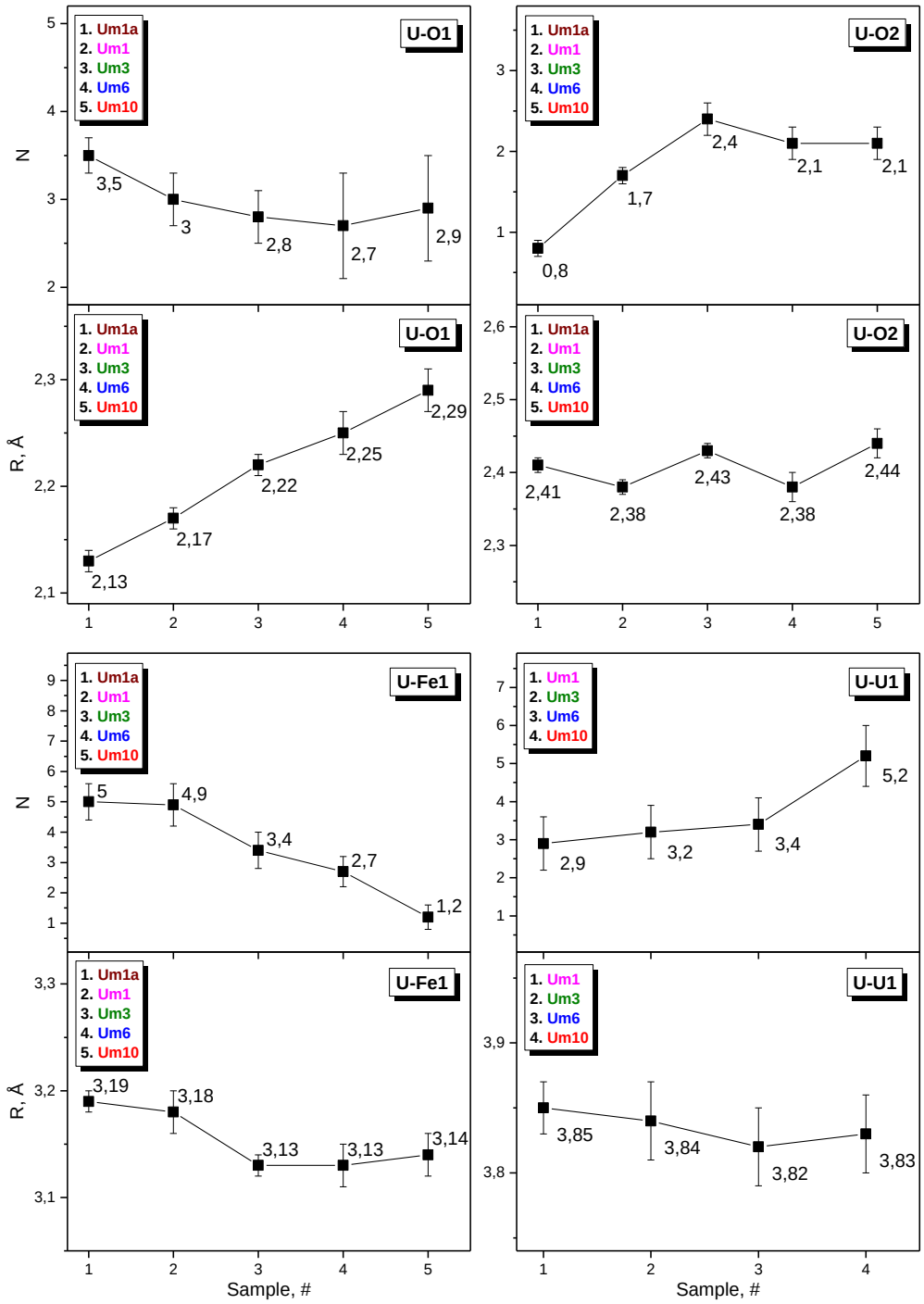

Figure AI.4. N and R values for U-O1, U-O2, U-Fe1 and U-U1 shells found from the best EXAFS fits for the Um10, Um6, Um3, Um1 and Um1a samples.

Table AII.1. FEFF9.6 input files for calculations of U M_4 edge XANES spectra of α-UO_3, β-UO_3, γ-UO_3 and UO_2.

```
TITLE Uranium(VI) oxide-alpha

CONTROL 1 1 1 1 1 1
PRINT 1 0 0 0 0 0
EDGE M4
S02 1.0
COREHOLE FSR
XANES 6 0.05 0.3
FMS 7 0
LDOS -20 20 0.2
SCF 3.7 0 30 0.05 10
UNFREEZEF
EXCHANGE 0 0 -2.5 -1
POTENTIALS
0 92 U
1 92 U
2 8 O
```

```
TITLE Uranium(VI) oxide-beta

CONTROL 1 1 1 1 1 1
PRINT 1 0 0 0 0 0
EDGE M4
S02 1.0
COREHOLE FSR
XANES 5 0.05 0.3
FMS 10 0
LDOS -20 20 0.2
SCF 7 0 100 0.05 10
UNFREEZEF
EXCHANGE 0 0 -2 -1
POTENTIALS
0 92 U
1 92 U
2 8 O
```

```
TITLE Uranium(VI) oxide-gamma

CONTROL 1 1 1 1 1 1
PRINT 1 0 0 0 0 0
EDGE M4
S02 1.0
COREHOLE FSR
LDOS -20 20 0.2
SCF 7 0 100 0.05 10
UNFREEZEF
EXCHANGE 0 0.5 -2 -1
XANES 5 0.05 0.3
FMS 10 0
POTENTIALS
0 92 U
1 92 U
2 8 O
```

```
TITLE Uranium(IV) dioxide

CONTROL 1 1 1 1 1 1
PRINT 1 0 0 0 0 0
EDGE M4
S02 1.0
COREHOLE FSR
LDOS -15 5 0.2
SCF 7.0 0 100 0.05 10
UNFREEZEF
EXCHANGE 0 0.5 -2 -1
XANES 5.0 0.05 0.3
FMS 10 0
POTENTIALS
0 92 U
1 92 U
2 8 O
```

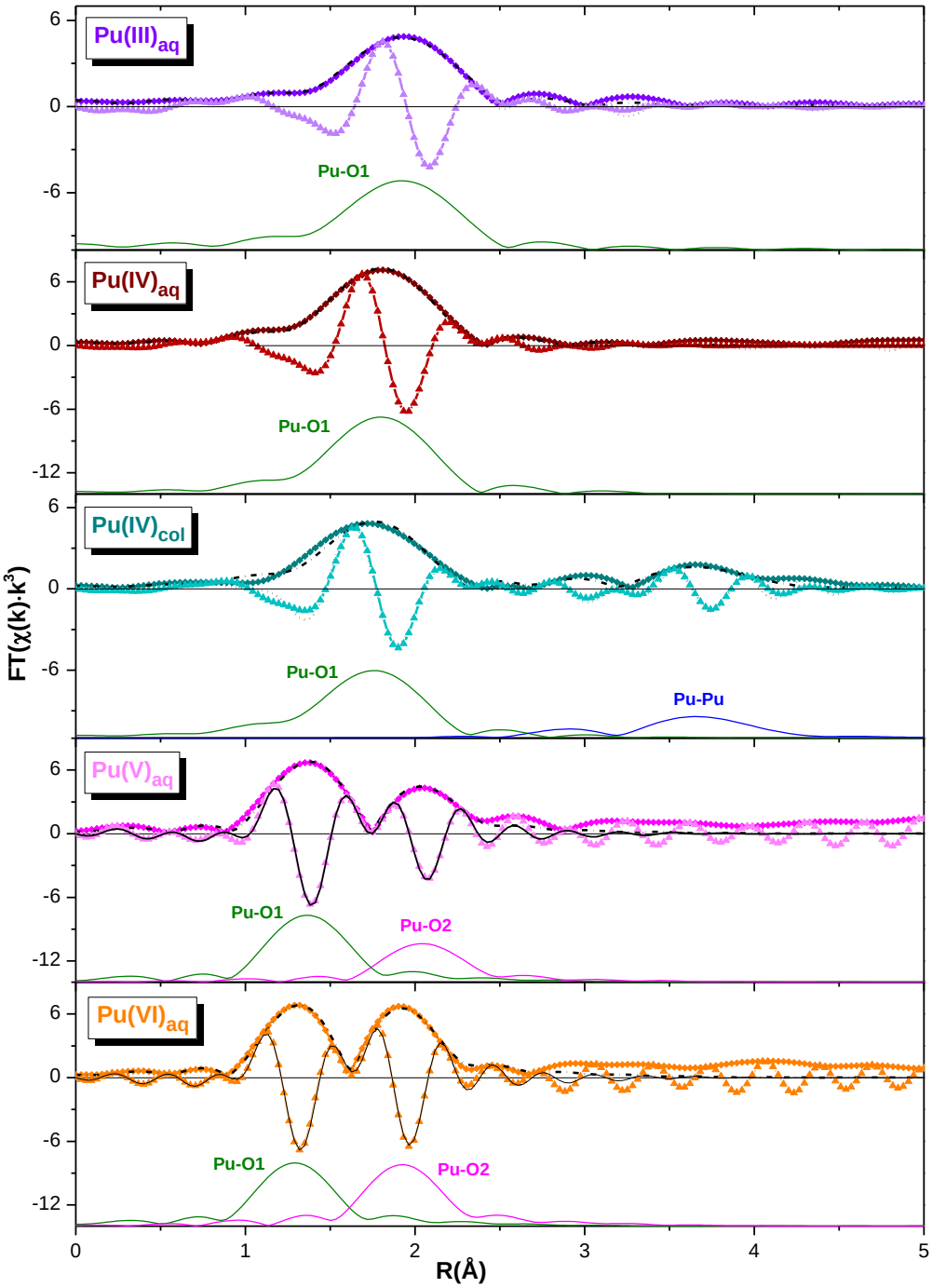

Figure AIII.1. R-space fit results for the $Pu(III)_{aq}$, $Pu(IV)_{aq}$, $Pu(IV)_{col}$, $Pu(V)_{aq}$ and $Pu(VI)_{aq}$ species; magnitude of the FT-EXAFS (colored rhombs) and their best fits (black dash dot line); imaginary parts of the FT-EXAFS (light colored triangles) and their best fits (black dash line).

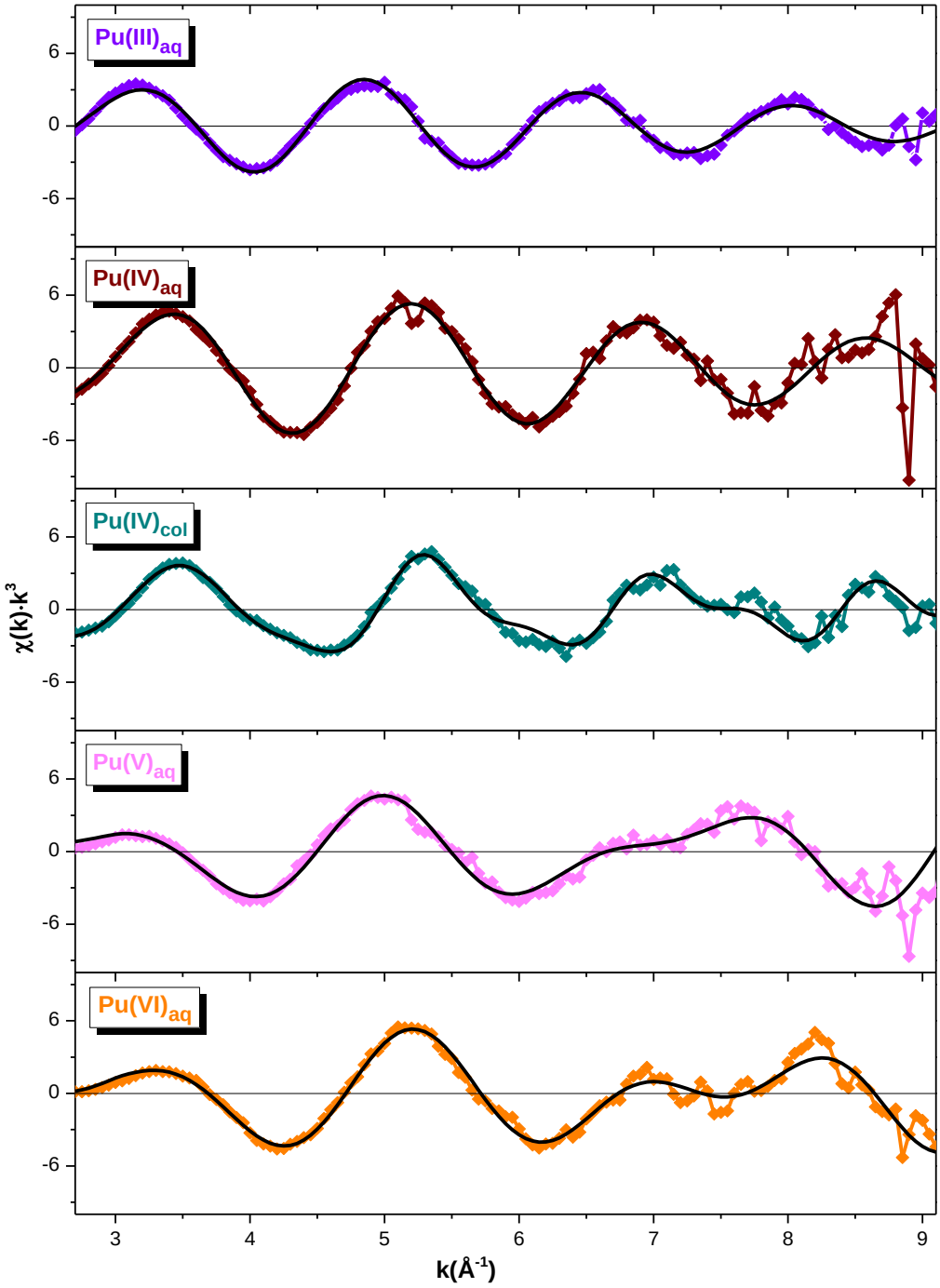

Figure AIII.2. k^3-weighted filtered $\chi(k)$-functions of the $Pu(III)_{aq}$, $Pu(IV)_{aq}$, $Pu(IV)_{col}$, $Pu(V)_{aq}$ and $Pu(VI)_{aq}$ (colored rhombs) and their best fits (black solid line).

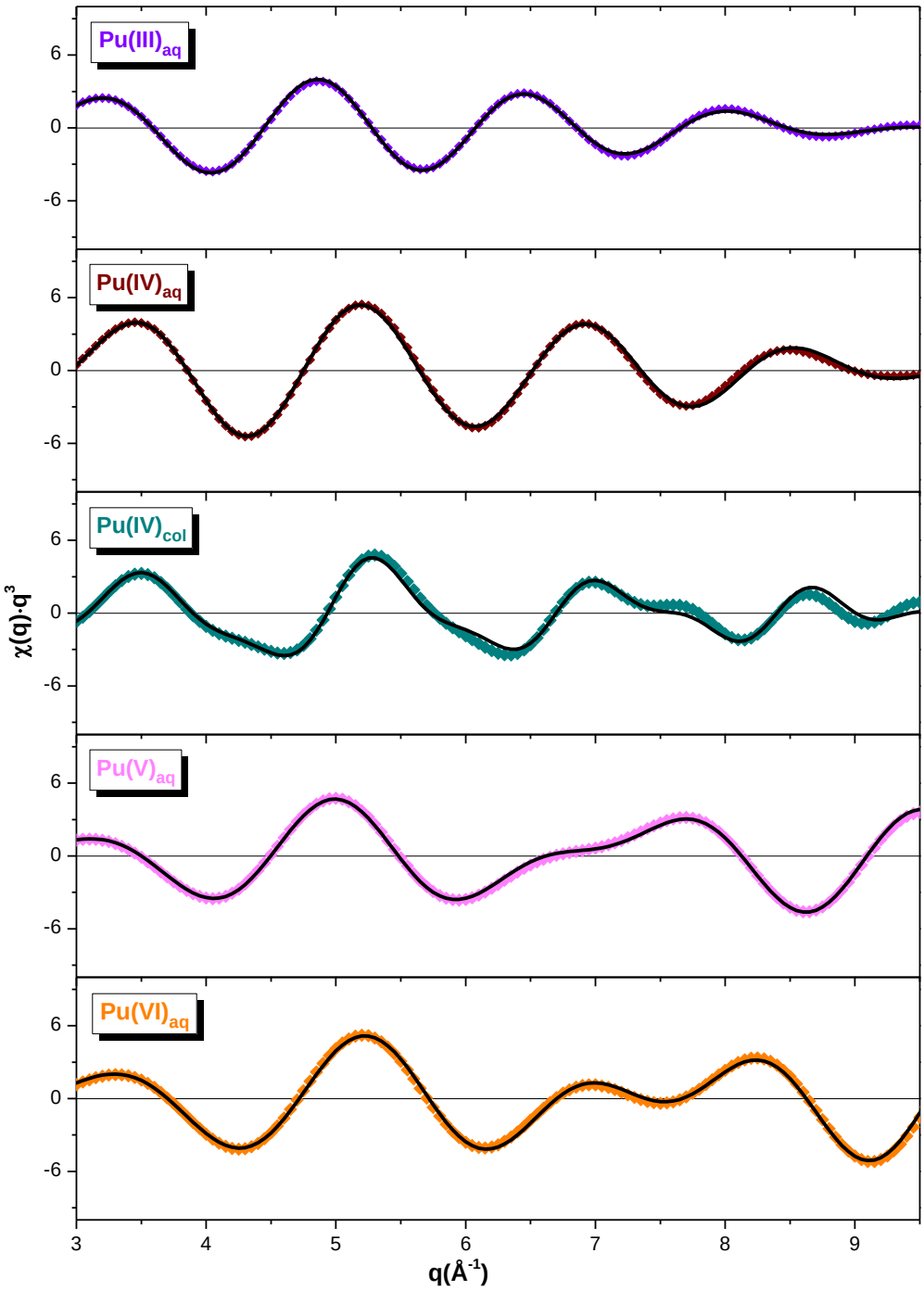

Figure AIII.3. Back-transformed EXAFS for the $Pu(III)_{aq}$, $Pu(IV)_{aq}$, $Pu(IV)_{col}$, $Pu(V)_{aq}$ and $Pu(VI)_{aq}$ and their back-transformed fits.

List of Tables and Figures

Table/ Figure	Content	pp
Table 2.2.1	Emission energies, analyzer crystals and corresponding Bragg angles used in the U and Pu	**15**
Table 4.1.1	U and Fe concentrations, pH, E_h and Ionic strength (I[NaCl])	**27**
Table 4.1.2	Descriptions of the samples and lists of the applied characterization techniques	**31**
Table 4.1.3	EXAFS fit results for the Um10, Um6, Um3, Um1 and Um1a samples	**41**
Table 4.2.1	Name of samples and spectra, contact time of U with magnetite, amount of U removed by magnetite and maghemite for suspension containing [U]=$3\cdot10^{-5}$ M and [NaCl]=0.01 M, pH, E_h values and applied spectroscopy techniques	**53**
Table 4.2.2	Energy positions of the spectral peaks	**58**
Table 5.1.1	Energy positions and areas of the peaks for the U M_4 edge HR-XANES spectra of $[U^{VI}O_2(CO_3)_3]^{4-}$ and $[U^{V}O_2(CO_3)_3]^{5-}$	**80**
Table 5.2.1	Crystallographic data used for calculations of the U M_4 edge HR-XANES spectra	**84**
Table 5.2.2	Average U-O bond lengths for α-UO_3, β-UO_3, γ-UO_3, $UO_3\cdot1\text{-}2H_2O$ and CaU_2O_7	**87**
Table 5.3.1	Input parameters for Pu L_3 edge XANES FEFF9.5 calculations; * self-consistent field (SCF): controls FEFF's automated self-consistent potential calculations; ** when it is not used the f electron density is fixed at the atomic value in order to obtain well converged SCF potentials; *** used to customize the energy grid	**94**
Table 5.3.2	Energy positions of spectral features for the $Pu(III)_{aq}$, $Pu(IV)_{aq}$, $Pu(IV)_{col}$, $Pu(V)_{aq}$ and $Pu(VI)_{aq}$ for Pu L_3 and M_5 edge HR-XANES spectra.	**97**
Table 5.3.3	EXAFS fit results for $Pu(III)_{aq}$, $Pu(IV)_{aq}$, $Pu(IV)_{col}$, $Pu(V)_{aq}$ and $Pu(VI)_{aq}$	**101**
Table AII.1	FEFF9.6 input files for calculations of U M_4 edge XANES spectra of α-UO_3, β-UO_3, γ-UO_3 and UO_2	**125**

Figure 1.1	Schematic view of a potential nuclear waste repository including different barriers and an example of a corrosion process, which takes place by interaction of ground water with the storage container and the waste; a simplified list of final repositories in different type of geological formations considered by different countries is also included	**1**
Figure 2.1.1	The XAFS spectrum of UO_2; the U absorption edge energy (E_0), the XANES and the EXAFS regions are marked	**7**
Figure 2.2.1	Radial extent of Pu 5*f* valence electrons. The radial probability *P(R)* of finding electron at a distance *R* from nucleus is shown for the valence 5*f*, 6*d*, 7*s* and 7*p* orbitals for Pu(III)	**11**
Figure 2.2.2	Schematic electron excitations and emission transitions for *An* L_3 and $M_{4,5}$ edges	**12**
Figure 2.2.3	U L_3 (a) and M_4 (b) edges conventional and HR-XANES spectra of $Cs_2(UO_2)Cl_4$ and $UO_3 \cdot 1\text{-}2H_2O$ (meta-schoepite), respectively	**12**
Figure 2.2.4	U 3*d*4*f* RIXS map of U(VI) in 1 M $HClO_4$ aqueous solution	**13**
Figure 2.2.5	Schematic representation of RIXS processes for *An*	**13**
Figure 2.2.6	Emission energies and the corresponding analyzer crystals and Bragg angles for *An* M_β/M_α (a) and *An* $L_{\alpha 1}$ (b) emission lines for *An* Z=90-96	**14**
Figure 3.1.1	3*D* graphical layout of the INE-Beamline for *An* XAS measurements	**16**
Figure 3.2.1	A photograph of the MAC-Spectrometer installed at the INE-Beamline (right). A scheme of the Rowland circle geometry (top left). A He glovebox and the transfer chamber for the samples (left bottom)	**19**
Figure 4.1.1	Design of the sample holder used for the U M_4 edge HR-XANES experiments at ESRF	**30**
Figure 4.1.2	Schematic representation of formation of magnetite through continuous recrystallization of Fe oxy-(hydr)oxide species and possible U interaction mechanisms with these species	**32**
Figure 4.1.3	Fe *Pourbaix* diagram for Um1, Um3, Um6 and Um10. Symbols correspond to experimental pH and E_h measurements for Um1-Um10 samples with 1000 $\leq [U]_{tot}$ [ppm] $\leq$ 10000	**33**
Figure 4.1.4	SEM image of Um10 (100 nm scale). An octahedrally shaped magnetite particle is circled	**33**
Figure 4.1.5	Crystalline XRD patterns for the 10 days aged Um10 sample (top; laboratory based measurements) and for the 480 days aged Um10, Um6, Um3, Um1 as well as Um1a samples	**34**
Figure 4.1.6	Fe $2p_{3/2}$ XPS spectra for Um10-Um1 samples aged for 210 days (a) and for Um6 aged for 10 and 310 days (b)	**35**
Figure 4.1.7	Fe K edge HR-XANES (a) and Fe $K_{\beta 1,3}$ X-ray emission (b) spectra of FeO, FeO(OH), Fe_3O_4 and Um6	**35**

Figure 4.1.8	U M_4 edge HR-XANES spectra of the U_4O_9, Um1, Um3, Um6, Um10 and Umh samples shifted along the *y*-axis (a) and of the Um1, Um3, Um6, Um10 and Umh samples plotted without a shift along the *y*-axis (b)	**36**
Figure 4.1.9	General schematic overview of the methods' sensitivity for speciation of *An*. $M_{4,5}$ edge XANES has a great potential for *An* speciation at much lower concentrations	**37**
Figure 4.1.10	U L_3 edge XANES spectra of po-mag42 [30], Um1a, Um1, Um3, Um6, Um10 (aged 147 days), Um1a (aged 373 days), Umh (aged 330 days), and UO_2 (a): U L_3 edge HR-XANES spectra of Um1, Um3, Um6, Um10 (aged 10 days), Umh (aged 55 days) and UO_2 (b)	**39**
Figure 4.1.11	Magnitude of FT-EXAFS data (colored rhombs) and best fits for the Um10, Um6, Um3, Um1 (a) and Um1a, Um1 (b) samples	**40**
Figure 4.1.12	HR-TEM image of Um1 (aged 330 days)	**43**
Figure 4.1.13	U M_4 edge HR-XANES spectra of Um1, Um1a and Umh	**45**
Figure 4.2.1	SEM image of magnetite	**52**
Figure 4.2.2	XRD patterns of magnetite (a) and maghemite (b) nanoparticles. The most intensive peak has a shift characteristic for the structure of maghemite	**53**
Figure 4.2.3	U *Pourbaix* diagram. The symbols correspond to experimental pH and E_h measurements for the Um175f, Um175 and Umh samples ($[U]_{tot} = 3\cdot10^{-5}$ M and I[NaCl] = 0.01 M)	**53**
Figure 4.2.4	U 4*f* XPS spectrum of Um175f (violet) and its best fit (black) (a). Spectral features characteristic for U(V) and U(VI) are shown with green and red lines, respectively. U 4*f* XPS spectra of Um175f and Um175 (b). Fe 2*p* XPS spectra of stoichiometric Fe_3O_4, Um175f, Um175 and γ-Fe_2O_3 (c)	**55**
Figure 4.2.5	U M_4 (a, b) and U L_3 (a', b') edge HR-XANES spectra of U_4O_9 (black), Um175f (violet), Um175 (magenta) and Umh (marine-blue)	**58**
Figure 5.1.1	The entire electromagnetic spectrum and used *in-situ* techniques used for molecular and atomic characterization of U species	**63**
Figure 5.1.2	Basic principle of three-electrode bulk electrochemical cell setup and operation	**67**
Figure 5.1.3	3*D* model of *in-situ* spectroelectrochemical cell, including three electrode system	**70**
Figure 5.1.4	Picture of the *in-situ* spectroelectrochemical cell installed at the INE-Beamline inside the He glovebox	**71**
Figure 5.1.5	Cyclic voltamogramms of U tricarbonato complexes measured with scan rate of 10 mV/sec for Hg/HgO (a) and Ag/AgCl (b) reference electrodes	**73**
Figure 5.1.6	Decrease of the current density during U(VI) reduction to U(V) in 1.5 M Na_2CO_3 aqueous solution. Complete U(VI) reduction is achieved within 2 hours for the used electrochemical setup	**74**

Figure 5.1.7	*In-situ* measured UV-Vis spectra of U(VI) (orange), 50% reduced U(VI) (magenta), bulk U(V) (brown and violet) tricarbonate complexes measured within 800 minutes of measuring time	**75**
Figure 5.1.8	3*d4f* RIXS maps of $[U^{VI}O_2(CO_3)_3]^{4-}$ (a) and $[U^{V}O_2(CO_3)_3]^{5-}$ (b)	**77**
Figure 5.1.9	U M_4 edge HR-XANES spectra of $[U^{VI}O_2(CO_3)_3]^{4-}$ (a) and $[U^{V}O_2(CO_3)_3]^{5-}$ (b)	**77**
Figure 5.1.10	Measured (red) and best model (black dotted) spectra of the normalized U M_4 edge HR-XANES spectra of $[U^{VI}O_2(CO_3)_3]^{4-}$ (a) and $[U^{V}O_2(CO_3)_3]^{5-}$ (b)	**79**
Figure 5.2.1	Description of formation routes of α-UO_3, β-UO_3, γ-UO_3 and $UO_3 \cdot 1\text{-}2H_2O$ synthesized from $UO_2(NO_3)_2 \cdot 6H_2O$	**85**
Figure 5.2.2	Powder XRD patterns of α-UO_3, β-UO_3, γ-UO_3 polymorphs (SUL-BL) and $UO_3 \cdot 1\text{-}2H_2O$ (Brucker Diffr.) together with XRD patterns published in the ICSD database (Table 5.2.1). XRD of CaU_2O_7 is not available.	**85**
Figure 5.2.3	U M_4 edge HR-XANES spectra of $UO_3 \cdot 1\text{-}2H_2O$, γ-$UO_3$, β-$UO_3$, α-$UO_3$, and CaU_2O_7, (a), experimental and theoretical spectra for α-UO_3 (b), β-UO_3 (c) and γ-UO_3 (d) phases	**86**
Figure 5.2.4	Standard molar Gibbs energies of formation of UO_{2+x} as a function of x	**89**
Figure 5.3.1	Vis-NIR spectra of $Pu(III)_{aq}$ (a), $Pu(IV)_{aq}$ (b, bottom), $Pu(IV)_{col}$ (b, top), $Pu(V)_{aq}$ (c) and $Pu(VI)_{aq}$ (d) before (coloured curve) and after (black dashed curve) the experiments	**95**
Figure 5.3.2	Pu L_3 edge conventional (a) and HR-XANES (b) of $Pu(III)_{aq}$, $Pu(IV)_{aq}$, $Pu(IV)_{col}$, $Pu(V)_{aq}$ and $Pu(VI)_{aq}$	**96**
Figure 5.3.3	Pu L_3 edge HR-XANES spectra, FEFF9.5 calculations of HR-XANES spectra and *d*- and *f*-DOS of aqueous $Pu(III)_{aq}$ (a), $Pu(IV)_{aq}$ (b), $Pu(IV)_{col}$ (c), $Pu(V)_{aq}$ (d) and $Pu(VI)_{aq}$ (e)	**98**
Figure 5.3.4	R-space fit results for $Pu(III)_{aq}$, $Pu(IV)_{aq}$, $Pu(IV)_{col}$, $Pu(V)_{aq}$ and $Pu(VI)_{aq}$ Fourier transformed magnitude of EXAFS data (colored rhombs) and their best fits (dash dot line). The arrow indicated Pu-Pu coordination peak in $Pu(IV)_{col}$	**100**
Figure 5.3.5	3*D* design (top) and a photograph (bottom left) of the *An* $M_{4,5}$ edge HR-XANES liquid cell (top). In the first version of the cell 10 µm PP has been used as a window material; as a result the colour of the Pu oxidation states can be distinguished and correlate well with the colours of the laboratory prepared Pu oxidation states (photograph bottom right) used for the Pu M_5 edge HR-XANES/RIXS measurements	**102**
Figure 5.3.6	Pu M_5 edge conventional (black dashed curves) and HR (coloured curves) XANES spectra of $Pu(III)_{aq}$ (a), $Pu(IV)_{col}$ (b), $Pu(IV)_{aq}$ (c), and $Pu(VI)_{aq}$ (d)	**103**
Figure 5.3.7	3*d4f* RIXS maps of $Pu(III)_{aq}$ (a), $Pu(IV)_{col}$ (b), $Pu(IV)_{aq}$ (c), and $Pu(VI)_{aq}$ (d)	**103**
Figure 5.3.8	Pu M_5 edge HR-XANES spectra of $Pu(IV)_{col}$ and $[Pu(IV)_{aq} + 6\ \%\ Pu(VI)_{aq}]$. Peak B is enlarged in the inset	**105**

Figure AI.1	R-space fit results for the Um10, Um6, Um3, Um1 and Um1a samples; magnitude of the FT-EXAFS (colored rhombs) and their best fits (black dash dot line); imaginary parts of the FT-EXAFS (light colored triangles) and their best fits (black dash line)	**121**
Figure AI.2	k^3-weighted filtered $\chi(k)$ for the Um10, Um6, Um3, Um1, and Um1a samples (colored rhombs) and their best fits (black solid line)	**122**
Figure AI.3	Back-transformed EXAFS for the Um10, Um6, Um3, Um1 and Um1a samples (colored rhombs) and their best fits (black solid line)	**123**
Figure AI.4	N and R values for U-O1, U-O2, U-Fe1 and U-U1 shells found from the best EXAFS fits for the Um10, Um6, Um3, Um1 and Um1a samples	**124**
Figure AIII.1	R-space fit results for the $Pu(III)_{aq}$, $Pu(IV)_{aq}$, $Pu(IV)_{col}$, $Pu(V)_{aq}$ and $Pu(VI)_{aq}$ species; magnitude of the FT-EXAFS (colored rhombs) and their best fits (black dash dot line); imaginary parts of the FT-EXAFS (light colored triangles) and their best fits (black dash line)	**126**
Figure AIII.2	k^3-weighted filtered $\chi(k)$-functions of the $Pu(III)_{aq}$, $Pu(IV)_{aq}$, $Pu(IV)_{col}$, $Pu(V)_{aq}$ and $Pu(VI)_{aq}$ (colored rhombs) and their best fits (black solid line)	**127**
Figure AIII.3	Back-transformed EXAFS for the $Pu(III)_{aq}$, $Pu(IV)_{aq}$, $Pu(IV)_{col}$, $Pu(V)_{aq}$ and $Pu(VI)_{aq}$ and their back-transformed fits	**128**

List of Symbols and Abbreviations

α	Alpha
β	Beta
γ	Gamma
%	Percent
Å	Angstrom
An	Actinide
Ar	Argon
CO_2	Carbon dioxide
°C	Celsius degree
Fe	Iron
He	Helium
O_2	Oxygen
Pu	Plutonium
S	Sulphur
U	Uranium
E_a	Anodic potential
E_c	Cathodic potential
ΔE_p	Difference between anodic and cathodic potentials
E_o	Absorption edge energy
ΔE_o	Energy shift
i	Current
ħ	Planck's constant
k	Photoelectron's wavenumber
N	Coordination number
R	Interatomic distance
r	Goodness of fit parameter
α-Fe_2O_3	Hematite
FeO(OH)	Goethite/Ferrihydrite
γ-Fe_2O_3	Maghemite
Fe_3O_4	Magnetite
AMCSD	American mineralogist crystal structure database
ANKA	Angströmquelle Karlsruhe
ARTEMIS	Interactive program for XAFS fitting
ATHENA	Interactive program for XAFS analysis
CV	Cyclic voltammetry
DCM	Double crystal monochromator
DFT	Density functional theory
DOS	Density of states
DW	Debye-Waller factor
ESRF	European Synchrotron Radiation Facility
EXAFS	Extended X-Ray absorption fine structure
FEFF	Computer program for quantum-chemical calculations
FIT2D	Computer program for XRD spectra analysis
FITYK	Computer program for spectra analysis and modelling
FWHM	Full width half maximum
HOMO	Highest occupied molecular orbital
HR-XANES	High-resolution X-ray absorption near edge structure
ICSD	Inorganic crystal structure database

IFEFFIT	Suite of interactive programs for XAFS analysis
INE	Institute for Nuclear Waste Disposal
LUMO	Lowest unoccupied molecular orbital
MO	Molecular orbitals
MS	Multiple scattering
NWR	Nuclear waste repository
RIXS	Resonant inelastic X-ray scattering
SCF	Self-consistent field
SDD	Silicon drift diode
SEM	Scanning electron microscopy
SNF	Spent nuclear fuel
SP	Scattering path
TEM	Transmission electron microscopy
UV-Vis	Ultraviolet-visible
Vis-NIR	Visible-near infrared
WL	White line
XAFS	X-ray absorption fine structure
XANES	X-ray absorption near edge structure
XAS	X-ray absorption spectoscopy
XES	X-ray emission spectoscopy
XPS	X-ray photoelectron spectroscopy
XRD	X-ray diffraction

List of Publications and Contributions

Peer reviewed articles

R. Bohler, M.J. Wellanda, D. Prieur, P. Cakir, T. Vitova, T. Pruessmann, I. Pidchenko, C. Hennig, C. Guéneaud, J.M. Konings, D. Manara,
"Recent advances in the study of the UO_2-PuO_2 phase diagram at high temperatures",
Journal of Nuclear Materials **2014**, 448(1-3): 330-339.

I. Pidchenko, S. Salminen-Paatero, J. Rothe, J. Suksi,
"Study of uranium oxidation states in geological material",
Journal of Environmental Radioactivity **2013**, 124: 141-146,

Articles accepted for publication

I. Pidchenko, F. Heberling, K.O. Kvashnina, N. Finck, D. E. Bohnert T. Schäfer, J. Rothe, H. Geckeis, T. Vitova,
"Aqueous U(VI) interaction with magnetite nanoparticles in a mixed flow reactor system: HR-XANES study",
Journal of Physics: Conference Series, **2015**, (accepted)

Y. Podkovyrina, I. Pidchenko, T. Prüßmann, S. Bahl, A. Soldatov, T. Vitova,
"Probing covalency in the UO_3 polymorphs by U M_4 edge HR-XANES",
Journal of Physics: Conference Series, **2015**, (accepted)

Articles in preparation

I. Pidchenko, K.O. Kvashnina, T. Yokosawa, N. Finck, D. Schild, R. Steininger, G. Göttlicher T. Schäfer, K. Dardenne, J. Rothe, H. Geckeis, T. Vitova,
"U(V) is stabilized in magnetite nanoparticles with concentration relevant for nuclear waste repository",
(in preparation)

I. Pidchenko, C. Garcia, D. Fellhauer, S. Bahl, K. Dardenne, J. Rothe, T. Vitova,
"*In-situ* spectroelectrochemical investigations of $[U^{VI}O_2(CO_3)_3]^{4-}$ and $[U^{V}O_2(CO_3)_3]^{5-}$ complexes: UV-Vis, U M_4 edge HR-XANES/RIXS and quantum-chemical approach",
(in preparation)

I. Pidchenko, E. Bohnert, T. Prüβmann, T. Vitova, R.J. Baker,
"Neptunium carbonate incorporation into uranyl carbonate minerals: An EXAFS and HR-XANES study of the reactivity of Np(V) with Grimselite, $K_3Na[UO_2(CO_3)_3]\cdot H_2O$",
(in preparation)

I. Pidchenko, D. Fellhauer, T. Prüßmann, K. Dardenne, J. Rothe, T. Vitova,
"Revealing the electronic structure of Pu(III)-Pu(VI) in perchloric acid media by high energy resolution X-ray emission and absorption spectroscopy",
(in preparation)

B. Xiao, S.A. Novikov, I. Pidchenko, T. Vitova, D. Schild, J. Stritzinger, G. Roth, D. Bosbach, K.O. Kvashnina, T.E. Albrecht-Schmitt and E.V. Alekseev,
"U(V) stabilization within iriginite-type framework *via* Ln(III) incorporation",
(in preparation)

M. Zegke, X. Zhang, I. Pidchenko, J.A. Hlina, R.M. Lord, G.S. Nichol, J. Bella, A. Prescimone, N. Magnani, G. Schreckenbach, T. Vitova, J.B. Love and P.L. Arnold
"Single-electron reduction of uranyl(VI) with groupI, groupII, group IV and groupXII metals and organometallics",
(in preparation)

Contributions to conferences (Poster and Oral)

I. Pidchenko, D. Fellhauer, T. Prüßmann, K. Dardenne, J. Rothe, T. Vitova,
"Plutonium oxidation state speciation in aqueous solution studied by high-energy resolution XANES technique" (Poster)
3rd ITU-INE Research Fellow Day, Eggenstein-Leopoldshafen, Germany, **6 February 2014**.

I. Pidchenko, D. Fellhauer, T. Prüßmann, K. Dardenne, J. Rothe, T. Vitova,
"Plutonium oxidation state speciation in aqueous solution studied by high-energy resolution Pu L_3 and M_5 edge XANES techniques" (Poster)
4rd ITU-INE Research Fellow Day, Eggenstein-Leopoldshafen, Germany, **13-14 October 2015**.

I. Pidchenko, D. Fellhauer, T. Prüssmann, K. Dardenne, J. Rothe, E. Bohnert, B. Schimmelpfennig, T. Vitova,
"Plutonium oxidation state speciation in aqueous solution studied by Pu L_3 and M_5 edge HR-XANES technique" (Poster)
7th Workshop on Actinides Speciation, Techniques, and Facilities for Radioactive Materials at Synchrotron Light Sources (AnXAS 2014), Villigen, Switzerland, **20-22 May 2014.**

I. Pidchenko, D. Fellhauer, T. Prüssmann, K. Dardenne, J. Rothe, E. Bohnert, B. Schimmelpfennig, T. Vitova,
"Plutonium oxidation state speciation in aqueous solution studied by Pu L and M edge high energy resolution XANES technique" (Oral)
2nd International Workshop on Advanced Techniques for Actinide Spectroscopy
(ATAS 2014), Dresden, Germany, **3-7 November 2014**.

I. Pidchenko, K.O. Kvashnina, T. Yokosawa, N. Finck, D. Schild, T. Schäfer, J. Rothe, H. Geckeis, T. Vitova,
"U redox state and speciation of U in contact with magnetite nanoparticles:
high-resolution XANES, EXAFS, XPS and TEM study" (Oral)
16th International Conference on X-ray Absorption Fine Structure (XAFS16), Karlsruhe,
23-28 August 2015.

I. Pidchenko, K.O. Kvashnina, T. Yokosawa, N. Finck, D. Schild, T. Schäfer, J. Rothe, H. Geckeis, T. Vitova,
"U redox state and speciation of U in contact with magnetite nanoparticles:
high-resolution XANES, EXAFS, XPS and TEM study" (Oral)
15th International Conference on the Chemistry and Migration Behaviour of Actinides and Fission Products in the Geosphere (Migration2015), Santa Fe Community Convention Center, Santa Fe NM, USA, **13-18 September 2015.**